Doctoral Dissertation.
Doctoral Program in Mechanical Engineering
Department of Mechanical and Aerospace Engineering (36° Cycle)

Backface strain as an index to detect damage initiation and propagation in composite adhesively bonded joints

From manufacturing and mechanical characterization of specimens to simulation, estimation of adhesive fracture properties, and Structural Health Monitoring (SHM) of joints

By

Mohammad Abbasi

Supervisor(s):
Prof. Luca Goglio, Supervisor

Reviewers:
Prof. Mariana Doina Banea, University of Aveiro, Portugal.
Dr. Marco Gerini Romagnoli, Oakland University, United States.

Politecnico di Torino
September, 2024

Declaration

I hereby declare that the contents and organization of this dissertation constitute my own original work and does not compromise in any way the rights of third parties, including those relating to the security of personal data.

Mohammad Abbasi

2024

Abstract

Composites and composite adhesive joints are experiencing growing application across various industries, with a notable emphasis in the automotive sector. This is due to the fact that composite materials provide an exceptional mix of lightweight characteristics and structural reliability, making them very attractive for automotive uses that prioritize fuel economy and performance. In addition, progress in adhesive technologies has resulted in the creation of high-performance adhesives that can effectively join a wide range of materials with outstanding durability and dependability. In the automotive industry specifically, Single-Lap Joints (SLJs) find extensive use in joining components such as body panels, chassis parts, and interior elements, offering manufacturers the benefits of improved vehicle aesthetics, reduced weight, enhanced structural integrity, and simplified assembly processes. Therefore, it necessitates to be more aware of the behavior of this type of joining materials.

This dissertation, firstly, investigates the mechanical behaviors of two different types of adhesives, Epoxy-based and Polyurethane-based. To do so, the bulk adhesive dogbone subjected to tensile tests are performed to obtain the properties like Young modulus, elongation, and ultimate strength. Furthermore, to be aware of the fracture behavior and obtain the adhesives' energy release rate in Mode I and Mode II, respectively, Double cantilever Beam (DCB) and End Notch Flexural (ENF) tests were conducted using composite substrates and analyzed. This information could be later employed in finite element modelling to simulate and predict the behavior of adhesively bonded joints.

Secondly, different application of adhesively bonded joints necessitates considering joints with different dimensions. Therefore, the effects of joint geometry parameters, such as adherend thickness (T=1.76, 3.52 mm), joint width (W=10, 20, 30 mm), and overlap length (L=10, 20 mm), on the behavior of single-lap joints (SLJs) under tensile loading are studied in this research activity. Peak force, joint stiffness, adhesive shear stress, and substrate normal stress are the investigated properties. SLJs are manufactured with carbon fiber composite adherends and two different types of adhesives, polyurethane and epoxy, which respectively present a flexible and rigid mechanical response. The results showed that increasing all 3 geometric parameters (L, W, T) leads to a significant increase in the load capacity of polyurethane joints (on average, 88.4, 101.5, and 16.9%, respectively). For epoxy joints, these increases were 47.7, 100, and 46%,

respectively. According to these results, W is the parameter with the most influence on the load capacity of the joints. However, it was observed that an increase in joint width has no significant effect on adhesive shear and a substrate's normal stresses. Epoxy SLJs behave approximately elastically until failure, while polyurethane SLJ load-displacement curves include an initial linear elastic part followed by a more ductile behavior before the failure. Joint stiffness is affected by all the parameters for both adhesive types, except for overlap length, which led to a negligible effect on epoxy joints. Moreover, the damage surfaces for both types of joints are analyzed.

Thirdly, having done the adhesive characterization tests it is understood that due to the fact that the polyurethane adhesives are relatively flexible, the ENF tests might not always be possible to be performed. This is because that this flexibility may result in a substrate interlaminar propagation of a crack before the crack starts propagating in the adhesive layer. Therefore, another alternative is proposed in this research to estimate the fracture properties of polyurethane adhesive by using SLJs experimental test results and performing Finite Element Modelling (FEM) of those tests. By calibrating the model with the SLJs experimental results the adhesive properties can be estimated. LS_Dyna is used for the simulation together with LS_OPT as an optimizer. In addition, after the model is calibrated, the effect of geometric parameters has been analyzed once at 25% of ultimate load and once at a fixed load for each sample. At 25% of ultimate load, it was observed that the increase in the joint width has nearly no significant effect on adhesive shear and peel stresses. However, at fixed load increasing L, W, and T resulted in a decrease in adhesive shear and peel stresses.

Lastly, this growing application of adhesively bonded joints in different industries demands employing structural health monitoring (SHM) technics. In this study, the backface strain (BFS) method, applied by both digital image correlation (DIC) and Fiber Optic Sensors (FOS), is used to detect crack initiation and propagation in adhesively bonded single-lap joints (SLJ). By comparing the positive strain, due to the tensile load, and negative strain related to the bending moment, a point, called zero strain point (ZSP), can be detected on the substrate surface of the SLJ. Using the Bigwood and Crocombe analytical model, the presence of the ZSP on the backface is explained and the experimental results are used to detect it. The monitoring of the ZSP reveals useful information about the health condition of the joint. The main aim of this research is to investigate how the ZSP position varies by changing adhesive type (epoxy and polyurethane) and bonding area dimensions both in elastic conditions and damage progression. The

results illustrate that the position of the ZSP in polyurethane SLJs is closer to the middle of the joint compared to epoxy SLJs. Additionally, the ZSP is more easily recognizable in epoxy adhesive SLJs when substrates are thicker. Finally, the ZSP showed negligible sensitivity to joint width for both types of adhesive joints regardless of the adhesive type. In conclusion, it is shown that the ZSP can be used as a monitoring index to detect damage initiation and propagation in SLJ specimens. Afterward, the applicability of ZSP method is investigated when the joint is subjected cyclic loadings. Having confirmed the functionality and effectiveness of the ZSP method as an index to monitor a joint healthiness, it can be proposed to use this method with (FOS) on real components to have an in-situ monitoring of the joint. Therefore, the component or the joint can be repaired or substituted before the rupture.

Acknowledgment

First and foremost, I would like to express my deepest gratitude to my supervisor, Prof. Luca Goglio, for his invaluable guidance, encouragement, and unwavering support throughout the course of my Ph.D. journey. His profound expertise and insightful feedback have been instrumental in shaping my research and helping me overcome various challenges along the way.

I would also like to extend my heartfelt thanks to my co-supervisor, Dr. Raffaele Ciardiello, for his constant support and constructive advice. His contributions have significantly enriched my work. I am grateful for his patience, dedication, and the many discussions that have deepened my understanding of the subject.

I would also like to acknowledge the members of our research group, especially Carlo Boursier Niutta and Dario Fiumarella, whose collaboration and support have greatly contributed to the progress of my work.

A special mention goes to my colleague and best friend, Davide Pederbelli, whose friendship have been a source of strength and inspiration throughout this journey. His willingness to lend an ear, offer a helping hand, and share in both the struggles and successes has made this experience all the more rewarding. I am thankful for the countless hours we spent discussing ideas, troubleshooting problems, and celebrating achievements together.

Finally, I would like to acknowledge the support of my family and friends, who have been my pillars of strength throughout this process. Their love, encouragement, and belief in me have been crucial in helping me reach this milestone.

Contents

List of Figures

List of Tables

Chapter 1

1. Introduction

1.1. Background and motivation

A bonded joint involves permanently joining two or more substrates or adherends using adhesive [1]. In contrast to conventional fastening techniques such as bolts, pins, nuts, and screws, which frequently result in significant stress concentrations and variable stress distributions, adhesive bonding has the potential to reduce challenges such as corrosion and fatigue fracture in metallic components. [2]. Additionally, it offers engineers the flexibility to design complex geometries that would be difficult to achieve with other joining methods. This method has several advantages, including significant weight reduction in structures, the ability to bond similar and dissimilar materials, uniform stress distribution along the overlap length, compatibility with other joining techniques, and its effectiveness in joining composite materials [2]. However, there are also notable disadvantages to consider. For example, it is challenging to predict when and how a damage can occur and propagate in adhesively bonded joints. Moreover, their behavior when subjected to different conditions including various loading type, temperature and humidity, is not still very well-known [3].

The utilization of adhesives in the automotive sector for assembling load-carrying parts has grown considerably, with the goal of lowering the weight of vehicles to enhance fuel efficiency and decrease emissions of pollutants. Nevertheless, manufacturing a structure that is bonded can be intricate because the characteristics of adhesives can differ widely, ranging from the fragile epoxy

adhesives to the extensively flexible polyurethane adhesives [1,4]. In this regard, the characterization of adhesives demonstrates its significance.

The numerical modeling of adhesive bonds is presently a dynamic area of inquiry with immediate implications for industry. Finite element analysis (FEA) facilitates the optimization of designs for structures capable of withstanding loads, impacts and crashes, thereby diminishing the significant expenses involved in the construction and experimental testing of prototypes. Literature indicates the existence of numerous models, each with varying levels of complexity, designed to address this issue. These models are capable of mimicking the behavior of adhesives.

Structural Health Monitoring (SHM) of adhesive joints plays a crucial role in ensuring the safety, reliability, and longevity of various engineering structures, from aerospace to automotive and civil engineering applications. Adhesive joints, known for their ability to efficiently distribute stress over a wide area, contribute significantly to the structural integrity of composite materials and complex assemblies. However, these joints are susceptible to environmental degradation, fatigue, and hidden damages that can compromise their performance over time. Implementing SHM enables the early detection of such defects, facilitating timely maintenance and preventing catastrophic failures. By continuously assessing the condition of adhesive joints through advanced sensing technologies and data analytics, SHM provides invaluable insights into the health of the structure, optimizing repair strategies, and significantly enhancing operational safety. This proactive approach to maintenance not only extends the service life of components but also contributes to the development of more durable and resilient next-generation materials and structures.

1.2. Problem definition

The automobile sector is presently transitioning towards the utilization of lighter, composite material frameworks which facilitate a diminution in vehicle mass. This reduction contributes to a decrease in fuel consumption and emissions, whilst concurrently enhancing the dynamic performance and safety of vehicles. The sector is currently trying to integrate this adhesive bonding approach beyond the borders of limited-edition sports cars into mass production. Furthermore, the push towards greater electrification of vehicles introduces the challenge of increased vehicular weight due to the necessity for larger batteries. This underscores the imperative for innovations in reducing structural weight. These advanced structures

are predominantly dependent on adhesive bonding. However, predicting their performance under a variety of conditions, including the change in joint dimension, and loading type, remains a complex task that poses significant obstacles for automotive designers.

It is generally possible to comprehend the behavior of joints consisting of metallic substrates, in which the adhesive is intended to maintain the metal's integrity in order to accommodate any plastic deformation. For composite or composite/metal joints, the available information is fairly restricted. The primary objective of this study is to gather empirical information on composite joints in order to comprehend its mechanical behavior, particularly when the dimensions of the joint change. This is due to the fact that not every joint in an automobile construction has the same dimensions.

Obviously, one of the most important parts of an adhesive joint is the adhesive itself. Characterization of adhesives necessitates performing delicate and complicated tests. Therefore, finding an alternative to estimate the behavior of an adhesive will save much time, effort and expenses which should be dedicated to performing experimental tests.

The everyday grown usage of adhesive bonding in different industries makes it important to fully understand the mechanical behavior of these type of joints to apply proper strategies for monitoring them. Because joints are often the weakest areas in composite structures, they are expected to fail first during the structure service life. As a result, adhesive joints are designed with conservative safety margins [5,6], and it is crucial to develop non-destructive testing (NDT) and structural health monitoring (SHM) techniques that are able to provide not only a warning at the initial stage of damage, but also reliable information about joint healthiness throughout service life. This enhances safety and reduced maintenance costs for those applications that need high reliability [7,8], and as well allows the joint repair or replacement to begin when necessary.

This research activity aimed at addressing the mentioned problems and challenges by considering two types of adhesives (SIKAPOWER-1277 epoxy and ADEKIT A 236/H 6236 polyurethane) provided by the Sika (Baar, CH) company.

1.3. Objectives

The main objective of this thesis is to develop a method for structural health monitoring of composite single-lap joints (SLJs) and detect the crack initiation and

following its propagation in this type of joint, which is mostly used in different industries, especially, in automotive industry. The available methods have many challenges and sources of error that may easily affect the results. With the new methodology that is presented in this study not only it is possible to do the SHM of composite SLJs, but the sources of error are also minimized, and the results are accurate and reliable enough. To develop this methodology and have a validated procedure that minimizes experimentation and associated costs it is crucial to comprehend and tackle four significant challenges.

The first challenge is accurately determining the mechanical and cohesive characteristics of the structural adhesives used in this research. By carefully choosing the right sophisticated characterization tests together with suitable data reduction strategies, it is feasible to characterize these adhesives.

As the second challenge, this research puts focus on the effect of bonding area geometry parameters, such as overlap length, joint width, and substrate thickness on the mechanical behavior of the joints with different types of adhesives. The dimensions of adhesive joints critically influence their mechanical properties and overall performance in structural applications. Key dimensions, including thickness, length, and width, directly affect the stress distribution, load-bearing capacity, and failure modes of the joints. A well-optimized joint dimension can enhance the efficiency of stress transfer, minimize concentrations of stress that lead to failure, and improve the durability and reliability of the assembly. Therefore, careful consideration of adhesive joint dimensions is essential in the design phase to ensure that the joint meets the specific mechanical requirements of the application, leading to structures that are both strong and resilient under varying operational conditions.

The third challenge is the establishment of numerical models that can accurately simulate the behavior of adhesive joints in a cost-effective and time-efficient manner, thus minimizing the reliance on expensive experimental studies. In this regard, as already explained, the characterization of adhesives is a very delicate and energy demanding task. Therefore, in this challenge step an alternative to complicated adhesive characterization experimental tests is introduced using the finite element modeling and experimental test of a SLJ. This activity is only performed for polyurethane adhesive.

Lastly, the work studies the strain on the outer surface of the bonding area (Backface Strain (BFS)) to serve the purpose of SHM of composite SLJs. By

observing the BFS a new approach was developed which is capable of detecting the crack initiation and its propagation under static and cyclic loading. Moreover, as the joint dimension is not always the same, the performance of this approach was studied when the joint dimensions change.

To find answers for and address these four challenges, and to analyze the behavior of a composite SLJ with different adhesives and joint dimensions, as well as have enough information on the health condition of the joint **four main tasks** were considered. In section 1.4, each one of the four main tasks is explained from the objective and methodology points of view.

1.4. Research methodology

Figure 1.1 illustrates a schematic of the research methodology employed in this study. This part will provide a more detailed explanation of the experimental tasks, including the specific types of tests and equipment necessary, as well as the numerical procedure. The research methodology is explained in detail in chapters 3 and 4.

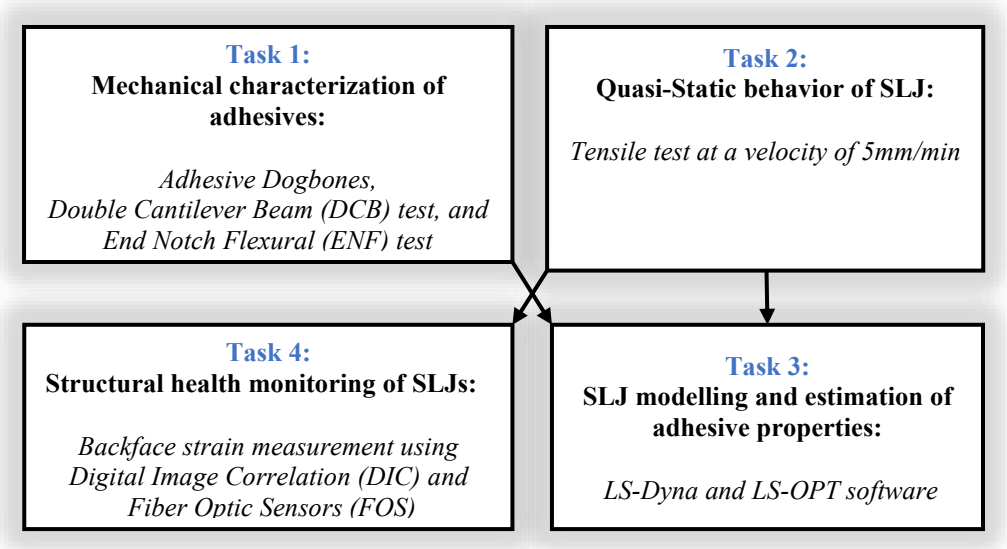

Figure 1.1 schematic of the research methodology

As stated in section 1.3, four main tasks were considered in this investigation.

Task 1 – mechanical characterization of adhesives:

The objective of this task was to determine the adhesives mechanical properties under quasi-static (5 mm/min) conditions separately. Therefore, each adhesive was tested individually and characterized. A carbon fiber reinforced polymer (CFRP) was selected as substrates. The composite substrate, however, was already characterized in [9].

To obtain the failure strength and fracture energy properties different experimental tests were performed. More specifically, adhesives' bulk dogbones were subjected to tensile loading to define the stress-strain curves. Whilst the adhesive fracture energies (energy release rate) in mode I and mode II were assessed by performing double cantilever beam (DCB) and end notch flexure (ENF) tests, respectively. All the tests were carried out in a quasi-static condition at the velocity of 5 mm/min.

The results of this part are used in Task 3 as a confirmation for the adhesive estimated properties from the combination Task 2 (SLJs experimental tests) and Task 3 (Simulation of SLJs).

Task 2 - Quasi-static testing of SLJs at the velocity of 5 mm/min:

The objective of this task was to test and assess different SLJs configurations (considering different joint overlap length (L), joint width (W), and substrate thickness (T)) with CFRP substrates and two types of adhesives (Epoxy and Polyurethane) under quasi-static (5 mm/min). The specimens' load-displacement curves were obtained in order to figure out the joint strength, stiffness, stresses in the bonding area and substrates cross sections. Finally, the effects of each joint geometry and adhesive types were analyzed on the behavior of SLJs.

The results from this part are used in Task 3 in order to estimate the adhesives mechanical properties using the Finite Element Modelling (FEM).

Task 3 – Finite Element Modelling of the quasi-static (5 mm/min) behavior of SLJs with Polyurethane adhesives and estimation of adhesive properties:

The objective of this task was to establish a numerical procedure which is capable of accurately modelling the SLJs with polyurethane adhesive subjected to tensile load at a velocity of 5 mm/min. The experimental results are already obtained in the Task 2. Furthermore, having the model developed and set up, the

mechanical properties of the adhesive are estimated by coupling the model with an optimizer algorithm. This means that there is a possibility to estimate the adhesive properties using FEM and SLJ experimental test result without performing complex tests like DCB and ENF. All the modelling was carried out in the finite element software LS-Dyna. A trapezoidal law was assumed for the cohesive zone model shape. The adhesive material card and cohesive zone model parameters were calibrated and estimated by use of LS-OPT as the optimizer, LS-Dyna as the FEM software, and the SLJ load displacement curve as the reference.

Task 4 – Monitoring the strain on the outer surface of the substrate for the purpose of joint SHM

The objective of this step was to develop a methodology to detect the crack initiation and follow its propagation in the joint. For this purpose, the strain on the outer surface of the substrates in SLJs was observed during the test. Obviously, as adhesives are applied in between two substrates it is not possible to reach out and monitor them directly. Therefore, by carefully analyzing the changes in substrates strain it should be understood what is happening in the adhesive layer and as a result to the joint. Digital Image Correlation (DIC) system and Fiber Optic Sensors (FOS) are the two tools used to monitor the strain on the backface of the substrate. The development of the methodology was successful and proven to be accurate enough to understand the behavior of the joints with both types of adhesives (epoxy and polyurethane). The last challenge was to understand if the joint dimension affects this methodology. Therefore, the test was performed for all the joints with different dimensions considered in Task 2 and the results were analyzed and compared.

1.5. Outline of the thesis

This thesis includes four published papers. Since the activities are very related and in order, the general outline of the thesis is similar to a large paper. Therefore, it includes an introduction section (Chapter 1), a background investigation (Chapter 2), a methodology part (Chapters 3 and 4), results (Chapters 5, 6, 7, 8), and conclusion (Chapter 9).

It should be noted that since this thesis is written based on the already published papers, in order to integrate the papers within the dissertation minor changes have been made on grammar, formatting, and the synchronization of the list of references. The papers [10–13] are assigned to each task in Figure 1.2 and listed as follows:

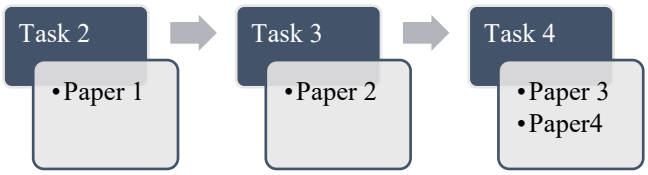

Figure 1.2 List of the papers resulted from each task

1- Abbasi M, Ciardiello R, Goglio L. Effect of bonding area geometry on the behavior of composite single lap joints (SLJ) and estimation of adhesive properties using finite element method. Journal of Adhesion 2023. https://doi.org/10.1080/00218464.2023.2252338.
2- Abbasi M, Ciardiello R, Goglio L. Experimental Study on the Effect of Bonding Area Dimensions on the Mechanical Behavior of Composite Single-Lap Joint with Epoxy and Polyurethane Adhesives. Applied Sciences 2023. https://doi.org/10.3390/app13137683.
3- Abbasi M, Ciardiello R, Goglio L. Backface strain as an index to detect damage initiation in composite single-lap bonded joints: effects of adhesive type and joint dimensions. International Journal of Adhesive and Adhesion 2024. https://doi.org/10.1016/j.ijadhadh.2024.103791.
4- Abbasi M, Ciardiello R, Goglio L. Damage Assessment in Adhesively Bonded Composite Joints using Backface Strain technique. Journal of Composite Part B: Engineering, 2024. https://doi.org/10.1016/j.compositesb.2024.111766.

Chapter 2

2. Literature review[1]

Today, adhesive joints are widely used in a vast range of engineering structures, from buildings to cars and airplanes. Every application has different needs for design. Because adhesive joints have so many advantages, their use has increased significantly in recent years. These benefits include lighter weight and lessened stress concentrations when compared to conventional mechanical bonding techniques like bolts or rivets [14]. Since adhesive joints are used in many different applications, it is essential to establish precise methods for predicting their strength in order to make the design process easier. As seen in Figure 2.1, some of the adhesive joint types that are frequently studied are single-lap joints, double-lap joints, strap joints, T-peel joints, double-strap joints, scarf joints, T-joints, and single-L joints. Therefore, the goal of this chapter, considering the recent research activity, is to provide an overview on the mechanical characterization of adhesives, strength prediction of the adhesive joints, and the structural health monitoring of the adhesive joints.

[1] **The content of this task is already partially published as introduction of papers [10–13]. Minor changes have been made on grammar, formatting, and the synchronization of the list of references in order to integrate the papers within the dissertation.**

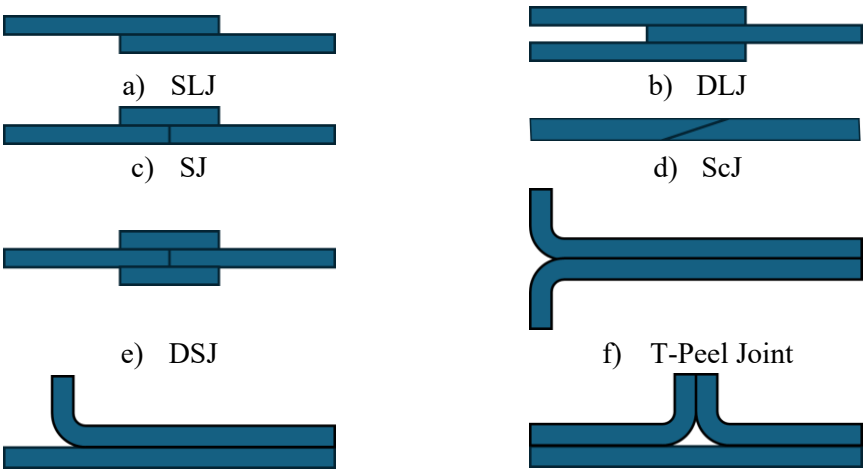

Figure 2.1 Adhesive bonding geometry types [15]

2.1. Adhesive mechanical properties

The adhesive itself is a crucial component of any adhesive joint, thus it is essential to talk about the tests that may be performed to ascertain the adhesives' mechanical and fracture characteristics. However, just a brief of the tests is given since experimental testing is not the main emphasis of this investigation.

The tensile elastic modulus, as well as the tensile yield and failure stresses, are typically determined by subjecting bulk adhesive specimens to tensile loading [16]. To assess the shear modulus, shear yield and failure stresses, tests like Arcan [17], and Napkin Ring test [18], as illustrated in Figure 2.2. These methods precision is rooted from purely shear stress at the adhesive layer [8]. Both tensile and shear tests are essential for the purpose of predicting the strength of an adhesive joint.

Figure 2.2 proper tests to characterize the adhesive shear properties [15]

To obtain the Mode I critical strain energy release rate (G_{Ic}), various tests can be employed. The most used testes are including the Double-Cantilever Beam (DCB) [19] and the Tapered Double-Cantilever Beam (TDCB) [20] as depicted in Figure 2.3. Teixeira et al. [21] made a comparison between the DCB and TDCB and found that the DCB is a superior choice overall for determining G_{Ic}.

These tests are crucial for predicting the strength of adhesive joints when employing fracture mechanics, damage mechanics, cohesive zone modeling (CZM). Moreover, they are important in determining the tensile cohesive strength (t^0_n), which is essential for CZM.

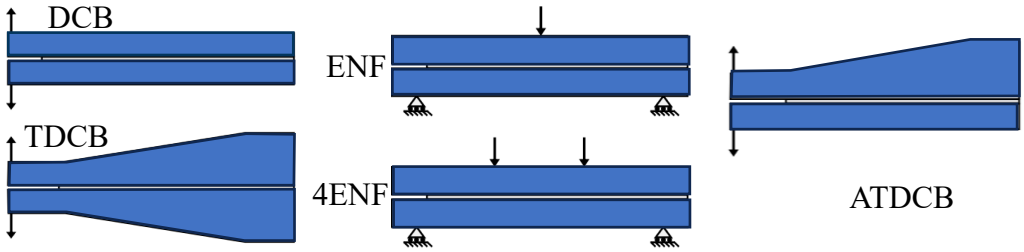

Figure 2.3 Adhesive energy release rate mostly used specimen geometry for different modes [15]

The Mode II critical strain energy release rate (G_{IIc}) is typically evaluated through tests such as End-Notched Flexure (ENF) [22] and four-point ENF (4ENF) [23] as depicted in Figure 2.3. In contrary to mode I (G_{Ic}), which can be obtained from standardized tests, there is no standard for adhesive properties in Mode II (G_{IIc}) [24]. Comparative studies between ENF and 4ENF tests [24] have indicated similar G_{IIc} predictions from both approaches. Nevertheless, ENF tends to outperform due to its broader available data reduction techniques. These tests are essential for forecasting the strength of adhesive joints, employed in fracture mechanics, damage mechanics, cohesive zone modeling (CZM). Additionally, they aid in establishing the shear cohesive strength (t^0_s), crucial for CZM applications.

Further, by performing tests like Asymmetrical Tapered Double-Cantilever Beam (ATDCB) [25] (Figure 2.3) it is possible to obtain the complete fracture envelope of adhesives. This helps establish the correlation between G_{Ic} and G_{IIc} for varying mode-mixities. The study by Hasegawa et al. [26] serves as an illustration, wherein the critical strain energy release rate (Gc) under mode I, mode II, and mixed-mode conditions are defined. The Power law or the Benzeggagh-Kenane law

are typically employed to establish the relation between different modes and the adhesive fracture envelope, as described in (2.1 and (2.2.

$$\left(\frac{G_I}{G_{Ic}}\right)^a + \left(\frac{G_{II}}{G_{IIc}}\right)^a = 1 \tag{2.1}$$

$$G_{Ic} + (G_{Ic} + G_{IIc})\left(\frac{G_s}{G_T}\right)^\eta = G_c \tag{2.2}$$

Where G_I, G_{II}, and G_{III} represent, respectively, the strain energy release rates in mode I, II, and III. G_s is calculated as the sum of G_{II} and G_{III}, while G_T is computed as the sum of G_I and G_s. The parameters η and α, which are material parameters, are determined through tests involving different mode mixities. These parameters play a crucial role in defining the fracture envelope of the material. For a more detailed discussion of different test methods to obtain adhesive energy release rates in different modes the review done by Ramalho et al. [15] can be consulted.

2.2. Adhesive joints Stress and Strength analysis

In general, stress analysis and strength prediction are being done with analytical or numerical methods. The numerical method can be divided into different approaches, the most important of which are continuum mechanics, fracture mechanics, damage mechanics and cohesive zone model (CZM). These approaches are briefly described as follows:

2.2.1. Analytical methods

Over the years, numerous analytical methods have emerged to anticipate the strength of adhesive joints. While these techniques still hold value as initial indicators of joint strength, they have largely been replaced by numerical methods in more complex analyses or situations demanding higher precision. Generally, these methods give stress and/or strain data within the adhesive layer, which are then compared to adhesive properties to determine failure.

Goland and Reissner [27] were among the pioneers who noticed that due to the load eccentricity in single lap joints a bending moment is applied to the joint which causes the joint rotation. They developed an analytical model capable of predicting adhesive internal stresses. Dragoni et al. [28] created software that uses analytical models to calculate the strength of various adhesive joint types. Goglio et al. [29] employed a structural sandwich model to assess the strength of Single-Lap Joints

(SLJ) and T-peel joints, comparing various failure criteria. For a more detailed description of the analytical models these references [30,31] can also be consulted.

2.2.2. Numerical methods

As adhesive joint complexities grow, employing analytical methods to tackle these issues becomes challenging or even infeasible. Therefore, numerical techniques, like the Finite Element Method (FEM), become essential for accurately predicting adhesive joint behavior. While various numerical methods exist for evaluating adhesive joints, the FEM [32] is the most widely employed approach.

- *Continuum mechanics:* Typically, continuum mechanics criteria, along with FEM analyses, are employed to examine stresses within the mid-thickness of the adhesive layer and make strength predictions [18]. The utilization of continuum elements for strength predictions has become less common due to stress singularities at interface corners resulting in rising stress in that area with increased mesh refinement [15]. Nonetheless, there have been several publications utilizing continuum elements for strength predictions of adhesive joints [33,34]. Traditional failure criteria, such as determining failure based on maximum stress or strain in the adhesive's middle, are now employed less frequently. Instead, new failure criteria for adhesive joints have recently been proposed in an attempt to address some of the challenges associated with utilizing continuum mechanics to determine joint strength [15,35].

- *Fracture mechanics:* Fracture mechanics differs from continuum mechanics in its capability to assess stress or strain singularities arising from material discontinuities [36]. In adhesive joints, such discontinuities typically show up as corners at the interface between the adhesive and adherend, or as defects. Traditional fracture mechanics principles employed to analyze crack propagation involve the Stress Intensity Factor (SIF) and the Strain Energy Release Rate (SERR), which are interconnected. There are various approaches to determine the SIF or the SERR, such as J-integral [37] or the Virtual Crack Closure Technique (VCCT) [38].

- *Damage mechanics:* The Damage Mechanics approach enables the simulation of gradual material deterioration in the adhesive, wherein the adhesive gradually loses its stiffness until it reaches a failure point, at which

it completely loses its stiffness. This approach has the capability to determine arbitrary crack paths [15,39,40].

- *Cohesive Zone models (CZM):* the CZM has been extensively explored in recent years for its effectiveness in examining damage and the advancement of cracks in adhesive joints. Typically, it is applied alongside the Finite Element Method (FEM), utilizing specially paired nodes that work in accordance with a predefined traction-separation law (TSL) [27]. These cohesive elements utilize a stress criterion to mark the beginning of damage and a fracture criterion to monitor the progression of cracks. In this approach, the trajectory of the crack is pre-established by the cohesive elements.

  The origins of the Cohesive Zone Model (CZM) trace back to the late 1950s and early 1960s, notably through the research conducted by Barenblatt [41] on crack behavior in brittle materials and Dugdale [42] on the analysis of yield in steel sheets with cracks. A significant benefit of utilizing CZM, as opposed to other methodologies, lies in its ability to predict strength in a way that does not depend on the mesh [43–45]. This characteristic is because of the model's reliance on an energetic criterion that averages damage growth over a defined area rather than basing it on single points.

  CZM can be approached in two primary ways: the local approach and the continuum approach. The local approach employs cohesive elements to link overlapping nodes, effectively creating an interface with negligible thickness (Zero-thickness). On the other hand, to join two surfaces the continuum approach models the entire adhesive bond, which possesses a measurable thickness (finite thickness). These methodologies are different in application, as depicted in Figure 2.4. The local method restricts damage simulation to the connection points of elements, employing solid finite elements to replicate the adhesive's elastic-plastic characteristics. Meanwhile, in the continuum method, the stiffness attributed to CZM elements is reflective of the adhesive layer's stiffness under different loading scenarios.

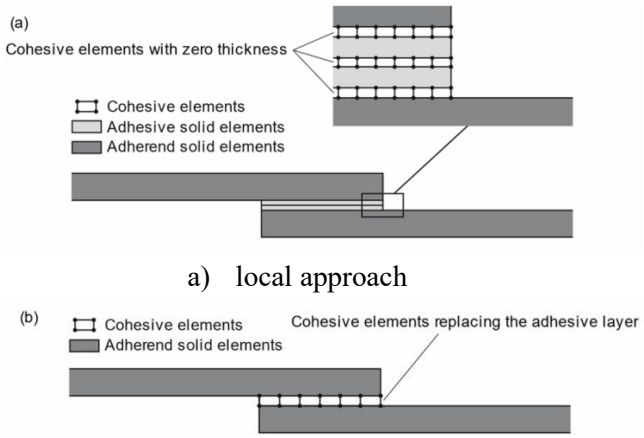

a) local approach

b) continuum approach

Figure 2.4 Cohesive element with different approaches in adhesively bonded joints [15].

The cohesive law, which dictates the behavior of adhesive bonds, can adopt various shapes such as triangular, linear-parabolic, polynomial, exponential, and trapezoidal [36]. Among these, the triangular form is the most straightforward and widely preferred [21], particularly for its effectiveness with brittle adhesives. It can also produce satisfactory outcomes for ductile adhesives under specific scenarios, despite occasionally underestimating strength [46–49]. However, it has been noted that this shape might lead to significant strength underestimations in the case of highly ductile adhesives [50]. Different shapes of cohesive laws are illustrated in Figure 2.5.

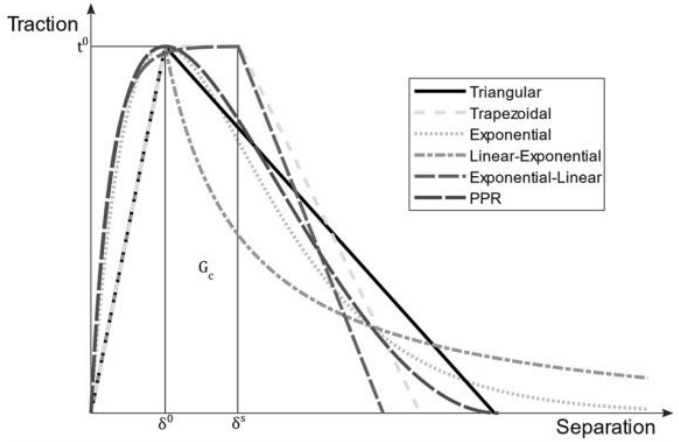

Figure 2.5 Different types of traction-separation laws for cohesive zone modelling [15].

2.3. Single-Lap Joints (SLJ)

Out of the various designs for bonding connections using adhesives, SLJs have been the subject of the most extensive research [51–54]. Nevertheless, there remains the potential to enhance the accuracy of strength prediction and mechanical performance of these joints. The complexity of defining the performance of a joint arises from various factors, including substrate materials [55,56], adhesive and joint type [57], overlap length [58], adhesive thickness [59], joint width [53], fillets at the edges [60], surface treatment [61–63], strain rate, and temperature [64]. These factors each contribute to the joint's behavior and are not easily quantifiable. Additionally, the adhesive type employed in the joint is another crucial component.

The characteristics that have received the most attention in the study of SLJs are the length of the joint and the thickness of the adhesive. Generally, it has been established that increasing the overlap length and the adhesive thickness led to an increase and decrease in the joint's ultimate stress, respectively [61,65–67]. Cui et al. [61] discovered that in SLJs with aluminum-alloy substrates, a greater adhesive thickness generally reduces the joint strength. However, with an overlap length of 20 mm, the strength initially increases and then drops. Furthermore, when the length of overlap rises, the strength of the joint also improves, but only up to a certain point. A parameter called δ (C/(L/2)) was established to analyze this outcome. C represents the minimal length of the remaining adhesive on one adherend, whereas L denotes the length of the joint overlap. They demonstrated that by increasing the overlap length, the peak load could be raised when the overlap length was small (with δ close to 1). Adams and Peppiatt [68] found that the decrease in joint strength caused by increasing the thickness of the adhesive was due to the higher occurrence of micro cracks and voids in thicker adhesives. However, certain researchers have linked this decrease to an increase in bending moment due to the presence of eccentric loads inherent in the SLJ testing configuration [61,69].

However, the literature has not extensively studied the width of the SLJ and the thickness of the adherend. A study conducted by Aydin et al [52] revealed that thicker adherends in SLJs with metallic substrates result in a greater transmission of shear stress from the edges to the middle of the joint. Furthermore, the failure surface exhibited a more severe and disastrous outcome in joints that had thicker adherends. Reis et al [70] investigated the effect of the rigidity of the substrates on the behavior of adhesively bonded joints. They showed that in adhesive joints with more rigid adherends a more uniform distribution of stress occurs in the joint. This, in turn, improves the shear strength of the joint. The effect of the width on the

behavior of SLJ test was studied by Gültekin et al [53]. They showed that increasing the metallic adherend width led to a rise in the load capacity of the joints. This rise is higher compared to the increase of overlap length. The same results were also obtained by Martinez et al [71].

2.4. Structural Health Monitoring (SHM) of SLJs

In the past few years, it has been seen that the composite materials have been increasingly used as an alternative for metals, mainly due to their good mechanical properties, possibility to be shaped into different geometry, light weight, and a high resistance against corrosion. Consequently, this fast growth of composite application in different industries like automotive, aerospace, civil and marine engineering has made the urge to use reliable joining methods to connect small or large components [72]. Traditionally, mechanical fastening like bolts and rivets, welding and adhesive bonding are widely used techniques to join composite materials. Adhesive bonded joints offer significant advantages over traditional mechanical joints, such as reduced weight, lower fabrication costs, improved damage tolerance, and the ability to join dissimilar materials without corrosion concerns. Due to these benefits, these joints have found extensive applications in various industries including aerospace and automotive [5,15,57,72]. Therefore, it is important to fully understand the mechanical behavior of adhesive joints to apply proper strategies for monitoring these joints. Because joints are often the weakest areas in composite structures, they are expected to fail first during the structure service life. As a result, adhesive joints are designed with conservative safety margins [5,6], and it is crucial to develop non-destructive testing (NDT) and structural health monitoring (SHM) techniques that are able to provide not only a warning at the initial stage of damage, but also reliable information about joint healthiness throughout service life. This enhances safety and reduced maintenance costs for those applications that need high reliability [7,8], and as well allows the joint repair or replacement to begin when necessary.

In general, various technologies and methods have been used to monitor the damage in composite joints. Frequently used ones are nanocomposite-based monitoring (using e.g., carbon nanotubes (CNTs)) [73–77], electromechanical impedance (EMI) (e.g. piezoelectric sensors)[78–81], acoustic emission (AE) [82–84], digital image correlation (DIC) [85,86], and fiber Optic sensors [87–90]. Each method has its own advantages and disadvantages. Embedding CNTs into non-conductive polymer matrices leads to the formation of an electrical network, which will be disrupted when subjected to strain. By applying tensile load to the specimen,

the distance between the embedded CNTs increases and results in a rise in the resistance of the specimen. The relation between the electrical resistance changes and the strain is already provided in [91]. Although this method has advantages like presenting a relatively high sensitivity, it has also limitations regarding detection of damage location and type [92]. Piezoelectric sensors as an EMI could be embedded in the specimen or be employed as a part of external monitoring system [72,93,94]. Positive aspects of EMI could be damage initiation identification and in-situ damage monitoring while its drawbacks could be the number of used sensors and possible effects on the performance of the specimen [78–81]. Although Acoustic emission has been excessively used for SHM of composite laminates it has been used limitedly for adhesive joints [72]. Although this method is fully passive and is able to pinpoint the damage initiation and identify the damage mode (e.g. adhesive or cohesive), it is considerably challenging to deal with extensive analysis of data acquired by this method. For this reason, it is common to take advantage of machine learning approaches with this method. Fiber Optic Sensors (FOS) have been used extensively for SHM of different types of composite joints [72,87–90]. Fiber Bragg Grating (FBG) sensors are the most popular FOS, which work by etching micro-structure brag gratings inside an optical fiber core, reflecting a specific light wavelength [95]. This wavelength changes when a FBG be subjected to external mechanical or thermal load, which allows accurate measuring of strain. Due to the mall size, FBGs might be embedded in the joint, but it may affect the specimen performance. Finally, Digital image correlation (DIC) is a non-contact method which is capable of inspecting large areas based on the images acquired by high velocity cameras [96]. DIC works based on comparing pixel by pixel of each acquired image with the previous image or a chosen reference image in order to measure the displacement and consequently the strain in the specimen. The drawbacks of the DIC could be the difficulties while preparing the samples and limited damage type detection. In the present study, both DIC and FBG are used for structural health monitoring of composite Single-Lap Joints (SLJs).

Backface strain (BFS) measurement technique that could be used as an NDT method was introduced in 1986 by Abe and Satoh [97] to study crack formation in spot-welded joints. As it is obvious from the method's name the first step is to measure the strain on the back surface of the specimen using one or more approaches which have been mentioned previously. This technique has been applied to adhesively bonded joints, resulting in numerous investigations [7,8,97–101] that all aim to efficiently detect adhesive damage. The BFS measurement method is particularly effective for evaluating the presence of hazardous cracks [7,8]. This method involves placing strain gauges on the external surface of the bonded joint,

known as the backface. Zhang et al. [8] used a measuring point by installing strain gauges at the overlap's end, focusing on the increased bend caused by cracks. Solana et al. [99] used the BFS by measuring the strain on the backface by using strain gauges and monitoring the ones with the largest strain gradient. Considering the BFS method, many researchers tried to monitor the adhesively bonded SLJs damage by placing strain gauges on the joints where stress concentration is high [7,8,99]. However, establishing the optimal location for these gauges is challenging due to the mixed-mode nature of SLJs as a result of their geometry. The BFS technique has also successfully been used employing arrays of strain sensors by other researchers to monitor crack propagation in SLJs and detect strains in different positions within composite SLJs [102,103]. For composite materials, there is the possibility of embedding sensors within composite laminates closer to the crack [104]. In SLJs, crack initiation and propagation can be monitored by detecting the position of the BFS profile peak [8]. The position of this strain profile peak has been confirmed to closely correspond with the crack tip location [7]. The correlation between the crack front and the BFS peak location in SLJs depends on factors like adhesive fillet presence, materials used, and substrate mechanical properties. Preisler et al. [98] employed the zero-strain point (ZSP) within the region exhibiting the most significant change in longitudinal strain for monitoring structural damage. ZSP is a point where the strain is zero due to the concurrent effect of tensile and bending strains. In such a point, under normal, undamaged conditions, there is no longitudinal strain present, independently of the applied load.

2.5. Gap and future work

Firstly, In the literature, there is a limited amount of research that comprehensively examines the impact of bonding area geometry on SLJs (single lap joints) with composite substrates. Specifically, there are few studies that focus on the impacts of adherend thickness and width [59,60,68]. This becomes more specific when it comes to the examination of the mechanical properties of carbon fiber composite SLJs that are bonded using both polyurethane and epoxy adhesives. As far as the author knows, there is no existing study in the literature that compares the impact of bonding area on the mechanical properties of adhesive joints using CFRP and both a rigid and flexible adhesive comparatively. Hence, it is necessary to evaluate the impact of bonding geometry, namely the dimensions of length (L), bond width (W), and substrate thickness (T), on the quasistatic performance of SLJs. Furthermore, it is crucial to discuss the distinctions in the behavior of epoxy and polyurethane SLJ.

Secondly, in most cases, characterization of the adhesives (G_{IC} and G_{IIC}) was done by taking advantage of direct methods [105,106]. Different available testing methods and geometry were explained in this regard. The most used and known geometries to obtain G_I and G_{II} are DCB and ENF respectively. As performing these kinds of tests is delicate, introducing an alternative could be quite useful. Therefore, it would be a good idea to estimate the mechanical behavior of adhesives using Finite Element Modeling (FEM) together with a SLJ experimental test. For this purpose, using the CZM method and cohesive elements to the simulate the adhesive layer can be used as a validated and powerful tool.

Finally, as the SLJs are the most widely used joints, it is important to know when the damage starts in these joints and how it propagates. Although other researchers have proposed methods like observing the peak of the backface strain profile as an index to check the healthiness of the joints there are drawbacks which impose the urge to develop other methodologies. The present study investigates the reliability of the zero-strain point (ZSP) method for detecting damage in composite SLJs subjected to static loading by using two different adhesive types (polyurethane and epoxy) and different bonding area dimensions. This method is based on the specimen measured backface strain. A large campaign of test was carried out using DIC to monitor the deformation of the backface of the SLJ. Considering the literature about SLJs and SHM, there is no study available on the effect of these adhesive types and joint dimensions on the crack initiation and propagation in these joints using the ZSP as a monitoring point. Further, the effect of each parameter on the position of the ZSP in different joints has been analyzed. Finally, taking advantage of the Bigwood and Crocombe model the experimental results were explained and compared with the analytical results. This method also could potentially be used to approximate the damage initiation point position in a SLJ. Therefore, the reliability of the ZSP method is firstly assessed based on the physical response of SLJs to static loading and with the observation of the DIC within the elastoplastic transition of the samples. Then, the experimental results were compared to the results initially obtained by the Bigwood and Crocombe elastic model. This comprehensive research activity on the effects of different parameters on ZSP position using the DIC and fiber optic sensors allowed an elaboration of a strategy to monitor SLJ in both online and offline modes. Finally, having the methodology confirmed it is proposed to be used with fiber optic sensors in real application.

Chapter 3

3. Experimental activity[1]

In this chapter, the details of experimental activity including the used materials, design of experiments, specimen manufacturing, test setup and machines are explained.

3.1. Adhesives

3.1.1. Bulk Adhesives' Dogbones manufacturing and testing

The adhesives used in this research were ADEKIT A 236/H 6236, a polyurethane-based adhesive, and SIKAPOWER-1277, an epoxy-based adhesive. These adhesives are produced by Sika (CH) company. According to the Technical Data Sheet, ADEKIT A 236/H 6236 can be employed in a wide range of applications and industries including transportation, marine, automotive, and aerospace. Moreover, it is compatible with different materials, such as composites, especially for bonding large parts, metals, and plywood. SIKAPOWER-1277 is designed for high strength and impact-resistant bonding of metallic substrates, such as steel and aluminum, as well as of composite substrates, such as GFRP and CFRP laminates. According to the standard ISO 527-3:2018 [107], dogbone specimens of these two adhesives dimensions were selected (Figure 3.1), manufactured (Figure 3.2a) using a Teflon die (Figure 3.2b), and tested. The polyurethane dogbone

[1] **The content of this task is already published as methodology part of papers [10–13]. Minor changes have been made on grammar, formatting, and the synchronization of the list of references in order to integrate the papers within the dissertation.**

specimens were post-cured in a curing oven at 70 °C for 16 h to respect the material datasheet provided by the producer company. Finally, the tensile tests were carried out by means of a Zwick/Roell (Z050) machine equipped with a laser extensometer. The tensile tests were performed at a constant crosshead velocity of 5 mm/min.

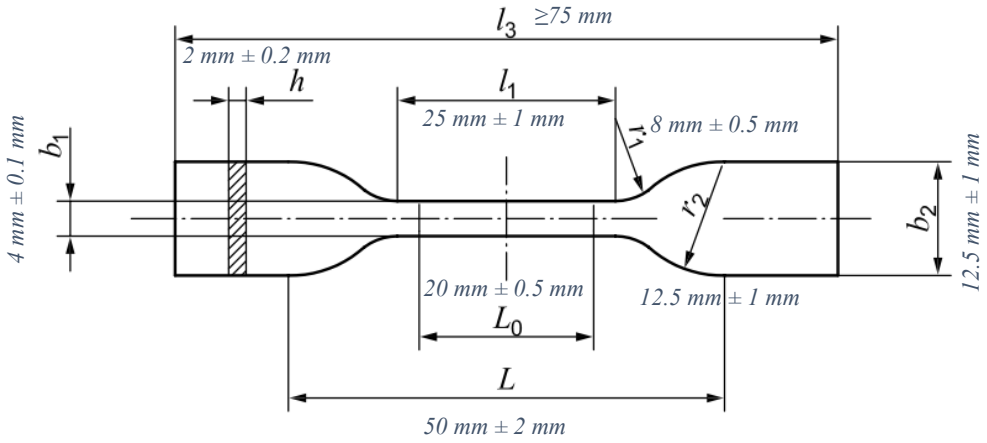

Figure 3.1 Adhesive dogbone dimensions [107]

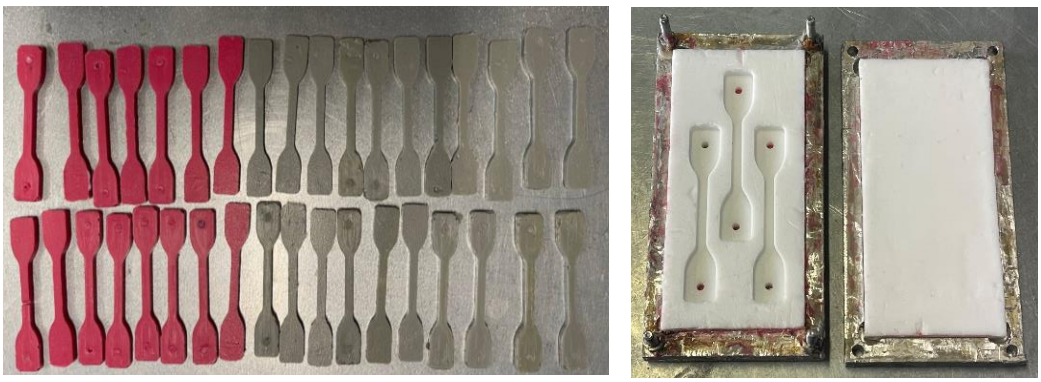

(**a**) (**b**)

Figure 3.2 **a**) Adhesive bulk specimens; (**b**) dogbone Teflon mold.

3.1.2. Double Cantilever Beam (DCB)

DCB specimens were fabricated to evaluate how the adhesive behaves under mode I fracture by measuring the mechanical parameter termed mode I fracture toughness, abbreviated as G_{Ic}. Understanding fracture toughness properties is

crucial for enabling numerical investigations of adhesive joints using fracture or damage mechanics techniques. The DCB specimen specification is given in ASTM D3422 and ISO 25217:2009 standards [108,109]. This specimen's construction is relatively straightforward, comprising two separated beams bonded by an adhesive layer with a pre-existing crack (a_0). Figure 3.3 illustrates a schematic drawing of a DCB specimen.

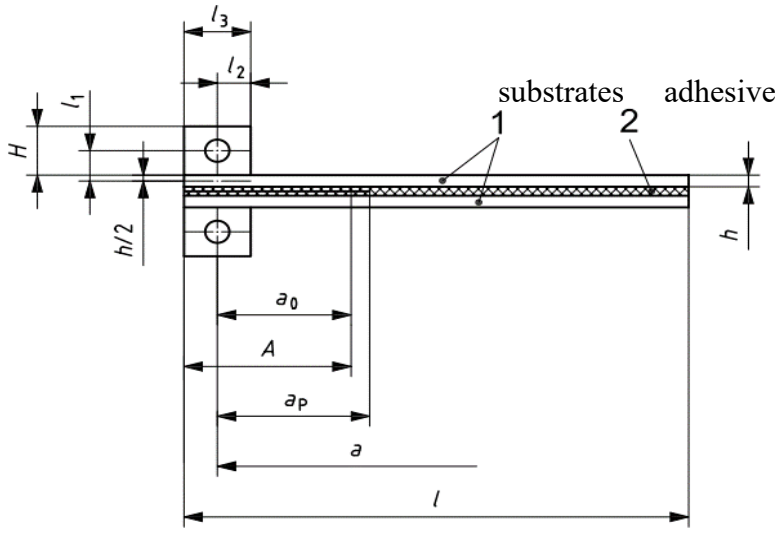

Figure 3.3 a DCB specimen schematic [109]

Applying a force to separate both beams at the unbonded section prompts the crack to propagate along the adhesive layer. The desired outcome is stable crack propagation, facilitating the computation of mode I fracture toughness through a data reduction process.

The DCB specimen used in this study were manufactured using two carbon fiber composite substrates. The mechanical properties of the carbon fiber prepregs are given in Table 3.1. Moreover, the specimen dimensions are also provided in Figure 3.4. The joint preparation, surface treatment, alignment, and curing are explained in section 3.2 for SLJs. The same approach was applied to manufacture the DCB specimens. An ultra-thin aluminum foil is placed at the middle of the adhesive layer to create a pre-existing crack. The initial crack length is represented by a_0, which is the horizontal distance from the aluminum foil tip to the load application line. Understanding this value of a_0 is essential for determining the energy release rate. The a_0 value for these studies ranged from around 48 to 50 mm. Each specimen was carefully measured to assure the correctness of the computed

a_0 value. The tests were performed using the Instron (US) 8801 servo-hydraulic machine at a velocity of 5 mm/min. The test setup is shown in Figure 3.5. To perform the test properly, the digital Image Correlation (DIC) system was employed (Figure 3.5). The sample preparation to use this is explained in section 3.2.3 for SLJs. The same process was followed to prepare the DCB specimens for the DIC system.

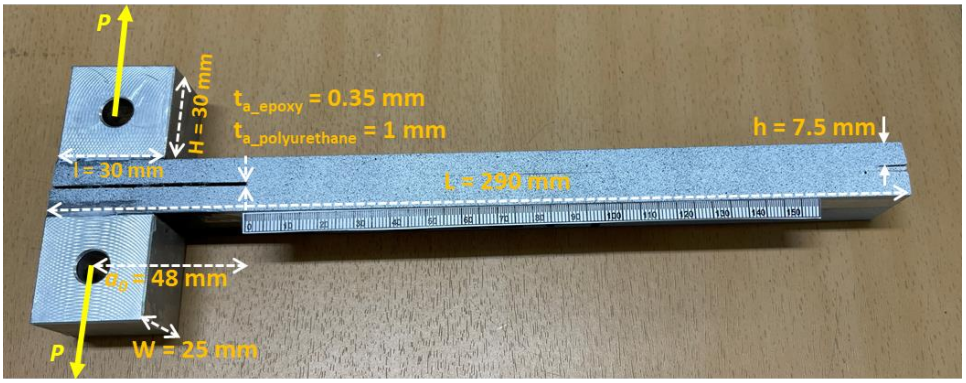

Figure 3.4 DCB specimen geometry: t_a=adhesive thickness, a_0=initial crack length from the loading line, W= width of the specimen, L=length of the specimen, h=substrate thickness, H=block height, l=block width.

Figure 3.5 DCB test setup

3.1.3. End Notch Flexural (ENF) specimen

Currently, there are no recognized standards specifically developed for evaluating mode II fracture in adhesive joints. However, several tests that were initially designed to assess the interlaminar fracture of composites in mode II have been modified for the purpose of examining adhesive junctions. The End Notch Flexural (ENF) test is the most often employed method for characterizing the mode II adhesive joint fracture due to its simplicity and widespread usage (Figure 3.6). The ENF testing method involves using two beams of uniform thickness that are joined together and supported at the ends. Shear stress is generated within the adhesive when a load is applied at the middle. The ENF specimens are identical to the DCB specimens in terms of their overall size and production technique and test velocity. The only distinction is in the length of the initial crack (a_0) which is considered to be 70 mm for ENF specimens. The schematic of the ENF specimens is shown in Figure 3.7.

Figure 3.6 ENF test setup

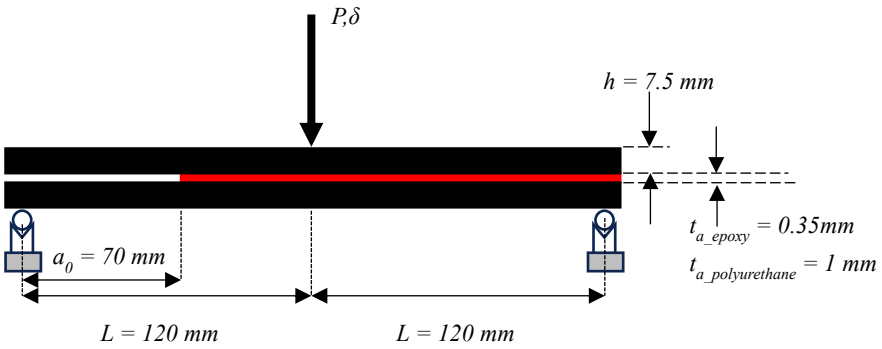

Figure 3.7 ENF specimen schematic (the specimen width is 25 mm).

3.2. Single Lap Joint (SLJ)

3.2.1. Substrates material

For the substrates, on the other hand, a carbon fiber/epoxy prepreg woven, named XPREG XC130, was used. This 210 gsm 3k reinforcement combines a high strength TR30S fiber for optimal performance and a 2x2 twill weave (the fiber orientation is 0°/90°) to provide excellent drape qualities. The mechanical properties of this composite material are reported in the works of Ciampaglia et. al. [9] and Benelli et al. [110]. They were experimentally assessed and are reported in Table 3.1.

Table 3.1 Mechanical properties of the carbon fiber composite material [9,110].

	Mean Value	STD
Density(kg/m^3)	1450	
Poisson's ratio	0.12	
Longitudinal modulus (MPa)	58,000	340
Longitudinal tensile strength (MPa)	440	16
Longitudinal tensile ultimate strain	0.0072	
Longitudinal compressive strength (MPa)	453	36
Longitudinal compressive ultimate strain	0.096	
Transverse tensile strength (MPa)	440	16
Transverse compressive strength (MPa)	453	36
In-plane shear modulus (MPa)	3900	
In-plane shear strength (MPa)	72	

3.2.2. Design of experiment, manufacturing and testing

To observe the effects of overlap length (L1= 10mm, L2= 20mm), adherend thickness (T1= 0.88mm, T2=1.76mm, T3=3.52mm), and joint width (W1= 10mm, W2= 20mm, W3= 30mm) on the behavior of SLJs (Figure 3.8) under tensile loading a set of tests was carried out (Table 3.2). The specimens are named based on these three parameters. For illustration, L1W2T3 stands for the specimen with the overlap length L1, joint width W2, and adherend thickness T3. For each sample, three repetitions were considered, thus a total of 108 specimens were manufactured. In the design of the SLJs, the thickness of the adhesives (measured with an electronic caliper) was in the range t_{PA} = 1.1 ± 0.1 mm for polyurethane adhesive, and t_{EA} = 0.33 ± 0.05 mm for epoxy adhesive. Additionally, the length between the beginning of the bonding area and the end SLJ is considered to be a fixed amount of 85 mm from each end of the specimen.

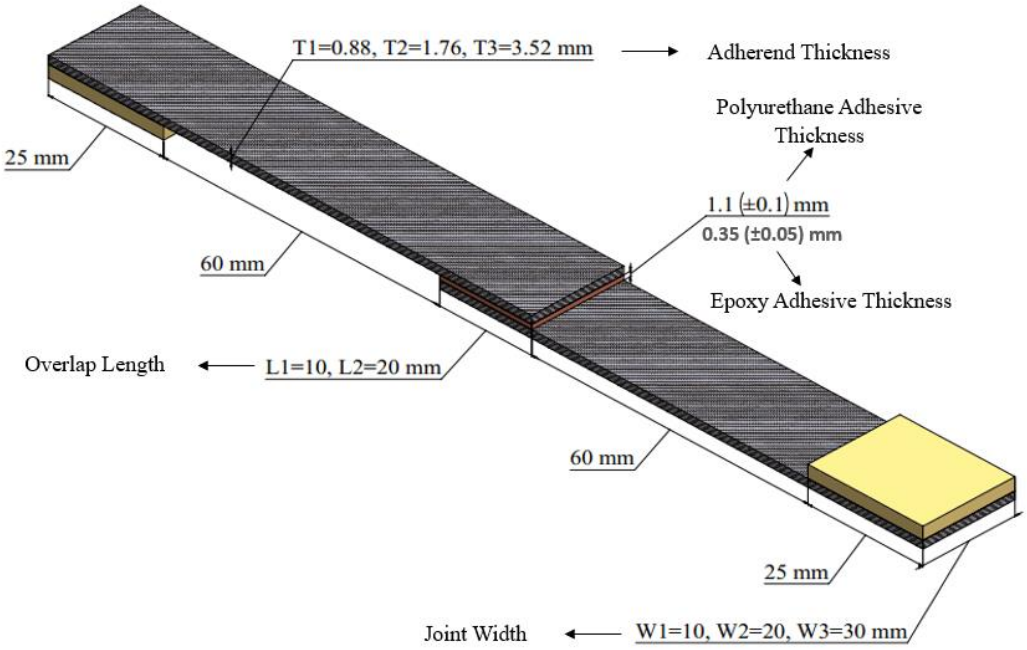

Figure 3.8. SLJ geometry

The thickness of each carbon fiber prepreg is 0.44 mm. Therefore, to obtain the desired adherend thicknesses, three laminates were produced with different numbers of layers (2, 4, 8 layers). Then, they were vacuumed by using the vacuum bag technique (Figure 3.9a). Following the manufacturer recommendation, the laminates were kept at room temperature (23 °C) for 24 hours and then cured in the

oven. A temperature ramp with different slopes was set to the oven starting from 20 °C to 120 °C. The total process of curing in the oven took 7.5 hours.

Table 3.2. SLJ design of experiments

Parameters		T1 (0.88mm)	T2 (1.76mm)	T3 (3.52mm)
L1 (10mm)	W1 (10mm)	L1W1T1	L1W1T2	L1W1T3
	W2 (20mm)	L1W2T1	L1W2T2	L1W2T3
	W3 (30mm)	L1W3T1	L1W3T2	L1W3T3
L2 (20mm)	W1 (10mm)	L2W1T1	L2W1T2	L2W1T3
	W2 (20mm)	L2W2T1	L2W2T2	L2W2T3
	W3 (30mm)	L2W3T1	L2W3T2	L2W3T3

Afterwards, laminates (Figure 3.9b) were cut by using a waterjet to manufacture the substrates with the planned dimensions (Figure 3.9c). The strength of the adhesive joints can be highly affected using surface preparation [15]. Therefore, the bonding area was treated manually using sandpaper (P500) and then cleaned with acetone wipes as suggested by the producer. Finally, using a Teflon mold, the joints were aligned and manufactured (Figure 3.9d). This procedure is shown in Figure 3.9. To possess good control of the thickness throughout the overlap length, a weight was applied on the upper substrate from the beginning or middle of the substrate (not jointed area) up to the end of the joint area (bonded area) and by inserting a spacer that allows for obtaining the designed thickness. Further, the thickness was measured after fabrication for verification. The specimens with epoxy adhesive were ready to be tested manually after the remaining 24 h at room temperature (23 °C). However, after preparing the joints with the polyurethane adhesive, they were kept at room temperature (23 °C) for the first 24 h and then put in the oven at 70 °C for 16 h. When the curing process was finished, the excess adhesives were removed as they may increase joint stiffness and strength. Then, the specimens were ready to be tested (Figure 3.9e).

Tests were performed using again the Instron (US) 8801 servo-hydraulic machine at a crosshead velocity of 5 mm/min. Additionally, 2 tabs of 25 mm were applied in the clamping area, as shown in Figure 3.8, to prevent misalignment. Strength of each joint was computed by using the maximum load to bonding area (overlap length multiplied by width) ratio. The actual dimensions of the joints were measured after the preparation of the samples.

(**a**)

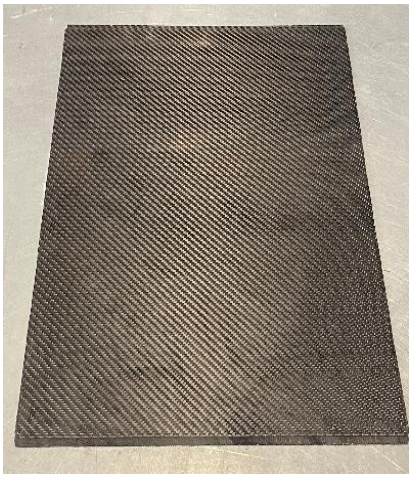

(**b**)

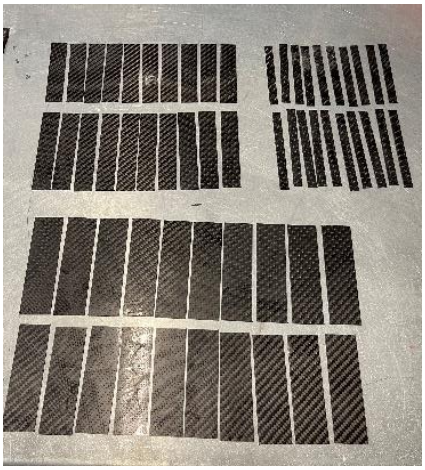

(**c**)

(d)

(**e**)

Figure 3.9 Manufacturing of specimens: (**a**) vacuuming the prepregs; (**b**) plates of composites with different thicknesses; (**c**) laminates cut to the desired dimensions (**d**) SLJs' alignment in the fixture; (**e**) manufactured SLJs.

3.2.3. Specimen preparation for measuring the backface strain

Having all the SLJ samples prepared (Figure 3.9a) it was time to install optical fibers on the outer surfaces of the joints. Both outer faces of the SLJ specimens were used to ensure that both sides of the joints are experiencing the same changes. One optical fiber was used in a manner such that attaching it both above and below the joint, a combined total of four lines of attachment were achieved (only the parts on the bonding area were attached to the SLJ). Figure 3.10a shows the installed fiber only on the surface of the joint. In order for the fibers to be straight and without any bends, they were maintained in a tensile state and attached on the joint area using a cyanoacrylate (Super Attack) glue. The next step was to prepare the samples to be recognizable by the Digital Image Correlation (DIC) tool. For this purpose, the bonding area is first painted with white color and then a speckle pattern is produced by spraying the black color as random points. It is tried to make the pattern randomly formed with black and white points considering an approximate ratio of 1 (Figure 3.10b). Finally, two tabs of 25 mm were applied in the clamping area, as shown in Figure 3.8, to avoid misalignment while applying the load.

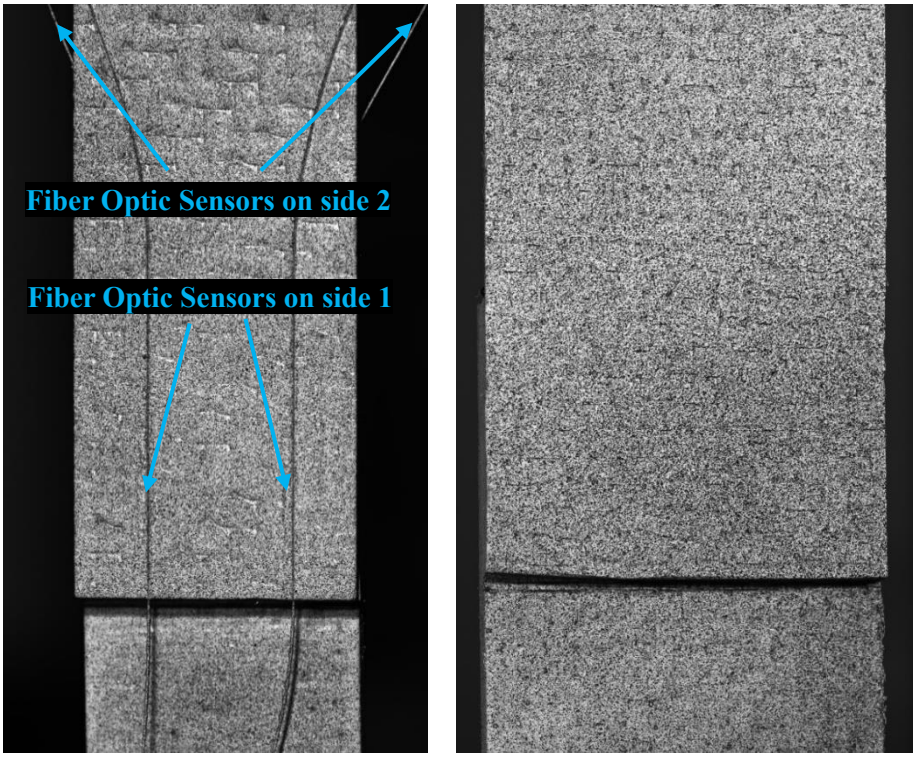

a) optical fibers and speckles b) Speckle pattern for DIC

Figure 3.10. Specimens' preparation for LUNA and DIC

3.3. Machines and tools

3.3.1. Curing Oven

The OV301 is a professional, industrial grade curing oven (Figure 3.11) designed and manufactured by Easy Composites Ltd (UK). It is optimized for composites use, including curing or post-curing laminates, prepregs, thermoplastics, castings, and molds. The oven is engineered for laboratory or R&D use as well. In this research activity, this oven is used for curing composite laminates, adhesives and specimens.

Figure 3.11 Curing oven

Key features of the OV301 include according to the manufacturer:

- Ramp and Soak Programming: It has an internal memory for storing numerous cycles, with full alpha-numeric names.
- Vacuum Pump Control Socket: Integrates a power socket for a vacuum pump, which can be automatically or manually controlled, with a maximum output of 500W.
- Vacuum Ports: Two vacuum ports are provided for connecting a vacuum bag inside the oven to a pump outside, enhancing the oven's functionality for vacuum-assisted processes.

3.3.2. Waterjet cutter

Once a composite laminate with the specified thickness and properties has been manufactured, it is necessary to cut it to the appropriate dimensions based on the

design of experiments. For this purpose, the waterjet cutter shown in Figure 3.12 is used. This machine is supplied by the Wazer manufacturer.

Figure 3.12 Wazer Waterjet cutter

80 Mesh Alluvial Garnets is the powder used as abrasive material together with water to cut specimen by the waterjet. There is a distinct container designated for this abrasive as shown in Figure 3.13a. The cutting bed, shown in Figure 3.13b, is designed to allow the secure attachment of the laminate using screws).

a) Abrasive feed container

b) Cutting bed

Figure 3.13 Wazer Waterjet cutter parts

The initial stage involves creating a two-dimensional representation of the component to be cut using design software such as AutoCAD, Solid Works, or any other program capable of generating a .dxf file. The correct format for accessing

the Wazer online program is through the URL wam.wazer.com. This online platform offers customers a virtual cutting surface where they can import and position their drawings. Furthermore, the specific material can be chosen or specified from the materials menu. There are other alternatives to select from, such as metals, plastics, rubbers, ceramics, stone, and other materials. Given that the method involves dealing with composites made of carbon fiber, this material is chosen from "other" category by specifying the thickness.

The path of the cut can be selected as either centered, outside, or inside the design. Opting for the external path is a prudent choice since it allows for a certain level of tolerance towards undesired errors, such as those that may occur when employing sandpapers. Lastly, the user can select the desired level of precision for the cut. In addition, the precision of the cut impacts the duration of the procedure. Once these procedures are done, it is now feasible to produce the file and store it in an external memory card that will be linked to the Wazer waterjet cutter.

Once the programming is completed, the next step involves configuring the waterjet cutter. It is necessary to verify if the cutting bed is free of dirt, if the abrasive container is full of abrasive, and if the pressure nozzle is open. All of these factors contribute to the optimal operation of the machine and the precise cutting of specimens and laminates.

After completing all the necessary preliminary checks, the laminate is positioned on the cutting bed and securely fastened using screws. Then the prepared cutting program is chosen. Prior to commencing the cutting process of the laminate, it is necessary to manually determine the position of the nozzle, specifically where to initiate the cut. It is highly advised to take advantage of the dry-run option in the menu which allows users to visualize the precise cut path (by moving the nozzle without cutting) and guarantees error-free cutting during the actual operation. Ultimately, the cutting process can commence by simply closing the waterjet cutter lid. The machine will display the remaining duration for the completion of the operation. Once the cutting process is complete, the specimens are now prepared with the desired dimensions.

3.3.3. Instron testing machine

The servo-hydraulic Instron (Norwood, MA, USA) machine 8801 (Figure 3.14) is widely used in labs as a common apparatus for conducting tensile tests. To help reduce the disruption caused by vibrations, a damper installation is used to support

the machine's base on the floor, given its substantial weight. Additionally, it ensures the correct functioning of other devices that are often susceptible to vibrations like DIC.

Figure 3.14 Instron 8801

3.3.4. Digital Image Correlation (DIC)

Digital Image Correlation (DIC) is a non-contact, full-field optical technique used to measure the displacement and deformation of objects subjected to mechanical loading. It involves analyzing images of a specimen before and after deformation to quantify the changes in shape and size at various points across its surface. DIC operates by tracking the movement of small patterns, known as speckle patterns, applied to the surface of the specimen. These speckle patterns act as unique identifiers, allowing the software to match corresponding points between the reference (undeformed) and deformed images. By comparing these matched points, DIC algorithms calculate the displacement and strain fields over the entire surface of the object. The method, actually, tracks the gray value pattern in small neighborhoods called subsets during deformation. The commercially available VIC-2D and VIC-3D systems from Correlated Solutions are among the available postprocessing software which both utilize this advanced optical measurement technology.

DIC is widely employed in various fields such as:

- Material Characterization: DIC is used to study the mechanical properties of materials such as metals, polymers, composites, and biological tissues.
- Structural Testing: DIC is employed in structural testing to assess the performance of components and assemblies under various loading conditions. It helps identify areas of stress concentration, deformation patterns, and failure mechanisms.
- Biomechanics: In biomechanics, DIC is utilized to analyze the deformation of biological tissues and implants under physiological conditions.
- Geotechnical Engineering: DIC is applied in geotechnical engineering to monitor the deformation of soil and rock structures during construction, excavation, and slope stability analysis.

In this study, a 3D version of the Correlated Solution (Columbia, SC, USA) DIC tool (Figure 3.15) was utilized to measure the displacement field on the surface of the SLJs. The lenses were Rodagon Smart Focus 80 mm (Figure 3.16). VIC-Snap software acquired images at a rate of 20 frames per second, resulting in sufficient detailed data from every test. The synchronization between the load-displacement curves and the images (i.e., associating the load and displacement values to the image at the same instant that each image was captured) was carried out with the VIC-Snap software. VIC3D 9 was used to analyze the images. To minimize the processing time and the amount of data collected, making the correlation analysis feasible, it was required to restrict the frame that the software processes to a smaller area of interest surrounding the specimen. The software generates a rectangular array of subsets inside the area of interest during this operation. Subsets are square portions of the picture, spaced by the same distance (the step size) both in vertical and horizontal directions. Here, subset size is 47 pixels and a subset spacing is 5 pixels (Figure 3.17).

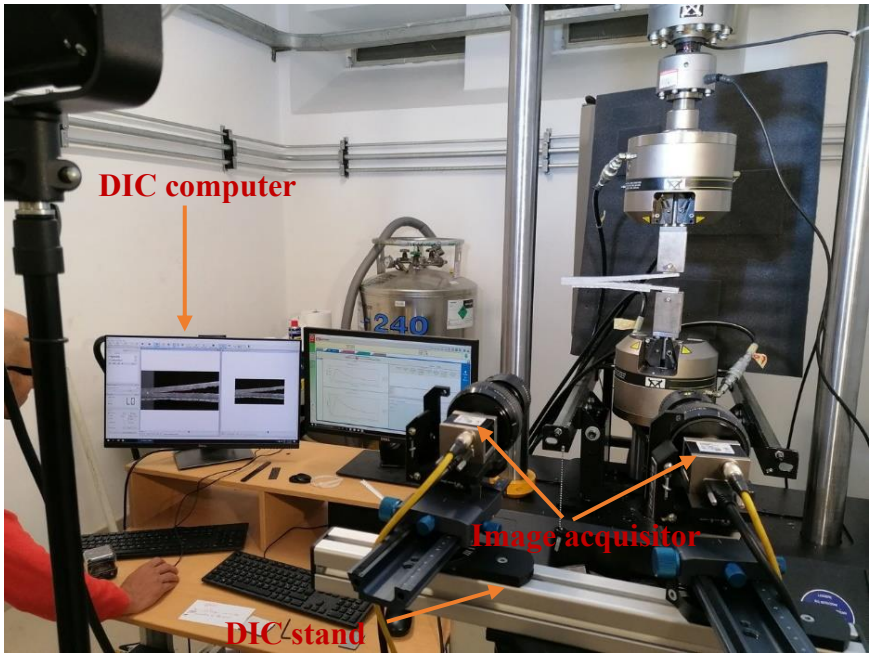

Figure 3.15 Digital Image Correlation (DIC) system

Establishing the DIC system is an intricate and laborious procedure. The system requires the assembly of several components in order to work correctly. The DIC system has many key components, including the acquisition system or data collection system, which must be coupled to the extremely sensitive cameras via appropriate channels (Figure 3.18). Additionally, it is necessary for the acquisition system to be synced with the Instron machine in order to accurately retrieve the same data (Figure 3.18). Furthermore, it is crucial to choose lenses meticulously in order to get photos that possess the appropriate focus and brightness. The MacVis program that is installed on the DIC computer helps choosing the right lenses. The number of cameras used in a DIC system may change based on the topic and the user's preference, since it allows for both 2D and 3D image acquisition and analysis. In 2D mode it is important that the camera be perpendicular to the specimen. Then in the postprocessing software by assigning a known distance between two points in a reference image the software automatically converts the pixels to mm. Contrarily, in 3D mode, two cameras must be employed. It is better to position them symmetrically with respect to the specimen. In 3D mode, before starting the test the calibration process should be done. Using the proper targets (Figure 3.19) provided by the manufacturer calibration becomes possible. The proper target should be chosen based on the specimen dimensions. At least 15 images are required for good calibration. According to the DIC manual the projection error under 0.1 is

acceptable. However, based on experience a projection error under 0.03 would provide precise results.

Figure 3.16 Rodagon 80 mm lenses

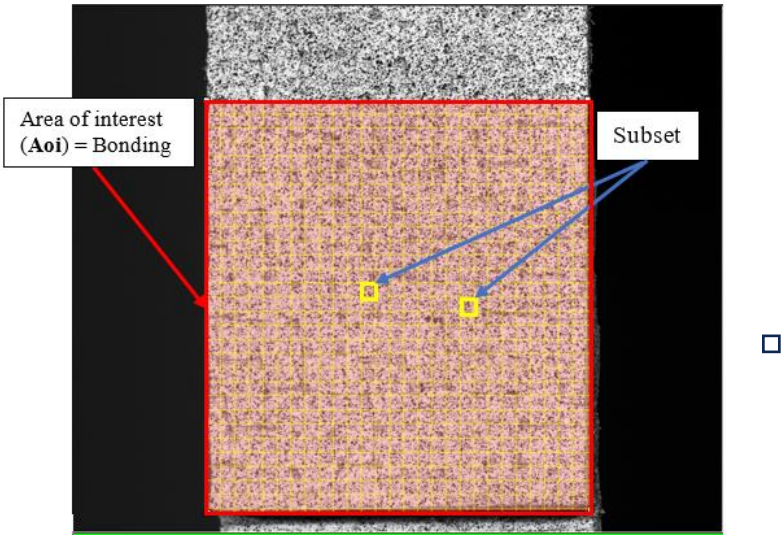

Figure 3.17 VIC-3D setting up

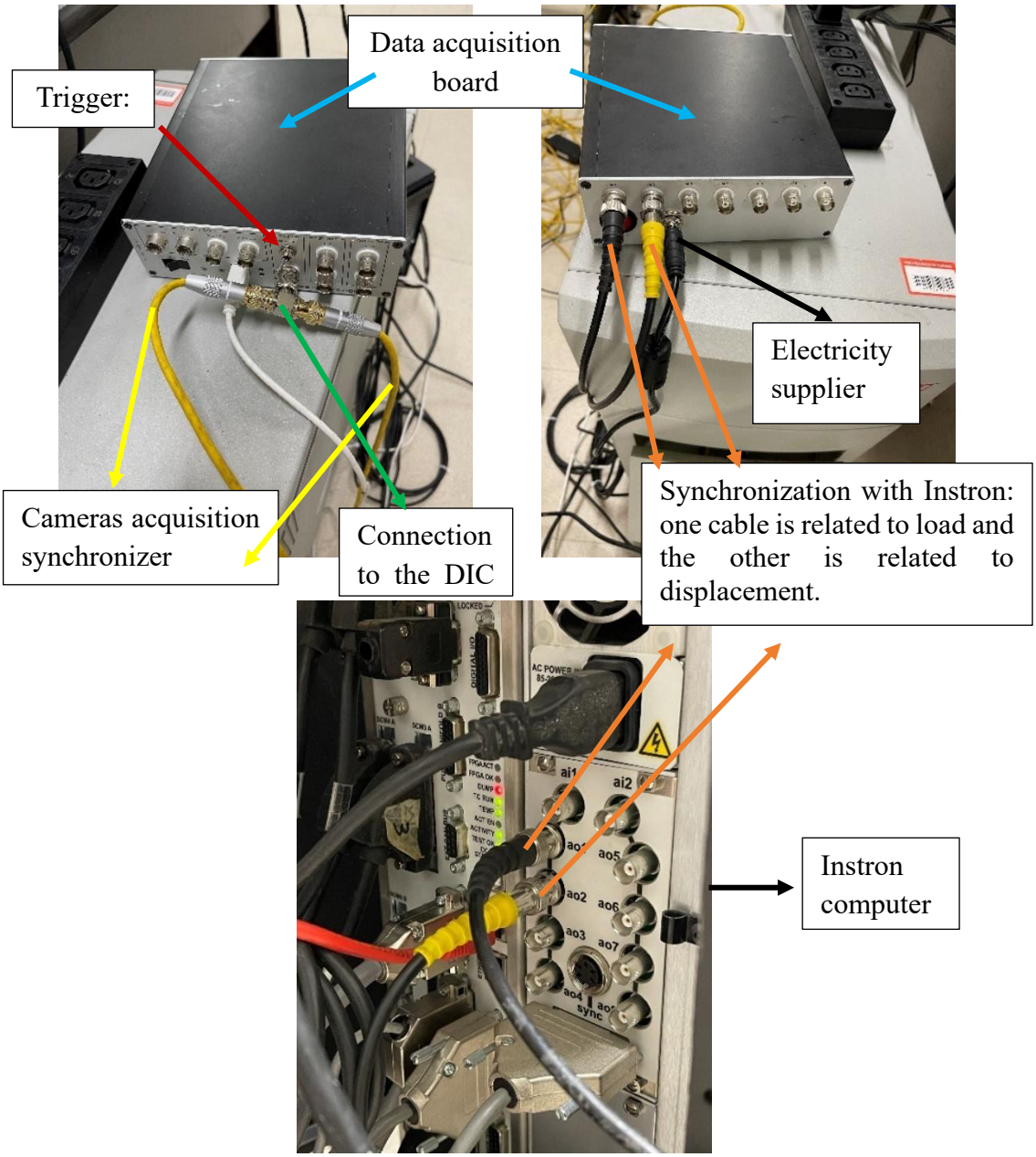

Figure 3.18 DIC acquisitor board

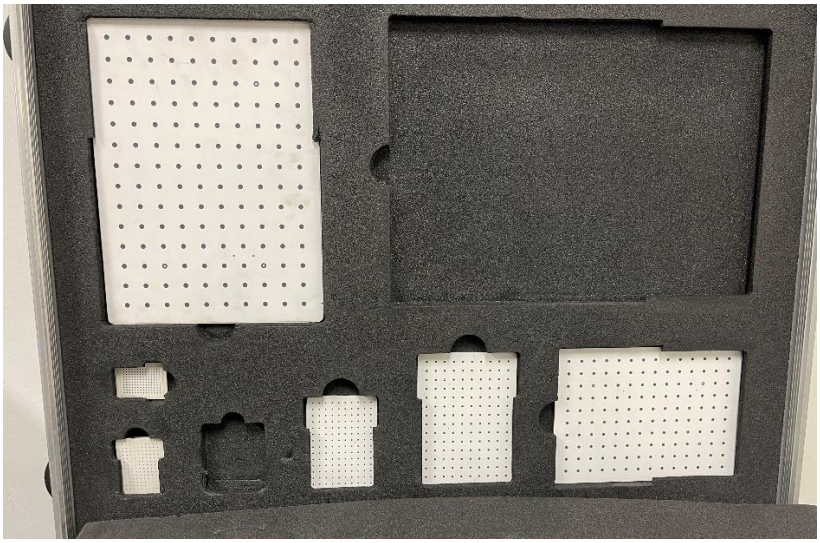

Figure 3.19 Calibration targets for the DIC

Finally having every connection done and calibration performed, it is time to adjust the light in order not to have an overexposed surface. In Vic-Snap image acquisition software, it is made possible to visualize if the light and focus have been set up correctly. As can be seen in Figure 3.20 when the contour map tends to be purple it means that everything is alright, and the test can be performed.

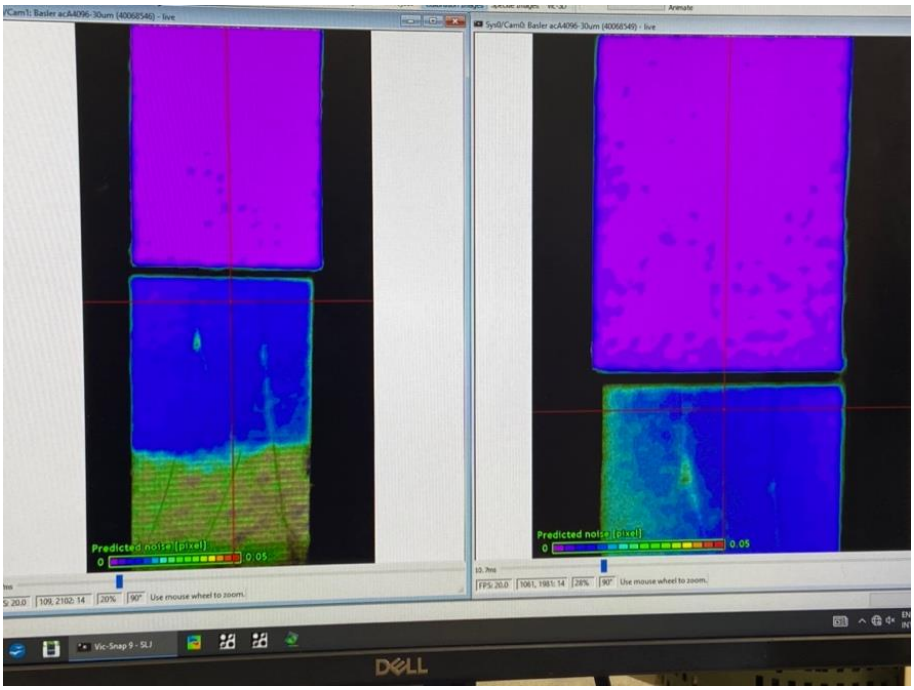

Figure 3.20. Light and focus counter map in Vic-Snap

In a nutshell using the DIC demands:

- Image Acquisition: DIC requires high-resolution digital images of the specimen's surface before and after deformation. These images are typically captured using cameras with suitable lenses and lighting setups to ensure clear visualization of the speckle pattern.
- Speckle Pattern Application: Prior to testing, a speckle pattern is applied to the surface of the specimen. This pattern can be created using spray paints, stickers, or other techniques that produce a random distribution of high-contrast features.
- Image Processing: The acquired images are processed using DIC software, which performs a series of steps including image alignment, correlation analysis, and deformation calculation. The software identifies corresponding points between the reference and deformed images based on the speckle pattern.
- Displacement and Strain Calculation: Once corresponding points are identified, the software calculates the displacement and strain fields across the surface of the specimen.

3.3.5. Fiber Optic Sensors (FOS)

The Odisi 6100 series is a multifunctional data collection system that is able of effectively monitoring and recording changes in both strain and temperature during mechanical testing. The system employs optical fibers for data collection and has a high level of sensitivity. The measuring setup is highly sophisticated, with a minimum gauge length of just 0.65 mm. This enables precise data collection and guarantees improved spatial accuracy in comparison to conventional strain gauges. The Odisi series, produced by LUNA (USA), is employed in several industrial sectors such as defense, aerospace, optical equipment production, and fiber optics. The particular version employed in this experiment is LUNA Odisi 6102. The package comprises a suitcase housing an Optical Distributed Sensor Interrogator, a specific instrument controller, multiple standoff cables, remote modules, a connection cleaner, and charging cables.

To set up the tool, a specific sequence of steps must be followed. The circuit connects one end of an optical fiber to a terminal while the other end is linked to a pigtail. The pigtail, seen in Figure 3.21, serves as a channel for transferring the signal and records the change in specimen strain. The pigtail is linked to the remote module (Figure 3.22a) which is connected to the acquisition board (Figure 3.22c)

through the standoff cable (Figure 3.22b). the final element that helps form a closed circuit is the acquisition board which is connected to the controller using a laptop as shown in Figure 3.22d.

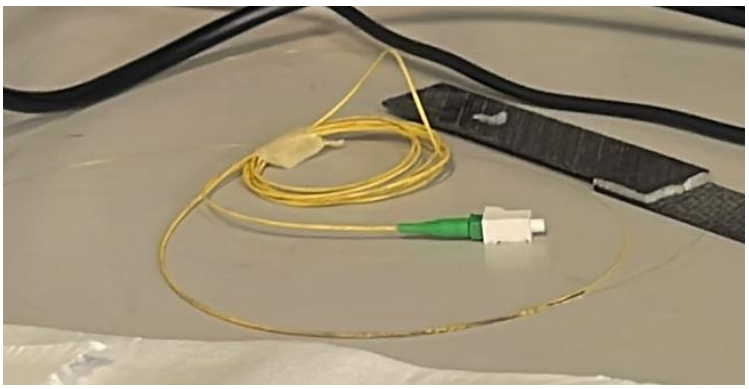

Figure 3.21 Pigtail (connector of the fiber to the remote control)

An essential consideration is the regular maintenance and cleaning of the connections. Therefore, the manufacturer includes a specialized connector cleaner as part of the complete setup. This is utilized to clean the standoff cable terminations and the pigtail. It has been noticed that the final signal reading is significantly lower in terms of clarity and confidence, when the connections are not clean enough.

Following the physical setup, the initial step is to verify the functionality of the fiber connection. Ensuring the connections between the pigtail and the terminal is crucial due to the high sensitivity of the optical fiber. This phase is an essential prerequisite that aids in the identification of signal transmission, termination loss, and fiber breakage. For example, Figure 3.23 illustrates that the signal near the fiber terminal is weak. Despite having done all the steps and formed the entire circuit, the end outcomes will not meet the anticipated expectations. It is advisable to establish a fresh connection in this scenario and subsequently reevaluate its quality.

According to the concept of measurement, the gauge length, which refers to the length of the optical fiber that contains points of measurement, is one of the most essential characteristics. Due to the great sensitivity and precision of the system that is being discussed, the gauge length that is considered to be the smallest feasible value is 0.65 millimeters. It is possible to define gauge length in a straightforward manner as the shortest distance that exists between the two points from which the system is able to gather data. The gauge length may be extended further in integer multiples of the lowest gauge length that the system allows, such as 1x0.65, 2x0.65, 3x0.65, and so on, depending on the size of the specimen and the sample requirements. This is executed in compliance with the established system. The

controller automatically determines the acquisition frequency as either 20Hz, 32.5Hz, or 62.5Hz, based on the length of the optical fiber. The acquisition frequency of the Luna Odisi-B must be perfectly synchronized with either the Instron acquisitor or the DIC acquisitor. This facilitates the final data analysis.

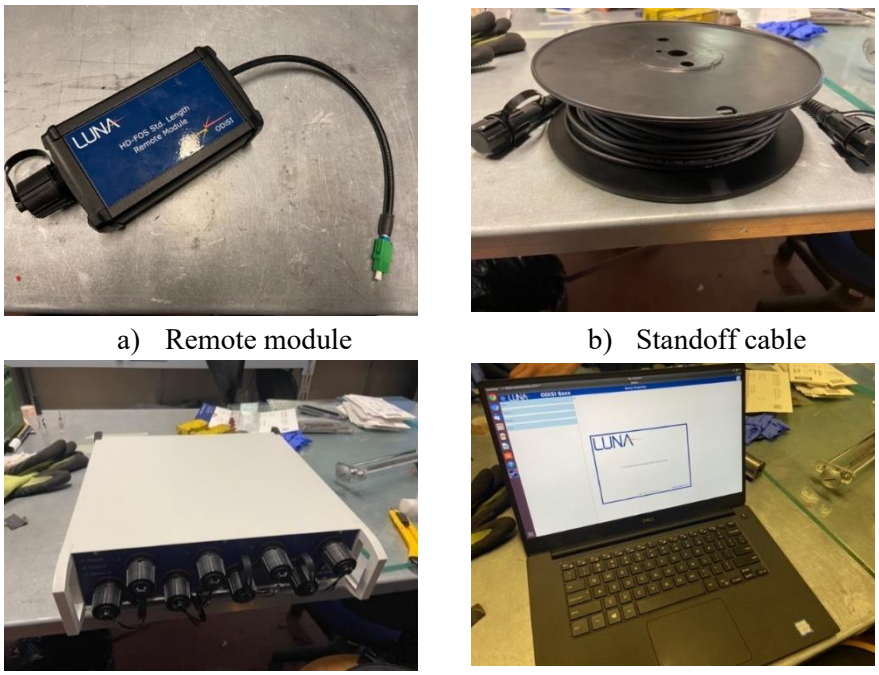

a) Remote module b) Standoff cable

c) Acquisition Board d) controller

Figure 3.22 Luna acquisitions system

Figure 3.23 Strain signal passage through an Optokon fiber

3.3.5.1. Optical fiber types

This investigation makes use of two distinct kinds of optical fibers, each of which comes from a different manufacturer. The characteristics and dimensions of these two are distinct from one another. Each of these fiber types has been covered here.

- **ThorLabs Polyimide-coated single-mode optical fiber:**

The market name of this product is SM1550P - Single Mode Optical Fiber. It has a numerical aperture (NA) of 0.12 ± 0.02 and operates at a wavelength range of 1310 - 1550 nm. The fiber is coated with polyimide and has a cladding diameter of Ø125 µm. It can be utilized at temperatures up to a maximum of 3500 °C due to the presence of a Polyimide covering in SM1550P as a shield and safeguard for the optical fiber. The permissible range of spectrum utilization in telecommunication applications is extensive. This is owing to the excellent concentricity between the core and cladding, which allows for a very high resolution of signals. In addition to its high-temperature capabilities, this fiber also exhibits chemical resistance and can be utilized in a vacuum condition. These properties make it an excellent option for applications in the aerospace, medical, and military sectors. For more detailed specifications the manufacturer website can be consulted [111]. Figure 3.24a and Figure 3.24b display the fibers and terminals (coreless fiber) that were utilized in the experimentation.

a) Optical fiber b) Optical fiber termination (coreless)

Figure 3.24 Optical fibers by ThorLabs

- **Optokon single mode fiber. G.657.A1 200µm:**

The coating of this fiber consists of two layers of UV-cured acrylate and has a cladding diameter of Ø125 µm. It operates at a wavelength range of 1310 - 1625 nm. The manufacturer advises that the fiber should be straightened after unwinding from the coil in order to get a satisfactory outcome. For a more detailed specifications of this fiber (Figure 3.25) the manufacturer's website [112] can be consulted. When comparing the two types of fibers, it was seen that dealing with the Optokon fiber is somewhat easier than dealing with the fiber produced by Thorlabs. The Thorlabs fiber is highly fragile, requiring extreme caution while removing the polyimide covering. However, in terms of precision, the Thorlabs fiber surpasses others and is therefore an excellent pick.

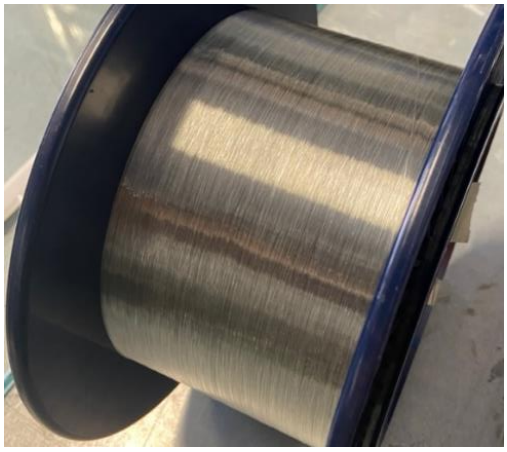

Figure 3.25 Optical fiber manufactured by Optokon

3.3.5.2. Fiber splicing, fiber fusion and fiber termination

Splicing refers to the act of connecting two fiber optic strands together. Taking advantage of this procedure it is possible to fix a broken fiber or lengthen a fiber. Furthermore, while connecting a fiber to a pigtail (a connection for the remote control, as shown in Figure 3.21) or creating a terminal, it is necessary to utilize a splicer. The Fujikura 90S+ splicer (Figure 3.26) is utilized.

There are two open ends in a fiber, one of which connects to a pig tail which makes the connection with the acquisition system and the other end connects to a coreless fiber called terminal. Pigtails are used to be spliced with optical fiber in order to make the connection with the acquisition system. The fiber, on the other hand, must first be cleaved using a cleaver before the splicing process may take place according to Figure 3.27. The cleaving process entails eliminating the fiber's coating and subsequently cutting the fiber with a cleaver to create an effective

fusion surface. It is essential that the cut be straight in terms of angular accuracy; otherwise, the loss will be far more than the amount that is permitted.

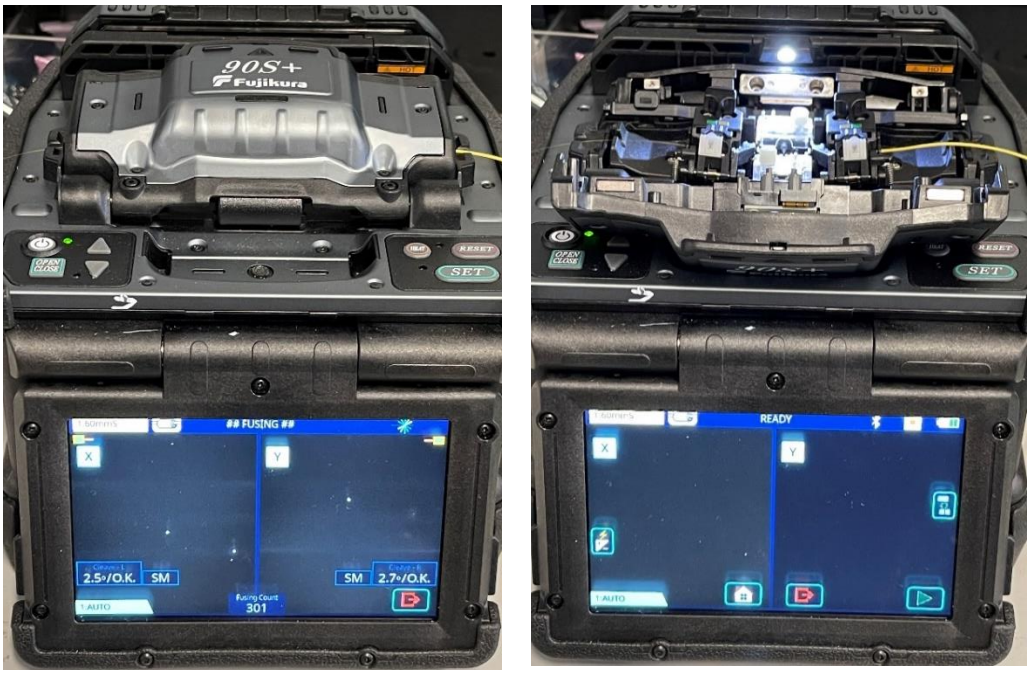

a) Splicer with the fiber fusion lid closed b) Splicer with the fiber fusion lid open

Figure 3.26. Splicer

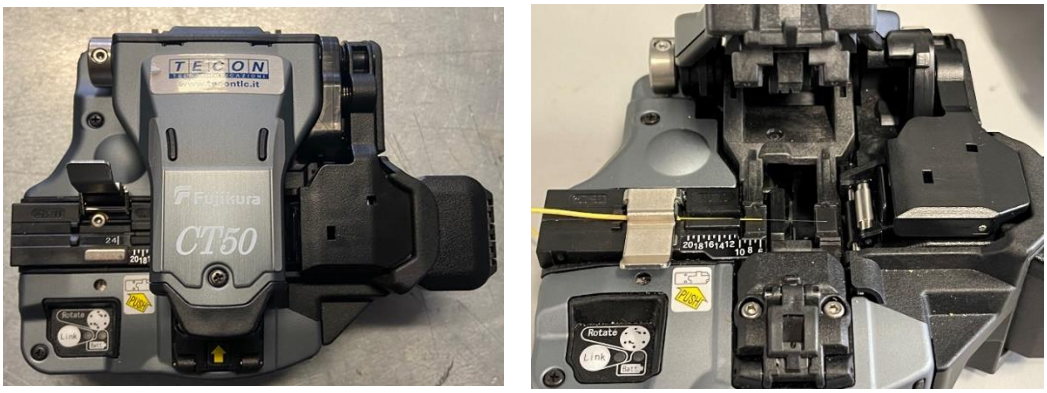

a) Cleaver with closed lid b) Cleaver with fiber placed inside

Figure 3.27 Cleaver used to cut the fiber with almost a flat cross-sectional area

Prior to commencing the fiber splicing procedure, it is imperative to ensure that the surface of the cut is suitably smooth, and the fibers are free from any dust

particles. If the splicer fails to fuse the fibers, the machine displays an error, and the process remains incomplete. The fibers are cleaned in order to get excellent results using cotton tabs and isopropyl alcohol. The entire splicing process may be observed on a screen that utilizes the integrated camera in the device (Figure 3.28).

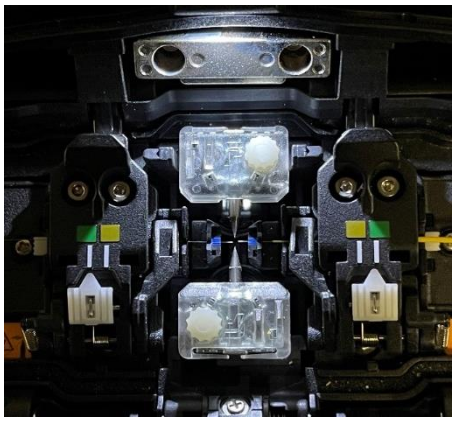

a) Placing the cleaved fibers in the slicer

b) Bringing the fibers near each other

c) A moment before the fusing starts

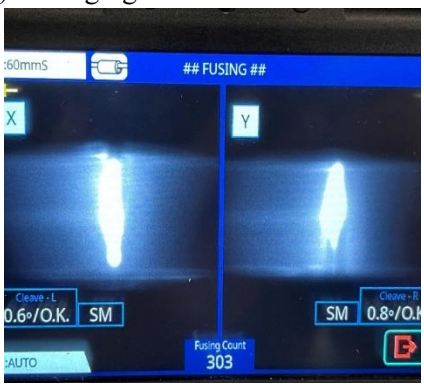

d) Fusing phase

e) Splice fiber with a loss of zero

Figure 3.28 Fusion process of the fibers using splicer

The two fibers that are to be spliced are positioned in close proximity with their cut sides facing each other (Figure 3.28a). Afterwards, the splicer lid will be automatically shut, and an internal motor will pull the two fibers into close proximity to each other (Figure 3.28b) in order to be fused. Additionally, the alignment of the fibers with regard to one another is a factor that decides how the fusion process will proceed. Once all of these limitations are resolved, the splicing process occurs (Figure 3.28 c and d). Once the fusion is completed, the fiber is now prepared to be removed (Figure 3.28e).

Once the two fibers are joined, the fusion region can be either coated with a plastic layer for protection or left exposed. Typically, if the test is conducted immediately after the specimen is prepared, it is recommended to leave it uncovered since it does not impact the quality of the spectrum obtained. Alternatively, it is advisable to maintain the connection concealed. To protect the fusion area, the fiber should be run through a fusion protection sleeve made of plastic so that the plastic sleeve covers the fusion area. For the next step, it is necessary to subject this sleeve to heat (heat shrink wrap process) using the specified component of the splicer (Figure 3.29a). Ultimately, the fused fiber is also safeguarded by the sleeve (Figure 3.29b).

a) Exposing the fiber fusion area with the plastic cover to heat

b) Fusion area protected by plastic cover

Figure 3.29 covering the fiber fusion area

Chapter 4

4. Numerical and theoretical modelling[1]

In this chapter, firstly, the finite element modelling of SLJs with polyurethane adhesives is explained in terms of material cards, contacts, boundary conditions, element type, and mesh size. Then the procedure to estimate the adhesive cohesive parameters using SLJ experimental test, SLJ FEM, and optimization method is described. This information is a prerequisite to perform Task 3. On the other hand, the details of Bigwood and Crocombe analytical model is mentioned. Employing this model the strain on the backface of the SLJ substrates can be calculated. This analytical model is used in Task 4.

4.1. Finite Element Modelling

4.1.1. Simulation and optimization: LS-DYNA and LS-OPT

LS-DYNA and LS-OPT are software tools developed by Livermore Software Technology Corporation (LSTC) [113] that play crucial roles in various engineering

[1] **The content of this task is already published as methodology part of papers [10–13]. Minor changes have been made on grammar, formatting, and the synchronization of the list of references in order to integrate the papers within the dissertation.**

disciplines. While LS-DYNA focuses on simulation, LS-OPT excels in design optimization.

LS-DYNA solver analyzes the response of structures and materials under static and dynamic loading conditions, including impacts, explosions, and crashes. This capability makes it valuable for simulating real-world scenarios where structures experience static or high-speed deformations and energy transfer. Moreover, it supports a wide range of material behaviors like plasticity, damage, and failure, allowing for accurate simulations of complex materials, such as metals, composites, and biological tissues. This enables engineers to create realistic models that capture the true behavior of materials under diverse loading conditions.

LS-OPT, on the other hand, is a Design optimization tool which Optimizes design parameters of an LS-DYNA model based on specified objectives and constraints. This allows engineers to automatically search for designs that meet specific performance criteria, such as minimizing weight, maximizing strength, or improving fuel efficiency. In addition, it employs various algorithms like gradient-based, evolutionary, and metaheuristic approaches to find optimal solutions. This broad range of algorithms ensures that LS-OPT can tackle diverse optimization problems with varying complexities. Besides, LS-OPT is a multi-objective optimization software that can handle problems with multiple conflicting objectives, providing trade-off solutions. This is beneficial for real-world scenarios where engineers need to balance different design goals, such as achieving high strength without sacrificing lightweight design. More importantly, LS-OPT seamlessly integrates with LS-DYNA, automatically running simulations and feeding results back into the optimization process. This tight integration eliminates manual interaction and simplifies the optimization workflow, saving time and effort. Therefore, LS-DYNA and LS-OPT form a powerful combination for simulation and optimization.

4.1.2. Modelling specification

An explicit nonlinear finite element analysis has been performed using LS-Dyna software. The composite adherends were modeled with four-node shell elements and the layers were modeled using the keyword *Composite Parts in two directions of 0°/90°. The thickness of each layer is 0.44 mm. The material model used to simulate the adherend is *Mat_Enhanced_Composite_Damage (MAT_54/55)[114]. In this material model, both Chang-Chang and Tsai-Wu damage criterion are embedded, but the one used in this research is Chang-Chang.

It is worth noting that all the substrates remained in the elastic region. The material card parameters are provided in [9] and [110] where the authors simulated the mechanical behavior of composite crash absorbers and composite substrates respectively, by finding a good agreement between experimental and numerical simulations. On the other hand, the adhesive is modeled using eight-node solid (not zero-volume) cohesive elements with element formulation 19 together with *Mat_Cohesive_General (MAT_186) which gives the possibility to use a normalized arbitrary shape of Cohesive Law [114] (Figure 4.1). The *Contact_Tied_Shell_Edge_To_Surface_Constraned_Offset was used as the contact algorithm between the shell composite substrate and the solid cohesive elements [115]. The parameters for this material card were obtained in LS-Opt environment and the results are explained in section 7.1. Based on the experimental load-displacement curve obtained in the experimental SLJ tests, it was decided to use a trapezoidal cohesive law.

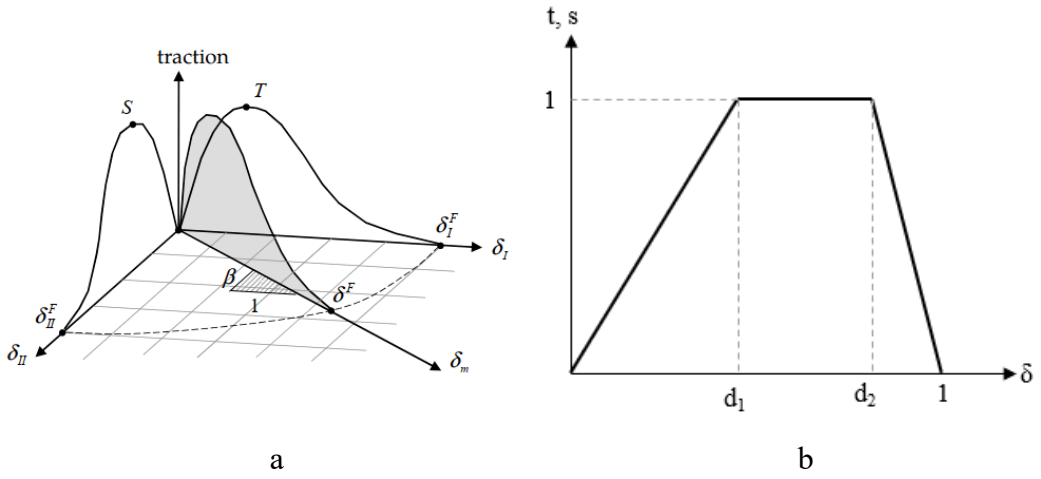

Figure 4.1. a) Generic cohesive law [114]; b) Trapezoidal cohesive law

The boundary and the loading conditions of the numerical simulations are similarly set as the ones in the experimental test. The extremity of one adherend was clamped and a prescribed motion law was applied to the other adherend, in a way that the moving nodes are only allowed to move straight in the x direction. The motion is applied through a velocity-time law which is characterized by an initial ramp, then followed by a constant value of the velocity, as done in [116]. Apart from these, a 2.5-mm mesh size was adopted for the adherends in the region far from the bonded area. However, in proximity to the overlap zone, the mesh of adherends and adhesive was refined to the mean value of 0.5-mm because in this area the stress distribution could be more critical (Figure 4.2). The mesh sensitivity

of the model was checked by considering 3520, 14080, and 56320 elements and the results (load-displacement curves) were negligibly different. Therefore, the mesh size of 3250 elements which has the lowest cost was chosen.

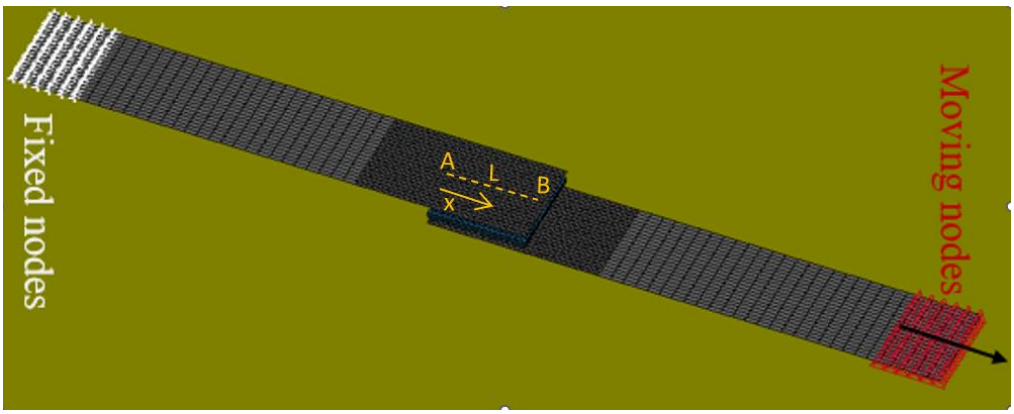

Figure 4.2. FEM model in LS_Dyna

4.1.3. Analysis of Variance, optimization, and model calibration

The mechanical properties of an adhesive like G_{Ic}, G_{IIc}, maximum traction (t), and shear (s) stresses are of great importance to perform a successful finite element analysis of an adhesive joint using CZM method. In this regard, Reis et al. [70] showed that in a single lap joint with more rigid substrates a higher shear stress was observed which means the joint is mainly affected by mode II. Therefore, the SLJ with the highest substrate thickness (T3) was considered as the reference experimental test to perform the Analysis of Variance (ANOVA) and the optimization. In this case, the effect of mode I on the failure of the joint is reduced and the most important parameters are expected to be G_{IIc} and s. An ANOVA was performed based on the mentioned parameters using the LS-Opt to verify it. As expected, the results revealed that mode II parameters are the most influencing parameters (this is discussed in section 7.1). Another equally important parameter is d_1, displacement at damage initiation in cohesive law because this parameter influences the initial trend of the numerical curve and thus the stiffness of the joint. Therefore, only G_{IIc}, s, and d_1 have been considered in the optimization analysis and to model the mechanical behavior of the SLJ joint prepared with the thickest substrate layer. The parameter d_2=0.6 was preliminary and iteratively found to set a constraint on the final rupture of the adhesive joint. This preliminary analysis and constraint were needed since the experimental SLJ load-displacement curves at

failure do not present a linearly decreasing trend, thus, the trapezoidal behavior does not match the experimental curve when the rupture is reached. The chosen normalized value d_2=0.6 allows having a good match between numerical and experimental results at rupture.

On the other hand, the peel stress t, and the corresponding energy release rate G_{IC} have been defined by using the same assumptions adopted in [117]. The maximum peel component, t, is assumed equal to the double of the maximum shear stress, in accordance with the Tresca criterion. This assumption is valid here as the adhesive and the substrates are very similar to reference [117]. Anyhow, the most important parameters proved to be the ones related to mode II, thus this assumption is acceptable. Further, G_{IC} was found by comparing the experimental curves, G_{IC} and G_{IIC} vs. crack length, which are reported by Banea et al. [118] and Leal et al. [119]. They reported that G_{IC} is approximately equal to one quarter of G_{IIC} for similar polyurethane adhesives. DCB tests were adopted to verify whether the G_{IIC} obtained in the optimization procedure was comparable to those found experimentally.

To numerically replicate the mechanical behavior of the single lap joint tests, the load-displacement curve related to specimen L2W2T3 has been chosen as the experimental reference curve. Afterward, a surrogate model-based optimization [117,120] has been carried out to minimize the difference between the numerical load-displacement output curve and the experimental reference curve. The optimization model uses the Mean Square Error (MSE) criterion and can be defined as follows:

$$\min_x MSE = \frac{1}{n}\sum_{k=1}^{n}\left(\frac{f_k(x) - H_k}{M_k}\right)^2$$
$$8<x_1<20$$
$$7<x_2<16$$
$$0.1<x_3<0.6 \qquad (4.1)$$

where $x = (x_1, x_2, \text{and } x_3)$ are the variables describing G_{IIC}, s, and d_1, respectively. n is the number of points. H_k, (k = 1, …, n) are the values of the reference load-displacement curve (experimental test), and $f_k(x)$ stands for the corresponding computed curve obtained by FEM. M_k is the maximum absolute difference between the target value and the computed value, i.e., M_k = max | $f_k(x) - H_k$|. In LS-Opt, both load and displacement are extracted and drawn versus each other as a numerical load-displacement cross plot, and the reference load-

displacement curve is called as a history file. Having these two curves now it is possible for LS-Opt to calculate the MSE. In this optimization problem, a Sequential Response Surface Method (SRSM) [121] is used as a metamodel-based optimization method as well as the Kriging approximation method [120] as the metamodel. This optimization is performed with 4 iterations to properly describe the mechanical behavior of the joints. Each iteration contains 12 sampling points. Therefore, 48 samples are stochastically disposed in the design domain.

4.2. Bigwood and Crocombe analytical model (Used in Task 4)

D.A. Bigwood and A.D. Crocombe [122] formulated a detailed elastic model capable of assessing the internal stresses within the adhesive material in single lap joints, namely shear stress τ_{xy} and transverse (peel) stress σ_y. This model describes each joint as the sandwich structure shown in Figure 4.3. It consists of two adherends and the adhesive in between, subjected to various load combinations (including tensile, shear, and bending moment) applied at the adherends' edges. The analytical model is built based on the following assumptions: only the shear and peel stresses are considered in the adhesive, the stress in longitudinal direction is negligible; the adherends are in a plane stress conditions in the x-z plane (similar to flat plates under tension and bending) and in a plane strain condition in the x-y plane.

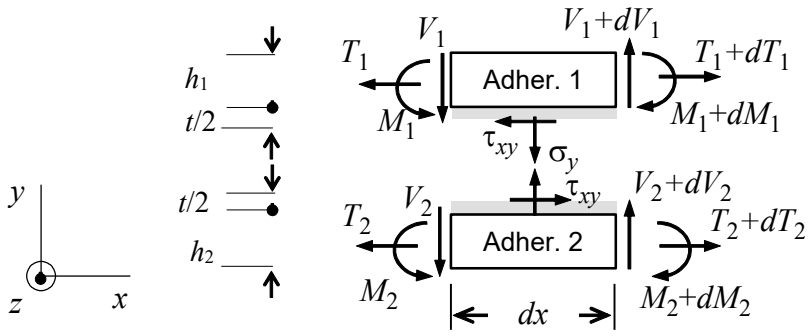

Figure 4.3. The general adherend-adhesive configuration used by Bigwood-Crocombe [122].

By applying equilibrium, compatibility and elasticity conditions, a pair of third- and fourth-order coupled differential equations are obtained. Through additional manipulation, two separate seventh- and sixth-order differential equations are eventually obtained:

$$\frac{d^7\tau_{xy}}{dx^7} - k_1\frac{d^5\tau_{xy}}{dx^5} + k_3\frac{d^3\tau_{xy}}{dx^3} - k_5\frac{d\tau_{xy}}{dx} = 0 \tag{4.2}$$

$$\frac{d^6\sigma_y}{dx^6} - k_1\frac{d^4\sigma_y}{dx^4} + k_3\frac{d^2\sigma_y}{dx^2} - k_5\sigma_y = 0 \tag{4.3}$$

Here, $k_5 = (k_1k_3 - k_2k_4)$, the coefficients k_1 *to* k_4 can be determined from the mechanical and geometrical characteristics of both the adhesive and the substrates. The general solution of these two equations is as follows:

$$\begin{aligned}\tau_{xy} = {} & C_1\cosh(m_1x) \\ & + C_2\sinh(m_1x) + C_3\cosh(n_1x)\cosh(n_2x) \\ & + \quad C_4\cosh(n_1x)\sin(n_2x) \\ & + C_5\sinh(n_1x)\cos(n_2x) + C_6\sinh(n_1x)\sin(n_2x) + C_7\end{aligned} \tag{4.4}$$

$$\begin{aligned}\sigma_y = {} & D_1\cosh(m_1x) \\ & + D_2\sinh(m_1x) + D_3\cosh(n_1x)\cosh(n_2x) \\ & + \quad D_4\cosh(n_1x)\sin(n_2x) + D_5\sinh(n_1x)\cos(n_2x) \\ & + D_6\sinh(n_1x)\sin(n_2x)\end{aligned} \tag{4.5}$$

where m_1, n_1, n_2 are argument multipliers, $C_1, \ldots, C_7$ and $D_1, \ldots, D_7$ are constants depending on the boundary conditions. The procedure to obtain these parameters is given in detail in [122].

Starting from the Bigwood and Crocombe adhesive stress analysis, the authors of this paper analytically implemented in the model the possibility of obtaining the strains in the backfaces of the adherend, in order to compare them with the experimental results. The strains in the adherends are caused by the two contributions of tensile force and bending moment. To assess their distribution in adherend 1 (on which the DIC measurement is performed), starting from the distributions of τ_{xy} and σ_y, respectively given by equations (4.4) and (4.5), the three conditions of axial, transverse, and rotational equilibrium are written:

$$T_1(x) = T_{11} + \int_0^x \tau_{xy}dx \tag{4.6}$$

$$V_1(x) = V_{11} + \int_0^x \sigma_y dx \tag{4.7}$$

$$M_1(x) = M_{11} + V(x)x - \int_0^x \tau_{xy}dx\frac{(t+h_1)}{2} - \int_0^x \sigma_y x dx \tag{4.8}$$

where T_{11}, V_{11}, and M_{11}, are, respectively, the tensile force, the shear force and the bending moment applied to the left end (x=0) of adherend 1. Note that the forces and the moment are per unit width.

After the evaluation of the tensile force and of the bending moment has been achieved, the related normal stresses are evaluated by means of equation (4.9) and (4.10), respectively:

$$\sigma_{xT1} = \frac{T_1(x)}{h_1} \tag{4.9}$$

$$\sigma_{xM1} = \frac{M_1(x)}{\frac{1}{12}h_1^3} \cdot \frac{h_1}{2} \tag{4.10}$$

The calculation of the stresses in adherend 2 can be obtained in a similar manner and is not reported for the sake of brevity.

Figure 4.4a illustrates the normal stresses within the adherends, depicting the stress due to the tensile force (σ_{xT} in Figure 4.4a) and the stress due to the bending moment (σ_{xM} in Figure 4.4a). A significant aspect to note is the sign of the stresses on the outer surfaces of the adherends. Moreover, a schematic from the effect of load eccentricity on SLJs is shown in Figure 4.4b. It can be seen from Figure 4.4 that the strain caused by tensile load is always positive, but the strain caused by the bending moment could be both positive and negative.

Assuming that $T_{1,2}$ and $M_{1,2}$ are positive, the upper surface of the upper adherend (1) undergoes positive stress contributions, while the lower surface of the lower adherend (2) undergoes a positive stress due to the tensile force and a negative stress due to the bending moment. Considering that each adherend is in plain stress conditions, the equation to evaluate the strain is:

$$\varepsilon_{x1,2} = \frac{(1-\upsilon^2)}{E}\left(\sigma_{T1,2} \pm \sigma_{M1,2}\right) \tag{4.11}$$

where the stresses due the tensile force and bending moment are given by, respectively, equations (4.9) and (4.10) for adherend 1 and by the analogous pair of equations for adherend 2.

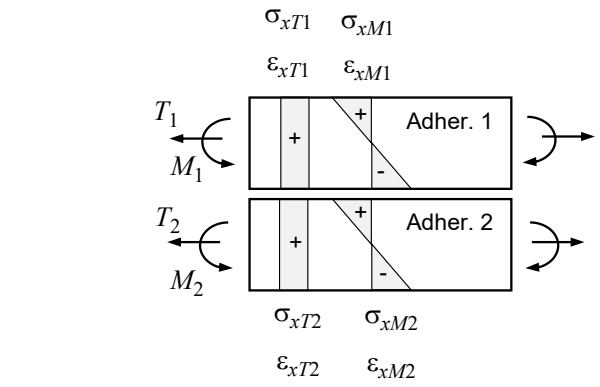

a)

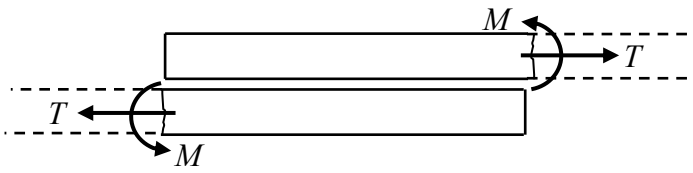

b)

Figure 4.4. Bonded joint subjected to general tensile and moment loading: a) stress and strain in the adherends in the overlap [122]; b) actual tensile force and bending moments in the joint ends due to the load eccentricity.

Chapter 5:

5. Characterization of adhesive mechanical properties[1] (Task 1)

This chapter explains the results obtained from both adhesives' dogbone, DCB and ENF tests. Additionally, before presenting the results of DCB and ENF tests the related data reduction schemes are provided to calculate energy release rate in mode I and II. These results are useful to be implemented in finite element modelling.

5.1. Tensile tests on dogbone specimens

At least five dogbone (Figure 5.1) specimens were tested for each adhesive. The stress-strain curves of the proper specimens are shown in Figure 5.2. The polyurethane adhesive shows a bilinear behavior, i.e., after the primary elastic part the material behaves again linearly, with a smaller slope, up to fracture. On the other hand, epoxy adhesive demonstrates an elastic-perfectly plastic behavior, i.e., it reaches a plateau after the first elastic part. The mechanical properties taken out from this figure are given in Table 5.1. All the tests were performed at a velocity of 5 mm/min, which on a gauge length of 20 mm gives a strain rate of ~ 0.004 ($\frac{1}{s}$).

[1] **The content of this task is already partially published as papers [10–13]. Minor changes have been made on grammar, formatting, and the synchronization of the list of references in order to integrate the papers within the dissertation.**

Moreover, the test condition and specimens' dimensions are detailed in section3.1.1.

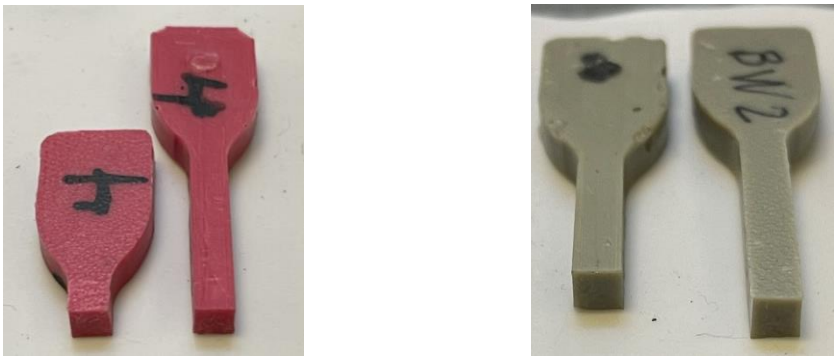

(a) (b)

Figure 5.1.Adhesive dogbone failure surfaces: (a) Epoxy (SIKAPOWER-1277); (b) Polyurethane (ADEKIT A 236/H 6236)

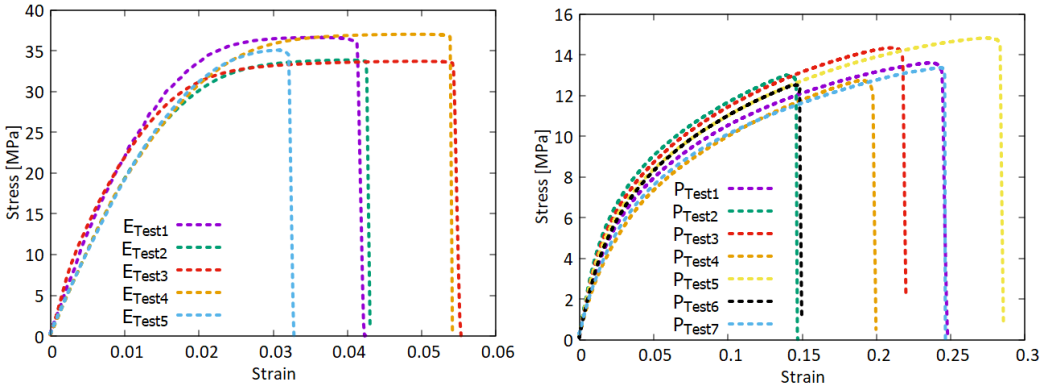

(a) (b)

Figure 5.2. Adhesives tensile tests: (a) Epoxy (SIKAPOWER-1277); (b) Polyurethane (ADEKIT A 236/H 6236)

Table 5.1**.** Mechanical properties of adhesives

Property	**Polyurethane (ADEKIT A 236/H 6236)**	**Epoxy (SIKAPOWER-1277)**
E (MPa)	278	2500
SIG ultimate (MPa)	13	35
Elongation (%)	22	4.1

5.2. Double cantilever Beam (DCB) tests

After the tests, the substrates were separated to control the failure surface of the specimens as shown in Figure 5.3. In case of epoxy adhesive, the failure surface is such that a relatively thicker adhesive residual can be seen on one substrate while a very thin layer of adhesive is observed on the surface of other substrate. In the case of polyurethane adhesive, the failure is cohesive, and the adhesive residual are well distributed on the surface of both substrates. All the tests were performed at a velocity of 5 mm/min. Moreover, the test condition and specimens' dimensions are detailed in section3.1.1.

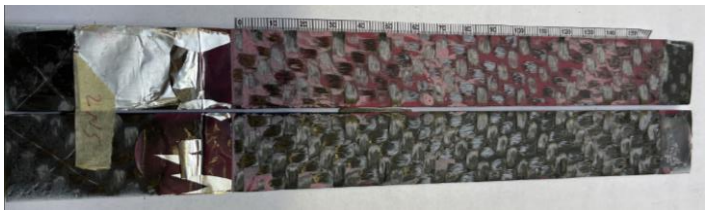

a) Epoxy

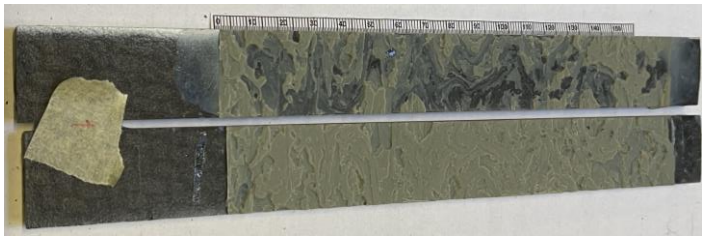

b) Polyurethane

Figure 5.3 DCB Specimen failure surfaces

5.2.1. DCB data reduction schemes

Having the DCB test done, energy release rate in mode one can be obtained employing proper data reduction schemes. There are different data reduction methods to assess the strain energy release rate (SERR). According to Irwin-Kies equation [123] the SERR, *G*, can be obtained by (5.1):

$$G = \frac{P^2}{2b}.\frac{dC}{da} \tag{5.1}$$

Where *P* is the applied load, a is the crack length, *b* is the joint width, and *C* is the specimen (adherends) compliance which is equal to *δ/P.* The parameter *δ* is the displacement corresponding to the load *P*. Furthermore, compliance is determined

by considering a cubic polynomial ($C = C_3a^3 + C_2a^2 + C_1a + C_0$) to fit the *C= f(a)* curves.

- **Simple beam theory (SBT):**

In this method, according to the references [108,124,125] the simple beam theory for a thin adhesive layer it can be found that:

$$\frac{dC}{da} = \frac{8}{E_S B}\left(\frac{3a^2}{h^3} + \frac{1}{h}\right) \tag{5.2}$$

Where h is the substrate thickness and E_s represents the independently measured flexural or tensile modulus of the substrate.

- **Corrected beam theory (CBT):**

The theoretical expression of compliance in a perfectly built-in DCB specimen, according to simple beam theory, tends to underestimate the actual compliance because real-world specimens are not perfectly built-in [108,126,127]

The adhesive fracture energy, G_{IC}, is determined using (5.4) when drill holes are employed for load introduction, or (5.4) when load-blocks are utilized.

$$G_{IC} = \frac{3P\delta}{2B(a+|\Delta|)}.F \tag{5.3}$$

$$G_{IC} = \frac{3P\delta}{2B(a+|\Delta|)}.\frac{F}{N} \tag{5.4}$$

Where F, the large displacement correction, and N, the load block correction are obtained by:

$$F = 1 - \frac{3}{10}\left(\frac{\delta}{a}\right)^2 - \frac{3}{2}\left(\frac{l_1\delta}{a^2}\right) \tag{5.5}$$

$$N = 1 - \left(\frac{l_2}{a}\right)^3 - \frac{9}{8}\left[1 - \left(\frac{l_2}{a}\right)^2\right]\frac{l_1\delta}{a^2} - \frac{9}{35}\left(\frac{\delta}{a}\right)^2 \tag{5.6}$$

In (5.5) and (5.4), l_1 is the distance from the center of the loading pin to the mid-plane of the arm of the substrate beam to which the load-block is attached, and l_2 is the distance from the loading-pin center to the edge of the block.

In the case of loading holes drilled directly through the substrate, the load-block correction factor, *N*, equals 1, and the parameter l_1 equals 0. The significance of the

large-displacement correction factor, *F*, arises when the ratio of displacement to crack length (δ/a) is greater than 0.4. Ideally, if the displacement correction factor, F, falls below 0.9, the test specimen should be reconfigured, such as by using thicker substrates, to minimize the necessary displacements and consequently reduce the impact of the large-displacement correction factor.

The correction term, |Δ|, can be determined experimentally by treating the beam as having a slightly longer crack length, (a + |Δ|). This involves plotting the cube root of the compliance, $C^{1/3}$, or the cube root of the normalized compliance, $(C/N)^{1/3}$ (if load-blocks are utilized), against the crack length, a, as depicted in Figure 5.4. The load-block correction, *N*, is defined in (5.6). By extrapolating a linear fit through the data points in the plot Δ is identified as the negative X-intercept. When conducting the linear fits, only the propagation (PROP) values need to be considered and all initiation values should be excluded from the analysis. For further information ISO 25217:2009 [108] can be consulted.

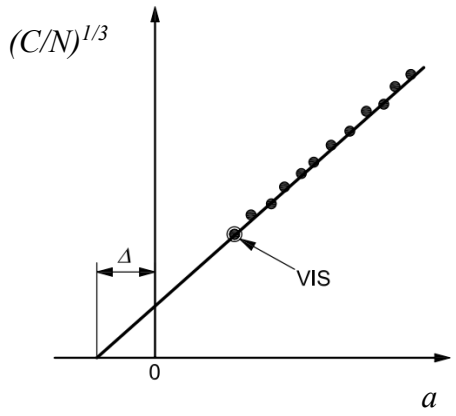

Figure 5.4. The linear fit correction for the CBT method for DCB test [108] (VIS is the first visualized deviation which should be excluded from the fit)

- **Compliance based beam method (CBBM)**

Previously mentioned methods demand measuring the actual crack length. In general, SERR is obtained based on (5.1). Applying the beam theory, the relationship between specimen compliance (*C*) and crack length (*a*) is established as follows:

$$C = \frac{\delta}{P} = \frac{8a^3}{bh^3E_1} + \frac{12a}{5bhG_{13}} \tag{5.7}$$

Where E_1 and G_{13} are the axial and shear modulus of the adherends, respectively.

SERR in mode I will be provided in (5.8) by combining (5.7) with (5.1):

$$G_I = \frac{6P^2}{b^2h^3}\left(\frac{2a^2}{E_1} + \frac{h^2}{5G_{13}}\right) \tag{5.8}$$

This technique does not consider factors like root rotation at the crack tip, stress concentration effects, and the existence of a significant Fracture Process Zone (FPZ) preceding the crack tip, all of which impact the *P-δ* curve. de Moura et al. [128] propose an alternative strategy by introducing the equivalent flexural modulus, E_f, instead of E_1 in (5.8), and the determination of an equivalent crack length (a_e) during testing. The equivalent flexural modulus (presented in (5.9) is derived from (5.7) considering the initial compliance C_0 and crack length a_0 instead of C and a, respectively:

$$E_f = \left(C_0 - \frac{12(a_0+|\Delta|)}{5bhG_{13}}\right)^{-1} \frac{8(a_0+|\Delta|)^3}{bh^3} \tag{5.9}$$

Δ serves as correction factor for the crack length in order to consider the impacts of root rotation. This correction factor can be derived from a linear regression equation, $C^{1/3} = f(a_0)$, which is calculated after examining samples with three varying initial crack lengths, as depicted in Figure 5.5 of the reference [128].

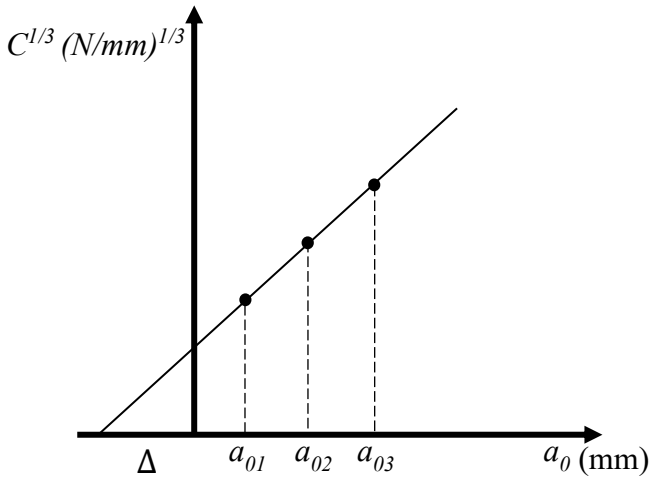

Figure 5.5 crack length correction

Wang and Williams [129] proposed another alternative to include the effect of root rotation by introducing the variable Δ_I:

$$\Delta_I = h\sqrt{\frac{E_1}{11G_{13}}\left[3 - 2\left(\frac{\Gamma}{1+\Gamma}\right)^2\right]} \tag{5.10}$$

where

$$\Gamma = 1.18\frac{\sqrt{E_1 E_3}}{G_{13}} \tag{5.11}$$

E_3 represents transverse modulus. In order to apply the de Moura correction to (5.10) and (5.11), E_1 should be substituted with E_f in these two equations. Now, Δ_I can be inserted in (5.9) instead of Δ. To obtain a converged E_f an iterative procedure should be followed between (5.9), (5.10), and (5.11).

In addition, it is necessary to take into account an equivalent crack length, a_e, when observing crack growth, to consider the effect of FPZ (Figure 5.6). Past research on mode II fracture has shown the significance of this effect, which becomes more important when dealing with ductile adhesives, as noted in reference [130]. The calculation of the equivalent crack length involves using a_e instead of the actual crack length a, based on the compliance of the specimen recorded during testing. The equivalent crack length, $a_e = a + |\Delta| + \Delta a_{FPZ}$, includes the effects of root rotation at the crack tip and the FPZ itself. With these adjustments, it is possible to derive the mode I SERR from (5.12):

$$G_I = \frac{6P^2}{b^2h^3}\left(\frac{2a_e^2}{E_f} + \frac{h^2}{5G_{13}}\right) \tag{5.12}$$

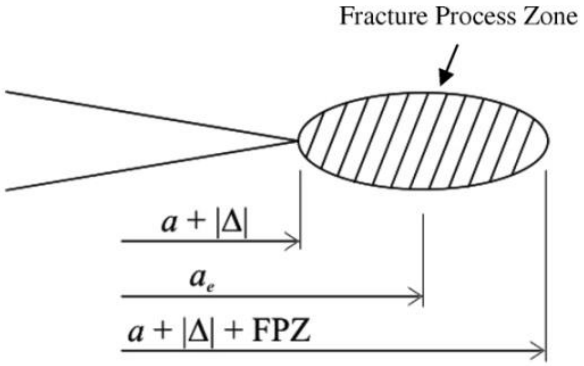

Figure 5.6 Schematic of fracture process zone (FPZ) and crack equivalent concept [131]

The (5.7) can be rewritten as (5.13). The coefficient α, β, and γ are given in (5.14). The equivalent crack length is now determined by the current compliance ($a_e = f(C)$) and can be calculated using (5.13) in Matlab® software. Considering the

real solution to solve this cubic equation the result is shown in (5.15) where the coefficient A is given in (5.16). This approach is known as the compliance-based beam method (CBBM) and allows for the determination of the fracture energy, G_{Ic}, directly from the $P-\delta$ curve. In this method there is no need to measure the actual crack length during testing by using an equivalent crack length derived from the compliance specified in (5.7). For more details, reference [131] can be consulted.

$$\alpha a_e^3 + \beta a_e + \gamma = 0 \tag{5.13}$$

$$\alpha = \frac{8}{bh^3 E_f}; \beta = \frac{12}{5bhG_{13}}; \gamma = -C \tag{5.14}$$

$$a_e = \frac{1}{6\alpha} A - \frac{2\beta}{A} \tag{5.15}$$

$$A = \left(\left(-108\gamma + 12\sqrt{3\left(\frac{4\beta^3 + 27\gamma^2\alpha}{\alpha}\right)} \right) \alpha^2 \right)^{\frac{1}{3}} \tag{5.16}$$

5.2.2. DCB results

The DCB load-displacement curves for both epoxy and polyurethane adhesives are presented in Figure 5.7a and b, respectively. These curves can show whether the crack has been propagated smoothly. Obviously, the polyurethane DCB presents a smoother load-displacement curve which means the crack has been propagated more smoothly for the polyurethane adhesives. Whilst in the DCB specimens with epoxy adhesive, the crack has been propagated in a different mode called stick-slip. In the stick-slip crack propagation mode, the crack does not propagate smoothly, in contrary, it is not propagating up to a certain load and it suddenly jumps ahead. This process keeps repeating until the complete propagation of the crack. These curves are also in accordance with the failure mode as in the case of polyurethane adhesive a complete cohesive failure is observed (Figure 5.3).

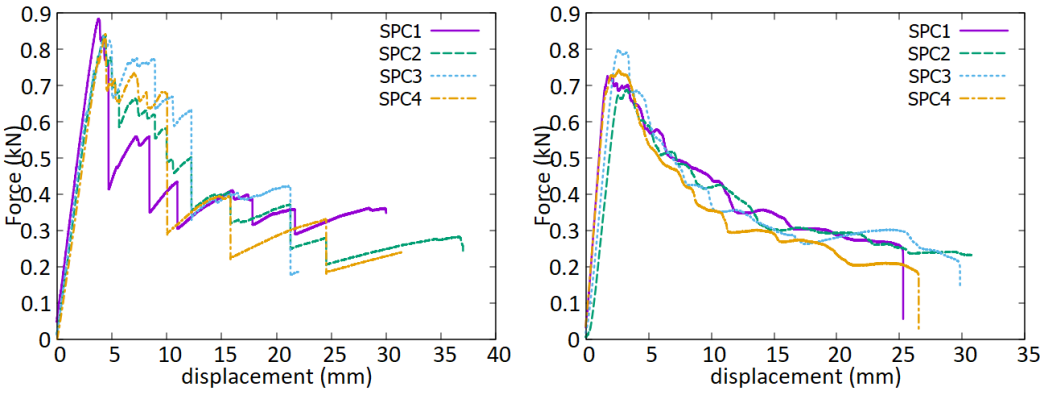

a) Epoxy adhesive b) Polyurethane adhesive

Figure 5.7 DCB specimen load-displacement curves

When the crack does not propagate in a smooth and continuous manner, accurately measuring its position throughout the test becomes highly complex and occasionally unfeasible [108]. Hence, in this study, due to the ability to calculate the energy release rate without direct measurement of the crack position, the CBBM reduction technique is employed to derive G_{IC} for the specimens bonded with epoxy adhesives. Both CBT and CBBM were used to acquire the G_{IC} for the specimens using polyurethane adhesives. Figure 5.8a and b present the R-curve (G Vs. a) for epoxy and polyurethane adhesives, respectively.

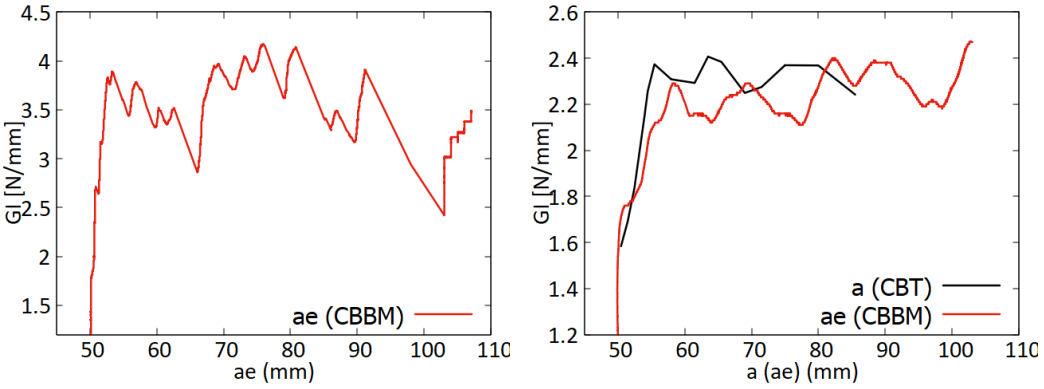

a) Epoxy b) Polyurethane

Figure 5.8 Adhesive mode I fracture energy: R-Curve (G_{IC} versus equivalent crack length).

5.3. End Notch Flexural (ENF) tests

After the ENF tests, the bonded surface of each specimen was checked and shown in Figure 5.9. It was observed that the failure surface is cohesive for both types of adhesives. All the tests were performed at a velocity of 5 mm/min. Moreover, the test condition and specimens' dimensions are detailed in section3.1.1.

a) epoxy

b) Polyurethane

Figure 5.9 ENF specimen failure surfaces

5.3.1. ENF data reduction schemes

Having the ENF test done, energy release rate in mode two can be obtained employing proper data reduction schemes. In classical data reduction methods, the critical SERR is usually calculated based on the Compliance Calibration Method (CCM) or beam theory as described in (5.1) [123]. According to this equation, the SERR in mode II is obtained (from Direct beam Theory (DBT)) in (5.17):

$$G_{IIC} = \frac{9P^2a^2}{16b^2E_1h^3} \tag{5.17}$$

As the simple beam theory does not consider the effect of transverse shear at the tip of the crack, Wang ang Williams [129] proposed a correction to the beam theory as follows (5.18):

$$G_{IIC} = \frac{9P^2(a+|\Delta_{II}|)^2}{16b^2E_1h^3} \quad (5.18)$$

Where Δ_{II} stands as the crack length correction taking into account the root rotation at the crack tip, and it is calculated in (5.19) as:

$$\Delta_{II} = 0.42\Delta_I \quad (5.19)$$

Δ_I is the correction factor for mode I, and it is outlined in (5.10).

The mentioned approaches depend on measuring the crack length throughout the test. Measuring the crack length is challenging due to the fact that crack's propagation happens by shear force while the adherends remain in contact. Therefore, it is hard to visualize and follow the crack propagation. Additionally, these methods do not consider the FPZ at the crack tip, a crucial area where damage occurs through plasticization and micro-straining, consuming a portion of the energy available. To address these issues, de Moura et al [132] proposed an alternative to previous approaches by considering an equivalent crack defined as $a_e=a+\Delta a_{FPZ}$. According to the beam theory, the specimen's compliance during the test can expressed in (5.20) as:

$$C = \frac{\delta}{P} = \frac{3a^3+2L^3}{8E_1bh^3} + \frac{3L}{10bhG_{13}} \quad (5.20)$$

Substituting a with a_e, and E_1 with E_f in (5.20) gives (5.21) as:

$$C = \frac{\delta}{P} = \frac{3(a+\Delta a_{FPZ})^3+2L^3}{8E_fbh^3} + \frac{3L}{10bhG_{13}} \quad (5.21)$$

The flexural modulus of the specimen can be obtained by inserting the initial compliance C_0 and the initial crack length a_0 in the (5.20). The outcome is (5.22) as follows:

$$E_f = \frac{3a_0^3+2L^3}{8bh^3C_{0corr}} \quad (5.22)$$

where C_{0corr} is give in (5.23):

$$C_{0corr} = C_0 - \frac{3L}{10bhG_{13}} \quad (5.23)$$

Now, the equivalent crack length is defined in (5.24) as:

$$a_e = a + \Delta a_{FPZ} = \left[\frac{C_{corr}}{C_{0corr}} a_0^3 + \frac{2}{3}\left(\frac{C_{corr}}{C_{0corr}} - 1\right) L^3\right]^{1/3} \tag{5.24}$$

Where C_{corr} is obtained from (5.23) by using C instead of C_0 which results in (5.25:

$$C_{corr} = C - \frac{3L}{10bhG_{13}} \tag{5.25}$$

Finally, SERR in mode II can be obtained by using a_e instead of a, and E_f instead of E_1 in (5.17). G_{II} is expressed in (5.26) as:

$$G_{II} = \frac{9P^2 a_e^2}{16b^2 E_f h^3} = \frac{9P^2}{16b^2 E_f h^3}\left[\frac{C_{corr}}{C_{0corr}} a_0^3 + \frac{2}{3}\left(\frac{C_{corr}}{C_{0corr}} - 1\right) L^3\right]^{1/3} \tag{5.26}$$

Following the described approach, the critical fracture energy, denoted as G_{IIC}, is determined directly from the P–δ curve. It is important to note that the modulus of the specimen is not manually inputted but rather calculated (see (5.22)). This calculation depends on the initial compliance and G_{13}. The only material property required for this method is G_{13}. Research by de Moura et al. [131] indicates that G_{13} has a significantly lower impact compared to the longitudinal modulus, suggesting that a typical value can be effectively utilized in this context.

5.3.2. ENF results

The ENF load-displacement curves for both epoxy and polyurethane adhesives are presented, respectively, in Figure 5.10a and b, respectively. In the ENF test, both substrates are in close contact with each other and during the test they will come even closer. This makes it difficult to observe the crack and its actual position. Therefore, the CBBM method is also used to obtain the G_{IIC} for both types of adhesives. The R-curve is shown in Figure 5.11a and b, respectively, for epoxy and polyurethane adhesive. As it can be seen in Figure 5.11b, the R curve is not reaching a plateau. Instead, G_{II} is reducing linearly after the peak value. this might be originated from some sources of errors. During the tests it was observed that before the polyurethane adhesive undergoes the complete shear load the crack propagated both within the adhesive and the composite substrates as shown in Figure 5.12. As a result, this interlaminar failure poses error to the adhesive characterization properties. To address this problem, another approach using FEM and SLJ experimental test is proposed and explained in chapter 7. It should be mentioned

that, in general, if the crack is propagating both in the adhesive and in the adherend, simultaneously G_{IIC} would be for sure overestimated. However, if the composite interlaminar G_{II} is much lower than the adhesive's and the crack migrates to the adherend then propagate exclusively within the substrate, G_{IIC} could actually be underestimated. Following the cracks was not easy in the specimens. According to my observations it seems that the crack, at first, started propagating in the adhesive and then propagated simultaneously both in the adhesive and the substrate. Therefore, the first probable idea is that the G_{II} value is overestimated.

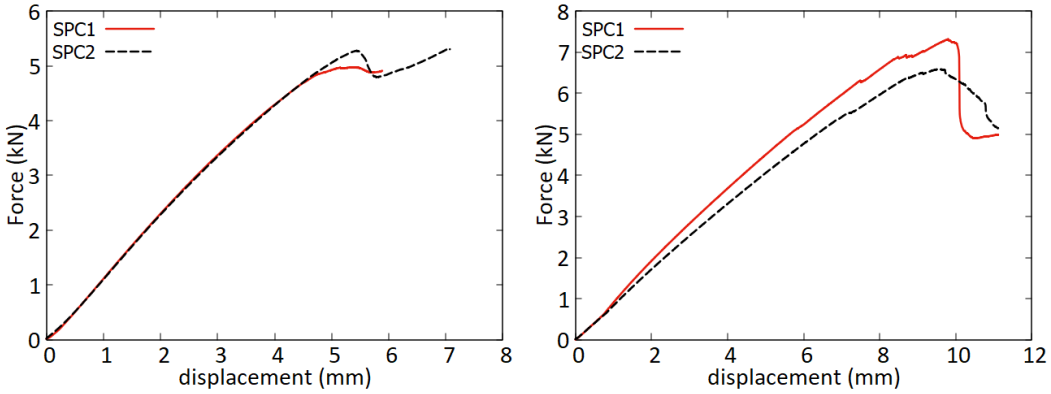

a) Epoxy b) Polyurethane

Figure 5.10 ENF specimen load-displacement curves

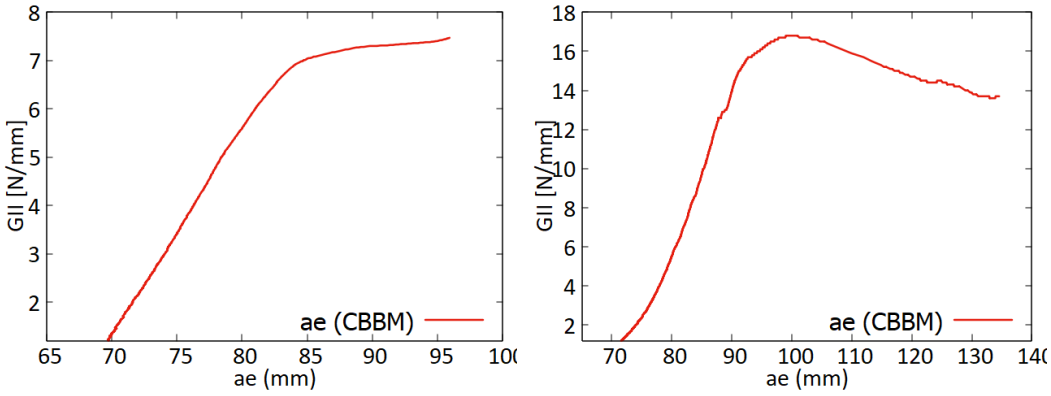

a) Epoxy b) Polyurethane

Figure 5.11 Adhesive mode II fracture energy: R-Curve (G_{IIC} versus equivalent crack length).

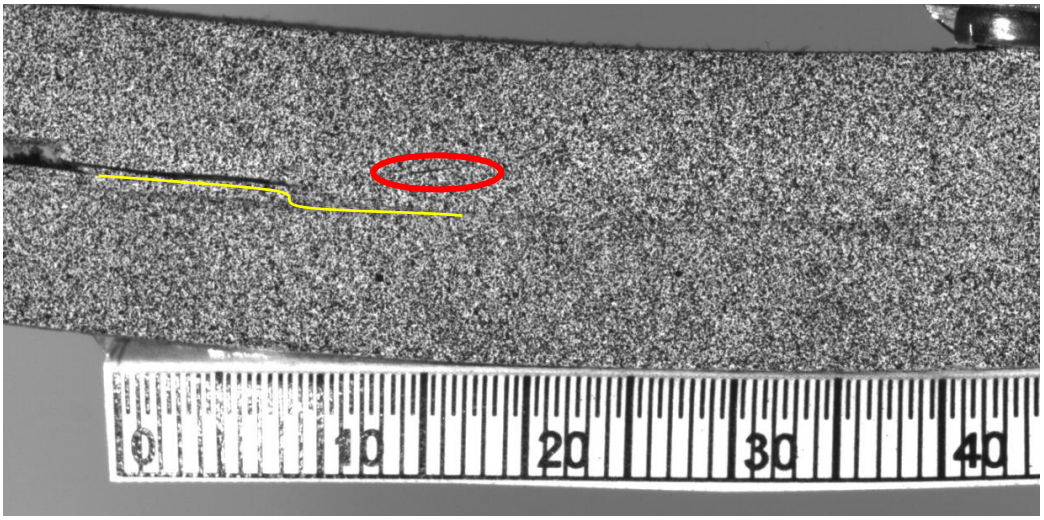

Figure 5.12 Substrate interlaminar crack propagation in ENF test with polyurethane adhesive.

5.4. Conclusion of Task 1

This research activity was performed to characterize two different types of adhesives, a rigid epoxy and a relatively soft polyurethane. For this purpose, different types of tests were performed including tensile test on the adhesive bulk Dogbone, DCB, and ENF test. The obtained results are as follows.

- Young modulus, ultimate strength and elongation were obtained from the adhesive bulk dogebone specimen tests. In case of epoxy adhesive, these properties are, 2500 MPa, 35 MPa, and 4.1 %, respectively. In the case of polyurethane adhesive, these values are, respectively, 278 MPa, 13 MPa, and 22 %.
- To find the adhesive critical energy release rate in mode I (G_{IC}) DCB test was performed. It was found out that the crack propagated more smoothly in specimens with polyurethane adhesives with respect to the epoxy specimen in which the crack propagated with the stick-slip mechanism.
- Corrected Beam Theory (CBT) and Compliance Based Beam Method (CBBM) were used as the data reduction schemes. The G_{IC} value obtained for epoxy and polyurethane adhesives are 3.75 N/mm and 2.3 N/mm, respectively.
- To find the adhesive critical energy release rate in mode II (G_{IIC}) ENF test was performed. CBBM was used as the data reduction scheme. The G_{IIC} value obtained for epoxy and polyurethane adhesives are 7.2 N/mm and 12-17 N/mm, respectively. However, because of the crack propagation in both

adhesive and substrate in specimen with polyurethane adhesive its G_{IIC} value is overestimated and is not precise and highly likely is overestimated.

Chapter 6

6. Effect of joint dimension on the behavior of composite SLJs[1] (Task 2)

In this task, the behavior of composite SLJs subjected to quasi static loading (5mm/s) are studied when the joint dimension (Overlap length (L), Joint width (W), and substrate thickness (T) are changed. In the case of polyurethane SLJs all considered substrate thickness (T1, T2, T3) are discussed. On the other hand, in case of SLJs with epoxy adhesives only the results related to T2 and T3 are reported. In case of epoxy adhesive and SLJs with substrate T1, the obtained max forces were different from specimen to specimen and the failure was adhesive for all cases. Therefore, the result for this thickness is not reported. For this task, the SLJ specimen manufacturing was already well-explained in section 3.2. The tests were performed at a velocity of 5mm/min using Instron machine. In the following sections the results and discussion are provided. One point to be considered is that all the stresses are mentioned here are limit stresses, i.e. corresponding to failure conditions.

[1] **The content of this task is already published as papers [10–13]. Minor changes have been made on grammar, formatting, and the synchronization of the list of references in order to integrate the papers within the dissertation.**

6.1. Polyurethane adhesive SLJs

Three samples of each configuration mentioned in Table 3.2. were tested and the results are shown in Figure 6.1. Each configuration presents good repeatability. In general, Figure 6.1 shows that by increasing the thickness of the substrates the displacement at maximum load does not change significantly. Whereas, increasing the overlap length leads to a slight rise of the displacement at maximum load. Further, the width does not significantly influence the ultimate displacement by considering L1 overlap for the three different adopted thicknesses. A slight difference can be observed by considering the L2 overlap effect on the ultimate displacement. In particular, the displacement increases for SLJ prepared with a larger width.

The summary of the results and the effect of L, W, and T, on the mechanical behavior of SLJ are reported in Figure 6.2. Peak force and joint stiffnesses (the slope of the initial linear part of the load-displacement curve) are reported. The values in the diagrams show that all three parameters significantly influence the peak force and joint stiffness. The larger the bonding area the higher the peak force and the joint stiffness. At a fixed substrate thickness, in joints with the same bonding area (L1W2T1 and L2W1T1, L1W2T2 and L2W1T2, L1W2T3 and L2W1T3), the behaviors are almost similar except that the stiffness for the joints with larger width is slightly greater. This is because with a larger width more of the bonded area is close to the overlap ends and therefore is more involved in the joint response, as in lap joints the middle zone of the overlap is less loaded. The minimum peak force and stiffness belong to L1W1T1 while the maximum ones belong to L2W3T3. The analysis of data in Figure 6.1 and Figure 6.2 shows that L and W are approximately equally and more influential than T on the load capacity of the joints. However, the effect of W on joint stiffness is greater than the effects of L and T.

To get into more details, for example in specimens with substrate thickness T1 (Figure 6.1a and Figure 6.2a), by increasing the joint width the peak force increased by 115% and 238%, respectively, for L1W2T1 and L1W3T1 compared to L1W1T1. These increases are 95 and 225%, respectively, for L2W2T1 and L2W3T1 compared to L2W1T1. Now, keeping both joint width and substrate thickness fixed, comparing L2W1T1 to L1W1T1, L2W2T1 to L1W2T1 and L2W3T1 to L2W3T1 the peak force increased by 130, 108, and 121 %, respectively. Finally, comparing L1W2T2 and L1W2T3 to L1W2T1 the peak force increased by 50% and 90 % respectively, while comparing L2W2T2 and L2W2T3 to L2W2T1 the peak force increased by 47 and 70 % (Figure 6.1a,b,c and Figure 6.2a,b,c).

The same comparison for joint stiffness is done. The results (Figure 6.1a and Figure 6.2a) show that by increasing the joint width the stiffness increased by 96.2% and 203.2%, respectively, for L1W2T1 and L1W3T1 compared to L1W1T1. These increases are 91.3 and 207.4%, respectively, for L2W2T1 and L2W3T1 compared to L2W1T1. Now, keeping both joint width and substrate thickness fixed, comparing L2W1T1 to L1W1T1, L2W2T1 to L1W2T1 and L2W3T1 to L1W3T1 the stiffness increased by 45, 41.4, and 47 %, respectively. Finally, comparing L1W2T2 and L1W2T3 to L1W2T1 the peak force increased by 45% and 128 % respectively, while comparing L2W2T2 and L2W2T3 to L2W2T1 the stiffness increased by 70 and 130 % (Figure 6.1a,b,c and Figure 6.2a,b,c).

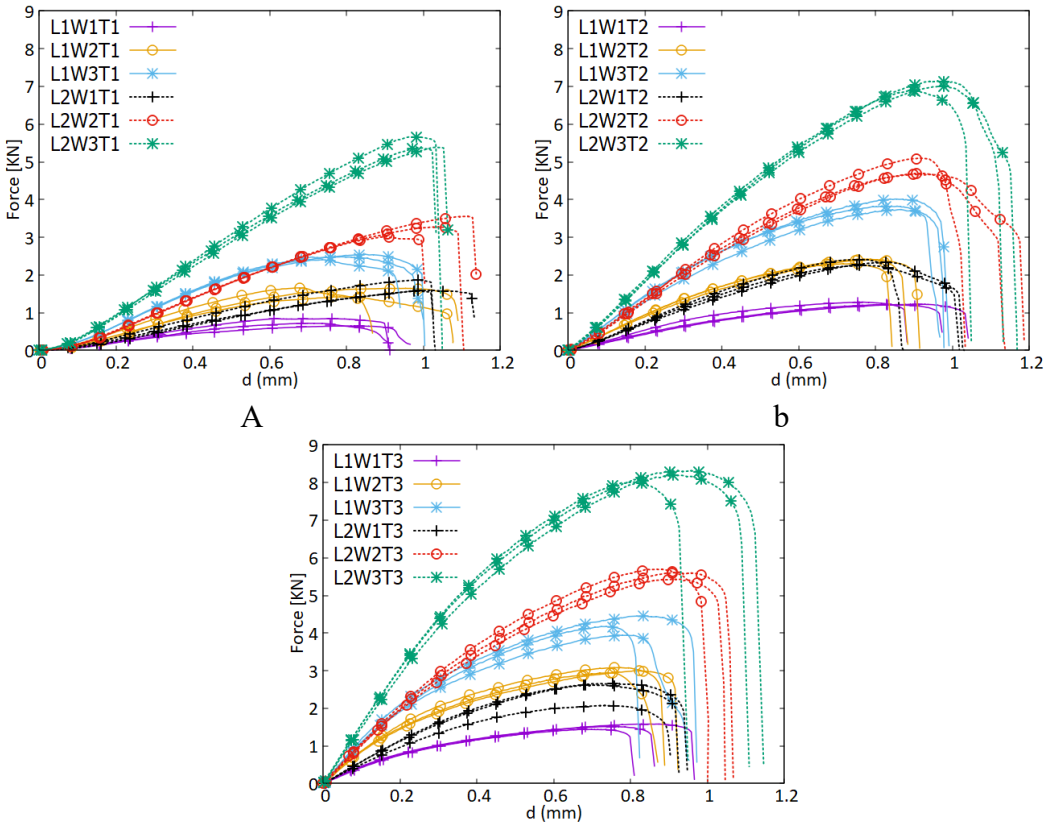

Figure 6.1. Load-displacement curves all the specimens including their repetitions a) substrate with T1 b) substrate with T2 c) substrate with T3

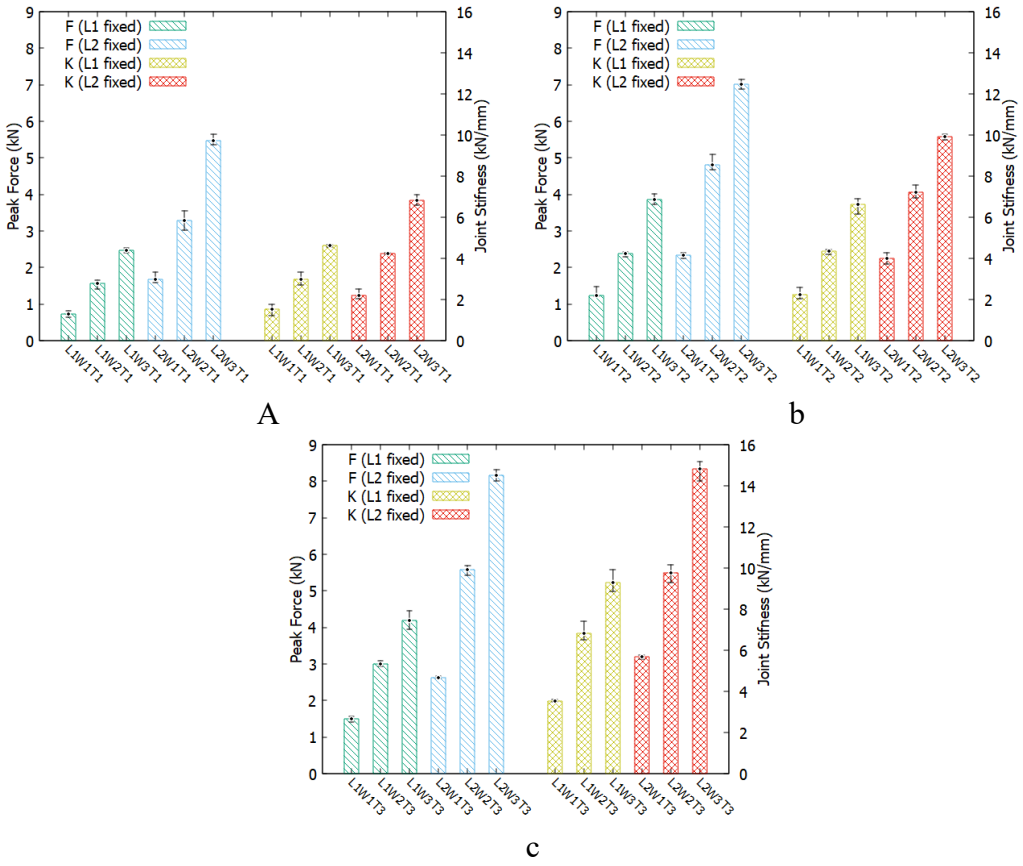

Figure 6.2. Peak force (F) and joint stiffness (K) for all the specimens a) substrate with T1 b) substrate with T2 c) substrate with T3

Figure 6.3a,b,c shows that, by changing the width of the bonding area, the average shear stress (Force/bonded area) at failure computed in the joint tends to remain approximately constant for every overlap length. On the other hand, keeping the substrate thickness fixed, by increasing the overlap length from L1 to L2 there is a slight decrease of shear stress, 5.2% and 10% in T2 and T3 respectively, except for T1 which remains almost constant by considering also the reported error bars. Since the width does not change the shear stress significantly and the change caused by the overlap length is less than 10% in all the specimens, for every substrate thickness an average value of shear stress is considered. Based on these average values, comparing T2 and T3 to T1, increasing the substrate thickness resulted in an increase of 46% and 72% in shear stress. This is because the stress distribution becomes more uniform as the substrate thickness increases, reducing the stress peaks at the overlap ends.

Figure 6.3a,b,c also shows that by changing the width of the bonding area, the normal stress (Force/substrate cross-sectional area) computed in the substrate tends to remain approximately constant for every overlap length. Whilst, keeping the thickness of the substrates constant, increasing the overlap length from L1 to L2 increases the substrate normal stress by 120%, 90% and 83%, respectively, for T1, T2, and T3. Moreover, at the same width and overlap length, substrates with smaller thickness undergo larger normal stress. The normal stress reduced 20% and 52%, respectively, for L1W(1,2,3)T2 and L1W(1,2,3)T3 comparing to L1W(1,2,3)T1. Similarly, by comparing L2W(1,2,3)T1 to L2W(1,2,3)T2 and L2W(1,2,3)T3, the normal stress is reduced by 30% and 60% , respectively.

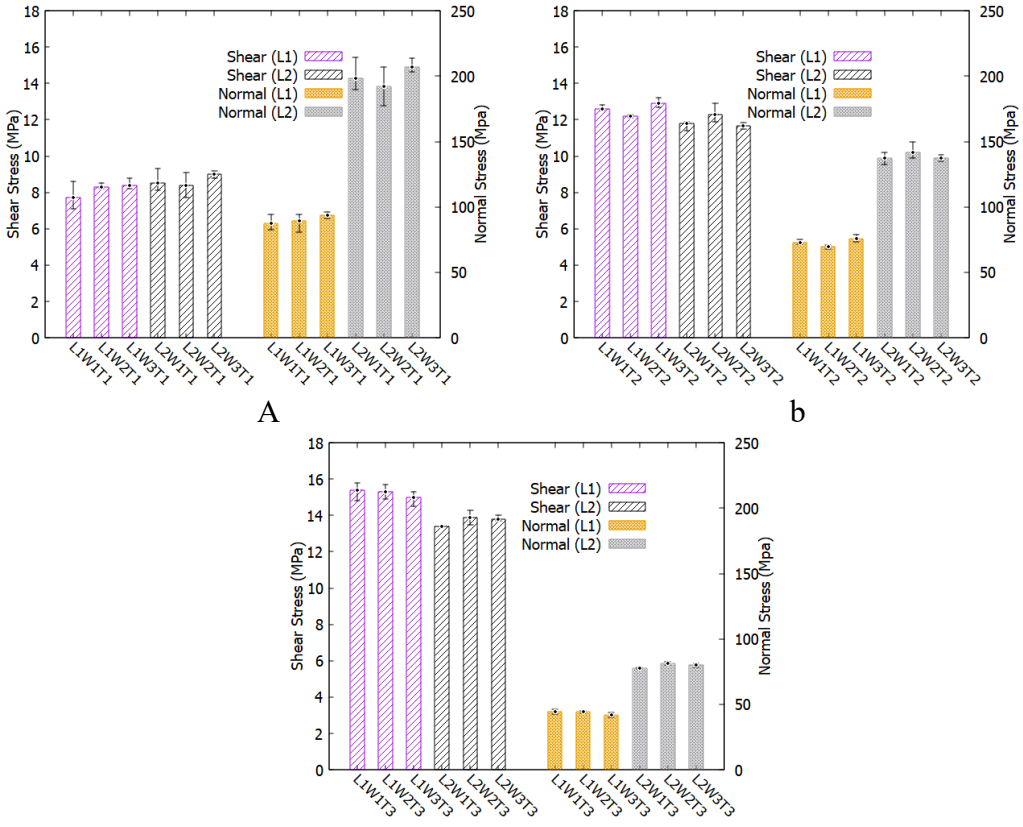

Figure 6.3. Adhesive shear strength and substrates normal stresses for all the specimens a) substrate with T1 b) substrate with T2 c) substrate with T3

6.2. Polyurethane SLJs failure surfaces

After the test, specimens were carefully checked and different types of damages including adhesive, cohesive, thin layer cohesive and mixed mode were observed as shown in Figure 6.4. It was observed that as a general behavior when the thickness of the substrates increases, the failure tends to be more cohesive. This ca be ascribed to the fact that when the thickness of the substrate increases its stiffness will increase in a way that the adhesive experiences, in relative terms, more shear and less peel stress. Moreover, the middle of the joints is under compression, because locally the peel stress is negative, and this compression is greater in joints with thicker substrates. This result is discussed in more detail in section7.2.1.

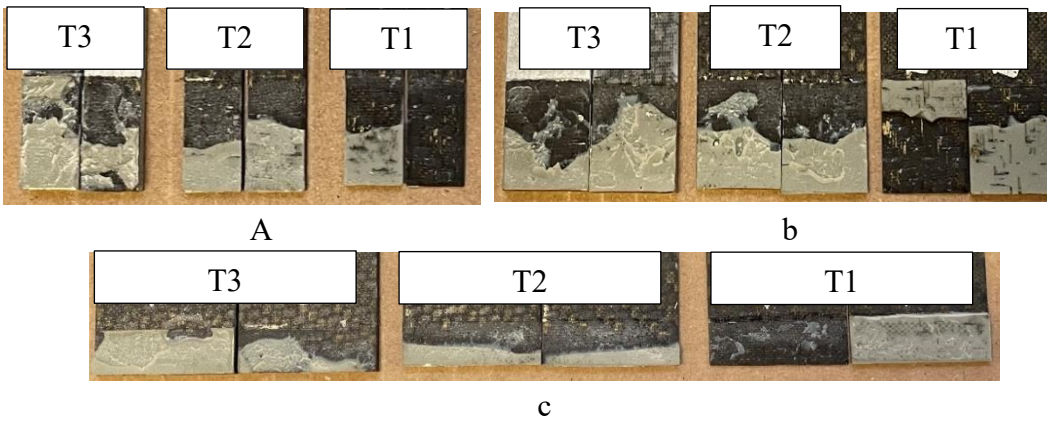

Figure 6.4. Failure surfaces of the specimens after the test a) L2W1T1,2,3 b) L2W2T1,2,3 c) L1W3T1,2,3

6.3. Epoxy adhesive SLJs

As mentioned at the beginning of this task, only the results related to T2 and T3 are reported here for epoxy SLJs.

In general, Figure 6.5 a and b illustrate that by increasing the thickness of the substrates and joint width the displacement at maximum load is not changing significantly. Whereas, increasing the overlap length led to a rise of 15 % and 10% in the displacement at maximum load for specimens T2 and T3, respectively.

Based on the results shown in Figure 6.6 a and b, similarly to polyurethane SLJs, all three parameters (L, W, and T) are significantly influential on the peak force of epoxy joints. the more the bonding area the more the peak force. The joint

width and substrate thickness are more influential for joint stiffness. Contrarily, the overlap length has a negligible effect on joint stiffness. At a fixed substrate thickness, in joints with the same bonding area (L1W2T2 and L2W1T2, L1W2T3 and L2W1T3), the peak load and stiffness are larger for the joints with larger widths. Similarly to polyurethane joints, L1W1T2 presents the minimum peak force and stiffness while the maximum values are experienced with the joint configuration L2W3T3. Figure 6.5 a and b and Figure 6.6 a and b show that L and W influence the load capacity more than T. However, the effect of W on joint stiffness is greater than the effects of L and T.

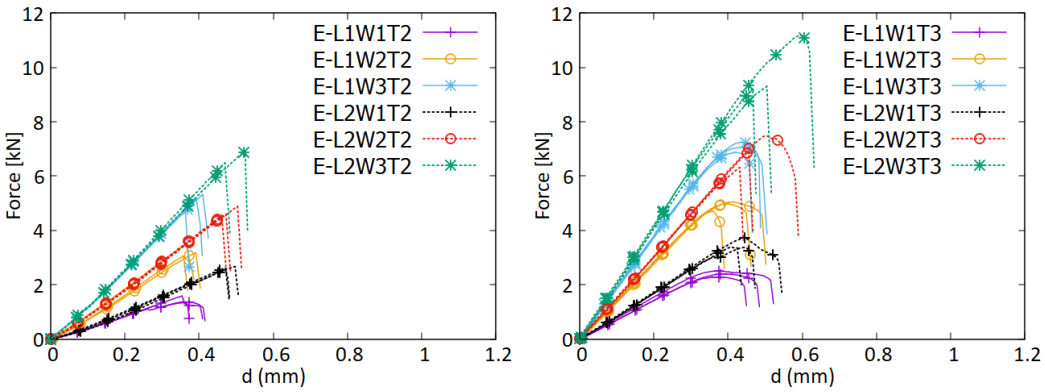

A b

Figure 6.5. Load-displacement curves of Epoxy SLJs including their repetitions: (a) T2; (b) T3

In particular, in the specimens with the substrate thickness T3, the peak force increased by 105% and 195%, respectively, for L1W2T3 and L1W3T3 compared to L1W1T3. The increases are 89% and 183%, respectively, for L2W2T3 and L2W3T3 in the case of comparing to L2W1T3. On the other hand, by fixing both joint width and substrate thickness the peak force increased by 46, 35, and 40% comparing L2W1T3 to L1W1T3, L2W2T3 to L1W2T3 and L2W3T3 to L2W3T3 respectively. Finally, comparing L1W2T3 to L1W2T2 the peak force increase is 51%, while comparing L2W2T3 to L2W2T2 the peak force increased by 36%.

The same comparison for joint stiffness is done. The results show that by increasing the joint width the stiffness increased by 92% and 156%, respectively, for L1W2T3 and L1W3T3 compared to L1W1T3. The increases are 77 and 141%, respectively, for L2W2T3 and L2W3T3 in the case of comparing to L2W1T3. Now, considering both joint width and substrate thickness fixed, comparing L2W1T3 to L1W1T3, L2W2T3 to L1W2T3 and L2W3T3 to L2W3T3 the stiffness increased

16, 7, and 9%, respectively. Finally, comparing L1W2T3 to L1W2T2 the stiffness increased 67%, respectively, while comparing L2W2T3 to L2W2T2 the stiffness increased 66. The results are summarized in Table 6.1 based on the average values.

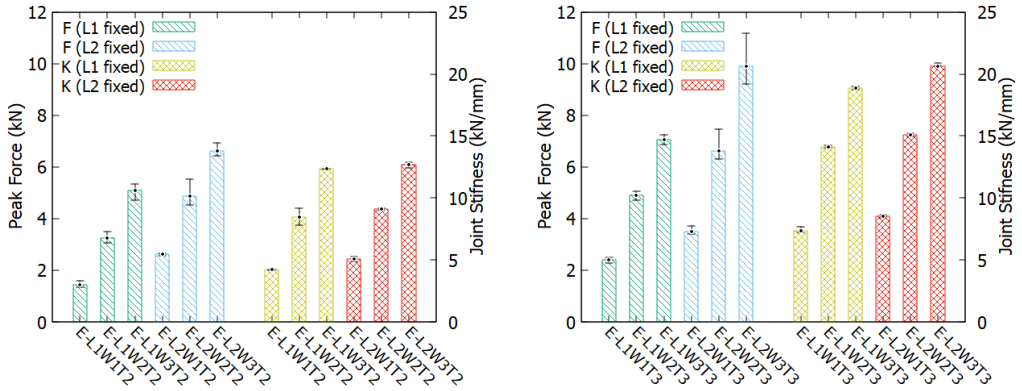

Figure 6.6. Peak force (F) and joint stiffness (K) of Epoxy SLJs: (a) T2; b) T3

Figure 6.7 a, and b show the average values of the shear stresses and normal stresses for all the investigated configurations. The shear stress is the force to bonding area ratio while the normal stress is the force to cross-sectional area of the substrate thickness ratio. These values have been investigated to understand whether there is an influence of substrate size on the mechanical response of the joints. Figure 6.7 a, and b illustrate that, by changing the width of the joint, shear stress (force/bonding area) tends to remain approximately constant for every overlap length. Therefore, the percentages will be based on the average values related to all three widths. At fixed substrate thickness, by increasing the overlap length from L1 to L2 there is a decrease in shear stress. For substrate with thickness T2, this reduction is 26% for epoxy joints. Whilst, for substrates with thickness T3, the reduction is 28% for epoxy joints. This is a consequence of the increase in peel and shear stresses at the edges of the joint that is larger when the overlap length is increased. Furthermore, increasing the substrate thickness increases the shear stress. To illustrate statistically, increasing the substrate thickness from T2 to T3 resulted in an increase of 45% and 41%, respectively for L1 and L2, in shear stress. When the thickness of the composite substrate increases its stiffness increases as well. Therefore, it will be less susceptible to being bent and the joint experiences a higher shear stress with respect to peel stress. T is the most influencing parameter, then L is also influencing while W has negligible effects on shear stress.

Figure 6.7 shows that like shear stress the normal stress in the substrate (force/substrate cross-sectional area) also remains approximately constant for every overlap length by changing the joint width. When the width increases the cross-sectional area of the substrate also changes. Having approximately constant normal stress in joints with different widths means that the load capacity of the joints changes approximately at the same rate as width changes. Therefore, the ratio of force over the cross-sectional area remains unchanged. Contrary to shear stress, by increasing the overlap length the normal stress increases. At fixed substrate thickness, increasing the overlap length from L1 to L2 increases the normal stress by 59%, and 43%, respectively, for T2 and T3. In this case, by increasing the joint length only the bonding area increases which results in increasing the load capacity, while the cross-sectional area is the same. Thus, the normal stress increases. Again, in contrast with shear stress, at the same width and overlap length, substrates with smaller thickness undergo larger normal stress. By increasing the substrate thickness from T2 to T3, the normal stress is reduced by 26% and 34%, respectively, for L1 and L2. Based on the results, L is the most influential parameter, T is an influential parameter, and W is not an influential parameter on normal stress in the substrates of a composite SLJ. Table 6.1 shows a summary of the effect of all parameters on the mechanical behavior of the joints based on the average values.

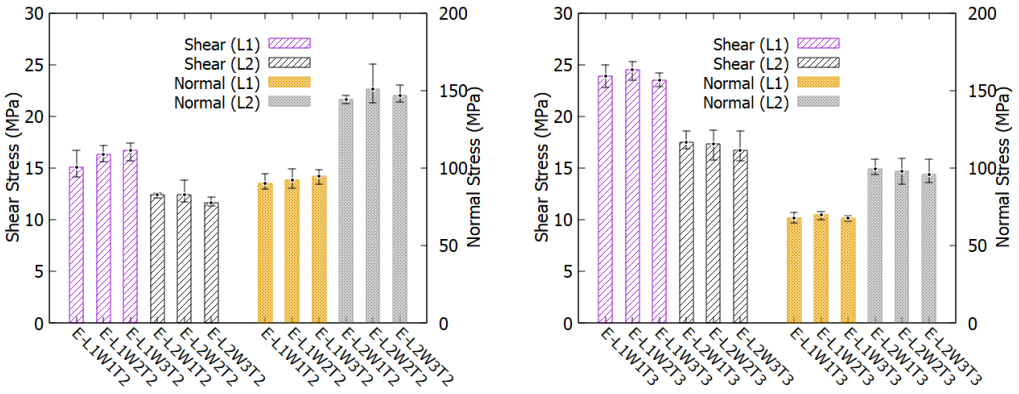

Figure 6.7. Adhesive shear strength and substrates normal stresses for all the specimens: (a) Polyurethane T1; (b) Polyurethane T2; (c) Epoxy T2; (d) Epoxy T3

Table 6.1. The average effect of each parameter on the mechanical properties of SLJ joints

Adhesive Type	Studied Parameters	Parameters Increased by from T2 to T3 (%)	Peak Force (%)	Joint Stiffness (%)	Shear strength at failure (%)	Normal Stress in Substrates (%)
Polyurethane	L	100	88.4±9.5	59.4±12.5	-7±0.04	105.7±0.2
	W	100	101.5±5.6	84.3±9.2	±1.5±0.1	±3±0.2
	T	100	16.9±6.2	47.2±9.6	17.5±0.05	-24.8±0.08
Epoxy	L	100	47.7±18.3	10.4±6.3	-27.4±1.3	51.2±11.5
	W	100	100±19.8	83.7±10.9	±2±0.1	±1±0.01
	T	100	46±12.6	65.7±7.4	43.7±2.7	-29.8±5

6.4. Epoxy SLJs failure surfaces

The failure surfaces have been visually inspected after the tests and different types of damages including adhesive, cohesive, thin layer cohesive and mixed mode have been observed (Figure 6.8). Moreover, it was observed that, as a general behavior, when the thickness of the substrates increases the failure tends to show more cohesive behavior, although a thin layer of adhesive is always present on one of the substrates. This might be due to the thickness of the substrate which increases its stiffness in a way that the adhesive experiences more shear with respect to peel stress.

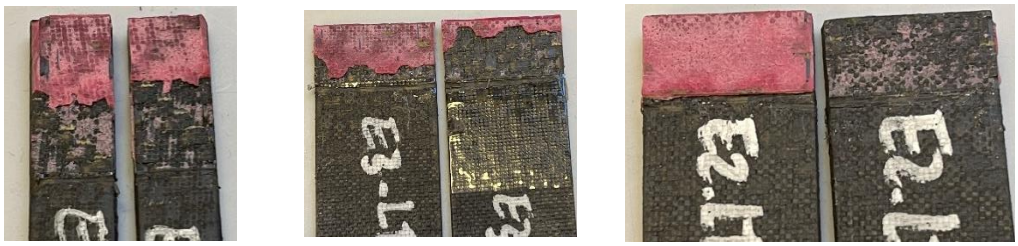

E-L2W1T3 E-L1W2T2 E-L1W3T3

Figure 6.8. Failure surfaces of the specimens after the test

6.5. Comparison between epoxy and polyurethane

By analyzing the average shear stress values, it was understood that the behavior of epoxy adhesive joints is more influenced by the joint dimensions, i.e., increasing the overlap length and substrate thickness results in larger changes in average shear stress for epoxy adhesive joints compared to the Polyurethane adhesive joints. This could be due to the larger young modulus and the stiffness of the epoxy adhesive in comparison with the polyurethane adhesive.

To summarize the effect of each parameter on the response of composite SLJs, the main effect plot for all the considered parameters is given in Figure 6.9 and Figure 6.10, respectively, for polyurethane and epoxy adhesives.

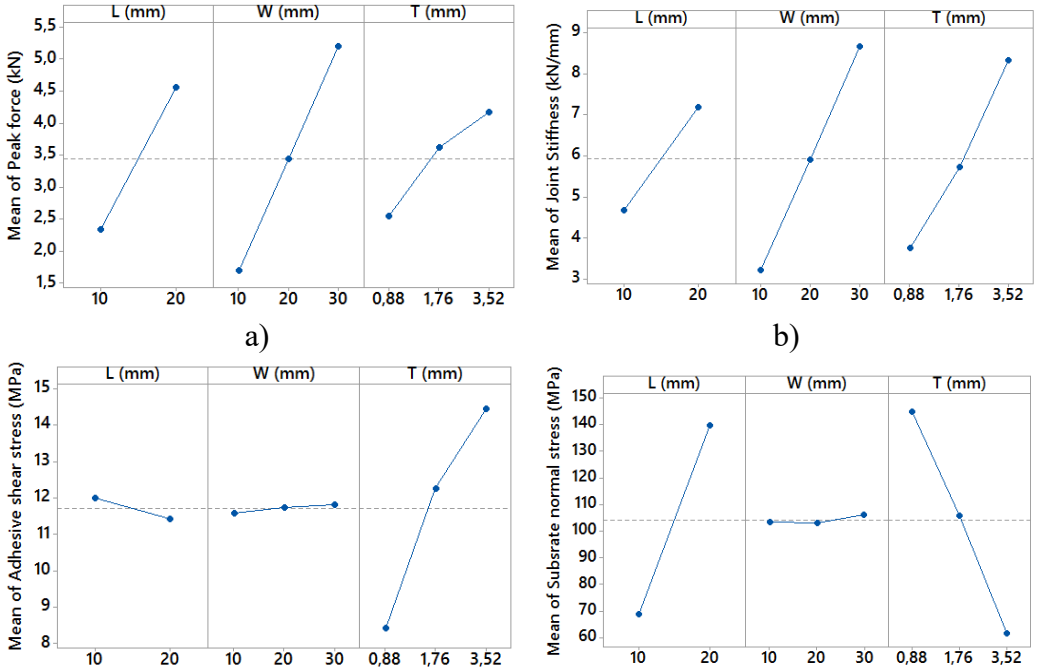

Figure 6.9 Main effect plot of parameters L, W, and T in polyurethane SLJs; a) Peak force b) Joint stiffness c) Adhesive shear stress d) Substrate normal stress

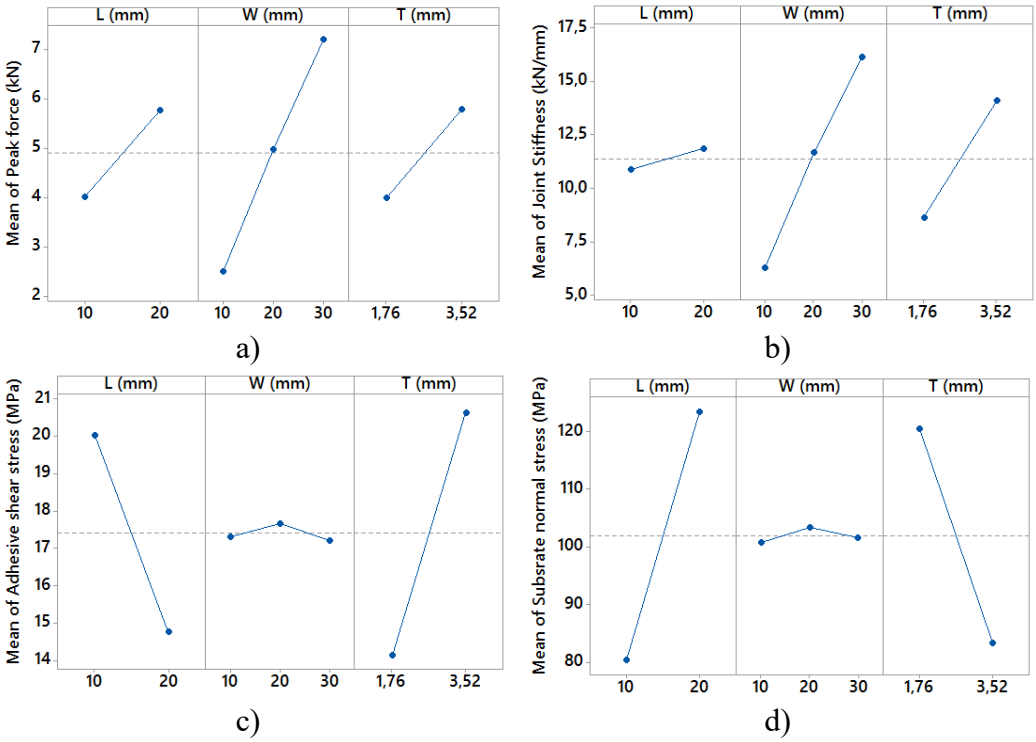

Figure 6.10 Main effect plot of parameters L, W, and T in epoxy SLJs; a) Peak force b) Joint stiffness c) Adhesive shear stress d) Substrate normal stress

6.6. Conclusion of Task 2

This task aims to observe the effect of different joint geometry parameters (adherend thickness, joint width, overlap length) on the mechanical behavior of composite SLJs, with both epoxy and polyurethanes adhesives, subjected to tensile load. The following conclusions were drawn:

- Polyurethane SLJ demonstrated an elastic-plastic behavior before the rupture, while epoxy SLJs showed an approximately linear elastic behavior up to the point of rupture.
- The peak load and joint stiffness in epoxy SLJs were larger (on average, 18 and 40%, respectively) than in the same joint with polyurethane adhesive. However, the displacement at maximum load in polyurethane SLJs was approximately 100% greater in comparison with the same epoxy SLJs.
- In polyurethane SLJs, an increase in all three geometric parameters (T, W, L) increases both joint stiffness and peak load. The joint width and length showed a more significant impact.

- L, W, and T are more significantly influential on the peak force in epoxy SLJs. W is more influential than L and L is more influential than T on the load capacity of the joints. On the other hand, W and T are of greater importance for joint stiffness. However, the overlap length has a negligible effect on joint stiffness. Moreover, at each substrate thickness, joints with the same W showed approximately equal stiffness.
- According to the results, T is the most effective (positive) parameter, followed by L (which is (negatively) affective), and W has negligible effects on shear stress. The shear stress of epoxy SLJs is more prone to change by changing the joint dimensions in comparison with polyurethane SLJs.
- L is the most influential parameter, T is an influential parameter, and W is not an influential parameter on normal stress in the substrates of a composite SLJ.
- Keeping the thickness of the substrates constant, an increase in overlap length resulted in a reduction in shear stress and an increase in normal stress. In addition, for all the geometrical configurations, increasing the adherend thickness increases the shear stress and decreases the normal stress.

Chapter 7

7. Fracture properties estimation of polyurethane adhesive[1] (Task 3)

The purpose of this task is to find an alternative to delicate tests like ENF in order to characterize the fracture of adhesives. Therefore, a finite element model of a SLJ is prepared. Experimentally, the response of SLJs is already obtained and discussed in Task 2 (chapter 60). The proposed methodology involves simulating the SLJs and correlating the results to their experimental response by iteratively updating the adhesive properties. Once the experimental and numerical results agree, the adhesive properties are obtained.

As mentioned previously in section 4.1, understanding the mechanical properties of an adhesive such as G_{Ic}, G_{IIc}, maximum traction (t), and shear (s) stresses is crucial for conducting a successful finite element analysis of an adhesive joint using the CZM method. Reis et al. [70] demonstrated that in a single lap joint with stiffer substrates, a higher shear stress is observed, indicating that the joint is primarily influenced by mode II. Therefore, the SLJ with the greatest substrate thickness (T3) was chosen as the benchmark experimental test for conducting ANOVA and optimization. In this scenario, the impact of mode I on joint failure is diminished, and the most critical parameters are expected to be G_{IIC} and s. An

[1] **The content of this task is already published as papers [10–13]. Minor changes have been made on grammar, formatting, and the synchronization of the list of references in order to integrate the papers within the dissertation.**

ANOVA was conducted based on these parameters using LS-Opt to validate this assertion.

7.1. Sensitivity analysis and Optimization result

The results of ANOVA and sensitivity analysis for a relatively thick substrate (T3) are given in Figure 7.1. This figure demonstrates that the effect of G_{IC} and t on the load-displacement curve of the joint can be neglected while the parameters G_{IIC} and s affect the results considerably. Therefore, the L2W2T3 specimen was chosen to perform the optimization and to find the optimum value for G_{IIC}, s, and d_1.

To minimize the difference between the experimental and numerical load-displacement curves to an acceptable value, the optimization was run in 4 iterations. After each iteration, the amount of MSE is reduced and the output curve was closer to the experimental target curve. Finally, in the 4^{th} iteration, an acceptable load-displacement curve was found which presents a good correlation with the experimental results. Figure 7.2 shows the design sample over all the iterations and the final optimum values of the interested parameters. The optimum values for the parameters G_{IIC}, s, and d_1 are obtained as 10 N/mm, 14.3 MPa, and 0.275 respectively. Afterward, the simulation was repeated for other samples, a couple of which are shown in Figure 7.3. As can be seen, there is a good, or at least satisfactory, agreement between load-displacement curves from FEM and the tests. The initial linear behavior, maximum load and failure are well predicted by the FEM model. It should be noted that for specimens with smaller substrates thickness, the values could be changed. This might be because of the changes in failure mode as shown in Figure 6.4. The thicker the substrates the more the cohesive failure and as a result the adhesive approaches its real limits and behavior. Furthermore, the effects of mode I increase in specimens with thinner substrates as they are more flexible and prone to be bent easier.

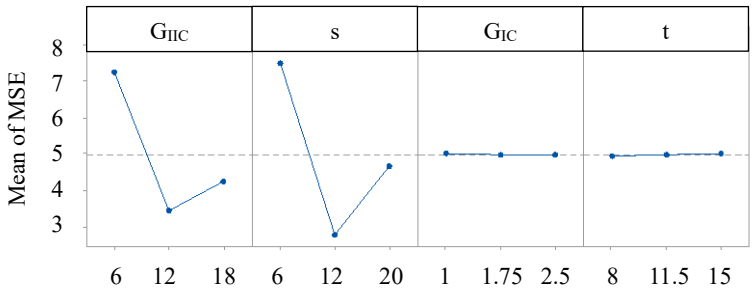

Figure 7.1. The effect of parameters G_{IIC}, s, G_{IC}, and t on the Mean Squared Error between load-displacement curve of model & experiments

Based on the assumption that was made according to references [118,119], the amount of G_{IC} should be around 2.5 N/mm. To validate the obtained result, the DCB test which is discussed in section 5.2.2 was also performed. Figure 7.4 shows the G_{IC} versus crack length during the test. As expected, G_{IC} is equal to 2.3 N/mm which is consistent with the assumption. Now, considering the results and discussion of section 5.3.2, it is obvious that the value of G_{IIC} from ENF test is overestimated (12-17 N/mm) because of the substrate interlaminar crack propagation.

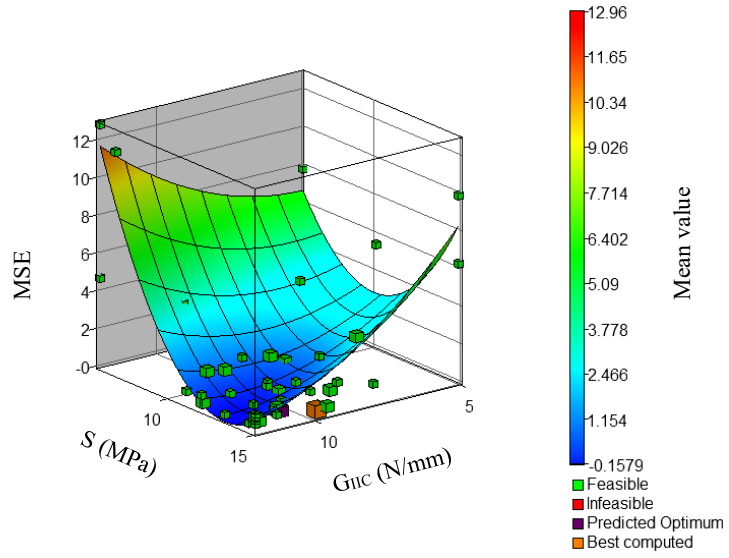

a

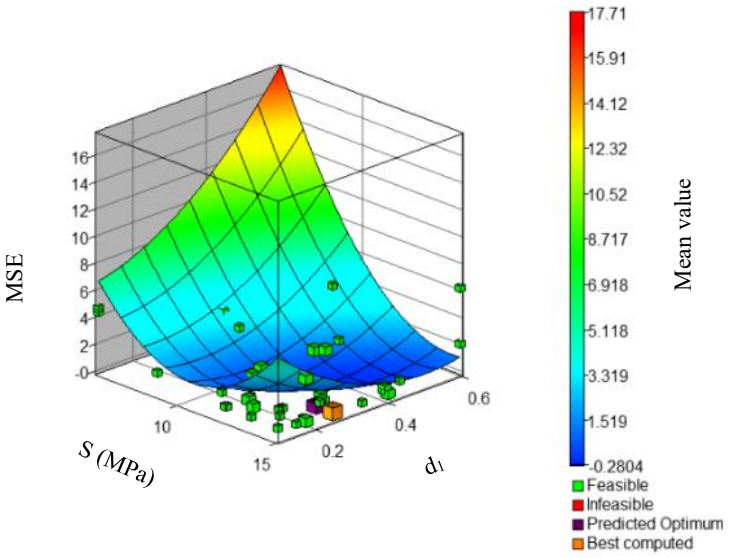

b

Figure 7.2. Metamodel design points and the optimum values considering MSE approach a) s-G_{IIC} b) s-d_1

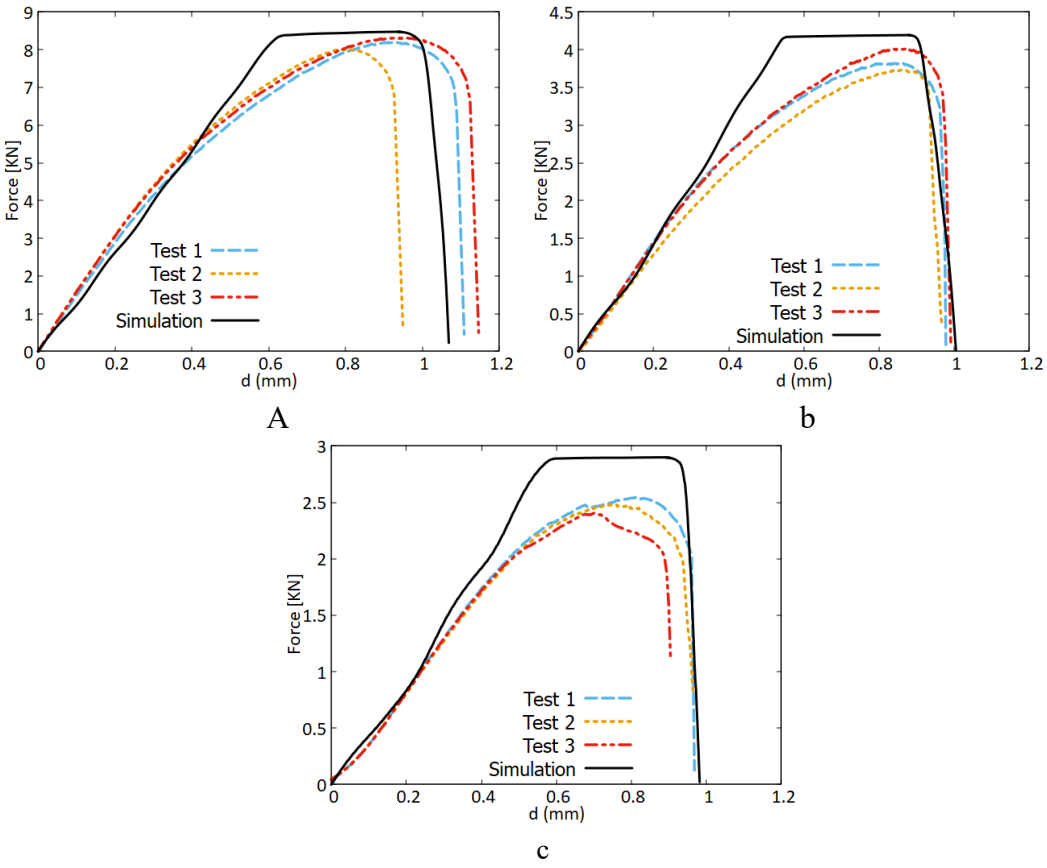

Figure 7.3 Comparison between the experimental and numerical results a) L2W3T3, b) L1W3T2, c) L1W1T1

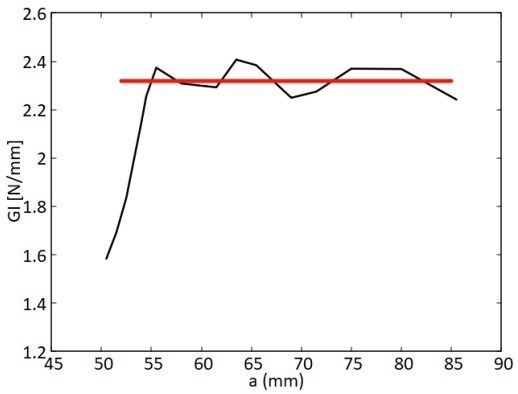

Figure 7.4. Adhesive R-Curve (G_{IC} versus crack length).

It seems that the trapezoidal cohesive law could have been limiting the correlation between the model and the experimental results for this specific set of

geometric parameters (the trapezoidal shape of the cohesive law is clearly visible in the simulated curves of Figure 7.3). Certainly, adopting a more general cohesive law with additional parameters, such as an exponential-linear cohesive law, can enhance the accuracy of the backward G_{II} estimation method and FEM in correlating with experimental behavior. However, increasing the number of parameters may also introduce challenges, potentially causing the optimization process to diverge or fail.

7.2. Adhesive internal stress analysis (shear and peel)

Numerical simulation was performed for all the specimens. The results, however, were analyzed based on two different approaches. The first approach is to look at the results at 25% of ultimate load for each sample. In this case, obviously, the load changes according to the intrinsic characteristics of each joint. On the other hand, the second approach is to visualize how each sample behaves considering a fixed load for all the specimens.

7.2.1. First approach (25% of relevant peak load)

Figure 7.5a and b show the results of shear and peel stresses. All the curves are extracted at the same timestep (almost 25% of ultimate load) after the simulation started. Looking at the results of the simulation it was understood that for both shear and peel stresses, the effect of the joint width is negligible. For this reason, it is not reported in the graphs for all the specimens. The same result was also obtained experimentally for the computed shear stress reported in Figure 6.3. For this reason, all the results related to one width only, for example, W1, are discussed.

Figure 7.5a and b show that for both peel and shear stresses the maximum values appear at the edges of the joint while the minimums occur in the middle as expected. This result is also in agreement with the work of Reis et al [58]. Figure 7.5a shows that increasing the thickness of the substrate increases the amount of shear stress, regardless of the joint length. However, increasing the joint length results in a reduction of the maximum shear stress. These findings are also consistent with the experimental results expressed in section 6.1. On the other hand, Figure 7.5b shows that increasing both the thickness of the substrates and the joint length led to an increase in peel stress. However, that does not mean the overall strength of the joint will become lower under shear tensile loading. This is because an SLJ behavior is mainly ruled by shear mode. When the joint length and substrate

thickness increase, the parameters related to this mode improve the stiffness and load capacity of the joint with a much larger scale in comparison with the weakness introduced to the joint by peel mode.

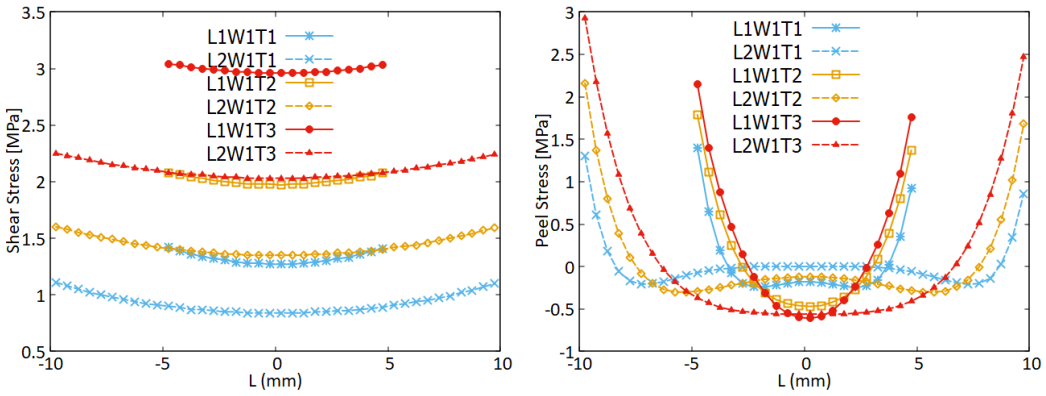

a b

Figure 7.5. Shear and Peel Stresses along the joint (line AB) at 25% of ultimate load for each specimen; a) Shear stress L1,2W1T1,2,3 b) Peel stress L1,2W1T1,2,3

Another point to be noticed is that the peel stress at the edges has a positive value while it is negative or tends to be zero in the middle of the joint. This effect is more obvious in joints with a longer length. For example, in Figure 7.5b, specimen L2W2T3 demonstrates a hyperbolic-harmonic behavior with tension at the edges and compression in the middle. However, with the decrease of the substrate thickness, L2W1T2 for instance, the maximum compression occurs approximately symmetrically at points between the two edges and the middle of the joint. This is while the amount of compression in the middle of the joint shows a tendency to decrease and reach an almost peel stress-free state in L2W1T1. One reason for this phenomenon is the flexibility of the substrate. As the thickness decreases the curvatures and rotations in the substrates caused by the bending moment have the possibility to occur closer to the edges.

7.2.2. Second approach (Fixed common load)

Figure 7.6a,b,c,d show how shear and peel stresses are distributed over the overlap length under the application of a fixed load. Looking at Figure 7.6a, it can be seen that in specimens with substrate thickness T1, by increasing the overlap length and joint width shear stress decreases. This is why the force is the same, but the bonding area is increasing which means that the force to area ratio reduces. The same trend is observed in cases of specimens with substrate thickness T2 and T3. For this reason, only the results of SLJ with substrate T1 is shown in Figure 7.6a and b. Figure 7.6a shows that as the joint width increases, the stress is distributed

more evenly and the difference between stress values at the edges and in the middle of the joint decreases. The same happens also by increasing the overlap length and the shear distribution curve becomes less curvy and flatter. Similarly, the peel stress is affected by joint width and overlap length (Figure 7.6). Furthermore, Figure 7.6c and d show a comparison of samples with different thicknesses and overlap length considering a fixed joint width (for example W2). Increasing the substrate thickness resulted in a decrease in both shear and peel stresses. Additionally, the specimens with thicker substrates have a less curvy and more flat distribution of stress.

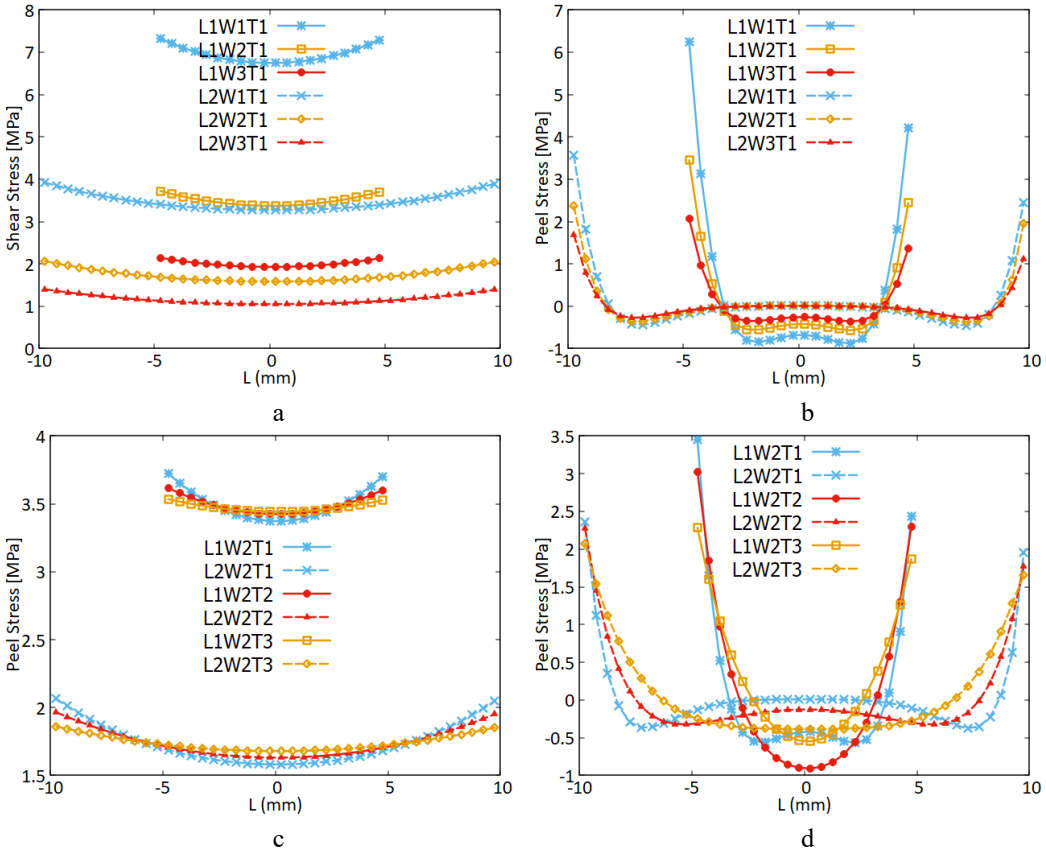

Figure 7.6 Shear and Peel Stresses at a fixed load; a) Shear stress for specimen with substrate thickness of T1 b) Peel stress for specimen with substrate thickness of T1 c) Shear Stress considering a fixed joint width (W2) with different overlap lengths and substrate thicknesses d) Peel stress considering a fixed joint width (W2) with different overlap lengths and substrate thicknesses

7.3. Conclusion of Task 3

The present work aims to study the effect of different joint geometry (adherend thickness, joint width, overlap length) on the response of composite SLJs subjected

to tensile load. Further, an optimization methodology has been introduced to estimate the mechanical properties of a polyurethane adhesive SLJ joint without performing DCB and ENF tests. The conclusions from this research can be drawn as follows:

- An increase of all three geometric parameters (T, W, L) increases both joint stiffness and ultimate load. The joint width and length caused a more significant increase.
- At 25% of ultimate load for each specimen; the width has negligible effects on the distribution of adhesive shear, peel, and substrate normal stresses.

  Keeping the thickness of the substrates constant, an increase in overlap length results in a reduction in shear stress, an increase in peel stress and an increase in normal stress in the substrates.

  For all geometrical configurations, increasing the adherend thickness increases the shear stress and decreases the normal stress.
- At a fixed, common load for all specimens; increasing all three parameters (L, W, T) resulted in a decrease in adhesive max peel, max shear and substrate normal stresses.

  An increase in all three parameters (L,W,T) resulted in a more smooth and less curvy distribution of both peel and shear on overlap length.
- The results revealed that the method used to estimate the mechanical properties of the polyurethane adhesive using FEM, optimization, and SLJ test is an acceptable approach and that the estimated G_{IC} and G_{IIC} are consistent with the value experimentally obtained from fracture testing.
- Comparing the results of this chapter and chapter 5, it can be concluded that for soft adhesive performing ENF test to obtain G_{IIC} might not result in a correct and precise value.

Chapter 8

8. Backface strain analysis of composite SLJs[1] (Task 4)

In this task, an approach is developed to monitor the health of a composite single lap joint (Figure 8.1) both analytically and experimentally. Firstly, using the analytical model the strains that a SLJ substrates undergo are explained when subjected to a tensile load. Afterward, using both analytical model and experimental test the joint monitoring method is described, i.e., it is described when a crack initiates and how it propagates. Finally, the effects of different parameters like adhesive type, joint dimension and load type on the monitoring approach are studied.

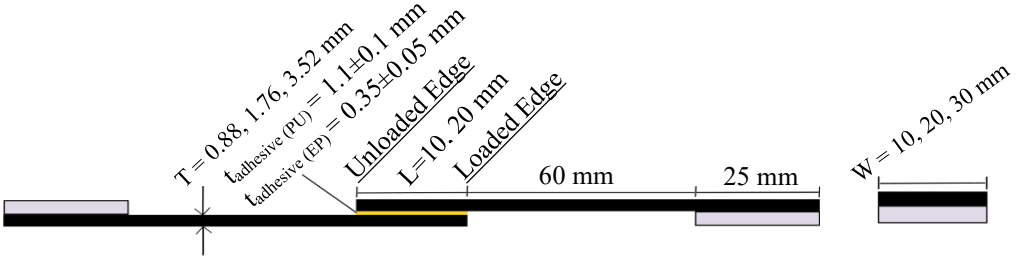

Figure 8.1. SLJ geometry. L: overlap length; W: joint width (figure on the right); T: substrate thickness; and $t_{adhesive}$: adhesive thickness.

[1] **The content of this task is already published as papers** [10–13]**. Minor changes have been made on grammar, formatting, and the synchronization of the list of references in order to integrate the papers within the dissertation.**

8.1. Backface strain prediction using the Bigwood Crocombe Model

In general, a SLJ consists of two substrates, similar or dissimilar, joined using an adhesive. Subjecting SLJs to tensile load usually two tabs (light grey parts in Figure 8.1) are used to avoid geometric asymmetricity. However, in each end of the bond, SLJs experience a mixed-mode loading due to the intrinsic eccentricity related to the overlapping geometry Figure 4.4. The tensile load by itself results in a positive strain in the substrate. The bending moment may cause both positive and negative strain on the backface of the substrates [12,13,98]. Using the Bigwood and Crocombe model, as explained in section 4.2, this positive and negative strain as well as the total strain on the substrate backface of the SLJ have been computed and are shown in Figure 8.2a,b,c,d and Figure 8.3a,b,c,d, respectively, for epoxy and polyurethane SLJs. As the analytical model is independent of the specimen's width only four configurations remain and that is why a generic letter W is used to name the samples in this section. In each figure, the blue curve indicates the strain due to the tensile load which is always positive. The red line, on the other hand, is the strain caused by the bending moment. In most parts of the joint backfaces, especially near to edges, the bending strain has a negative value and is very close to zero in the middle of the joint. Finally, the yellow line is the total strain on the substrate backface of the specimens which includes the effects of both tensile and bending strains.

Figure 8.2a,b,c,d and Figure 8.3a,b,c,d show that the distribution of the tensile strain in SLJs with both adhesive types is positively and continuously increasing from the unloaded to the loaded end of the adherend. This increase is approximately linear in polyurethane SLJs (Figure 8.3a,b,c,d). In epoxy SLJs, when the overlap length is L1 the tensile strain is approximately linear (Figure 8.2a,c) while when the overlap length is L2 a sort of plateau (Figure 8.2b,d) can be seen in the middle of the joint.

Conversely, the distribution of the bending strain changes with the overlap length, the substrate thickness, and the adhesive types. Moreover, the bending strain absolute value near to the bonding area ends is much larger than the tensile strain. This means that the distribution of the total strain is mainly affected by the bending strain and the total strain distribution has approximately similar shape as the bending strain. It should be also noted that in the middle of the joint, the total strain is influenced by both tensile and bending strains.

Considering the effects of adherend thickness and overlap length, the bending strain distribution is more wavy for smaller thickness (compare Figure 8.2a,b with Figure 8.2c,d and Figure 8.3a,b with Figure 8.3c,d) and longer overlap (compare Figure 8.2a,c with Figure 8.2b,d and Figure 8.3a,c with Figure 8.3b,d,). This is because in case of a more compliant adherend and longer overlap the wavy behavior of the bending moment distribution has more possibility to appear [12,13]. Regarding the effects of adhesive type and thickness, the thinner and stiffer epoxy causes a more wavy distribution of the bending strain compared to the thicker and softer polyurethane (compare Figure 8.2a with Figure 8.3a, Figure 8.2b with Figure 8.3b, etc.).

As a result, it can be seen that there is a sort of plateau in the total strain distribution of epoxy SLJs especially in joints with larger overlap lengths (Figure 8.2b,d). Conversely, in the polyurethane SLJs the distribution of the total strain is nearly linear (Figure 8.3a,c) or wavy (Figure 8.3b,d). In general, the zone close to the unloaded end of the adherend (left of the graphs in Figure 8.2 and Figure 8.3) undergoes small strain values (the strain must vanish in this end), whilst in the zone close to the loaded end (right of the graphs) the strain is always negative and exhibits the highest absolute values, due to the prevailing effect of the bending moment.

As a further remark, it can be noted that the strain distributions of Figure 8.2, being the adhesive brittle and nearly elastic linear until failure, is representative also of the distribution that would occur under impending failure. On the contrary, the strain distributions of Figure 8.3, being the adhesive ductile, is not representative of the distribution under impending failure.

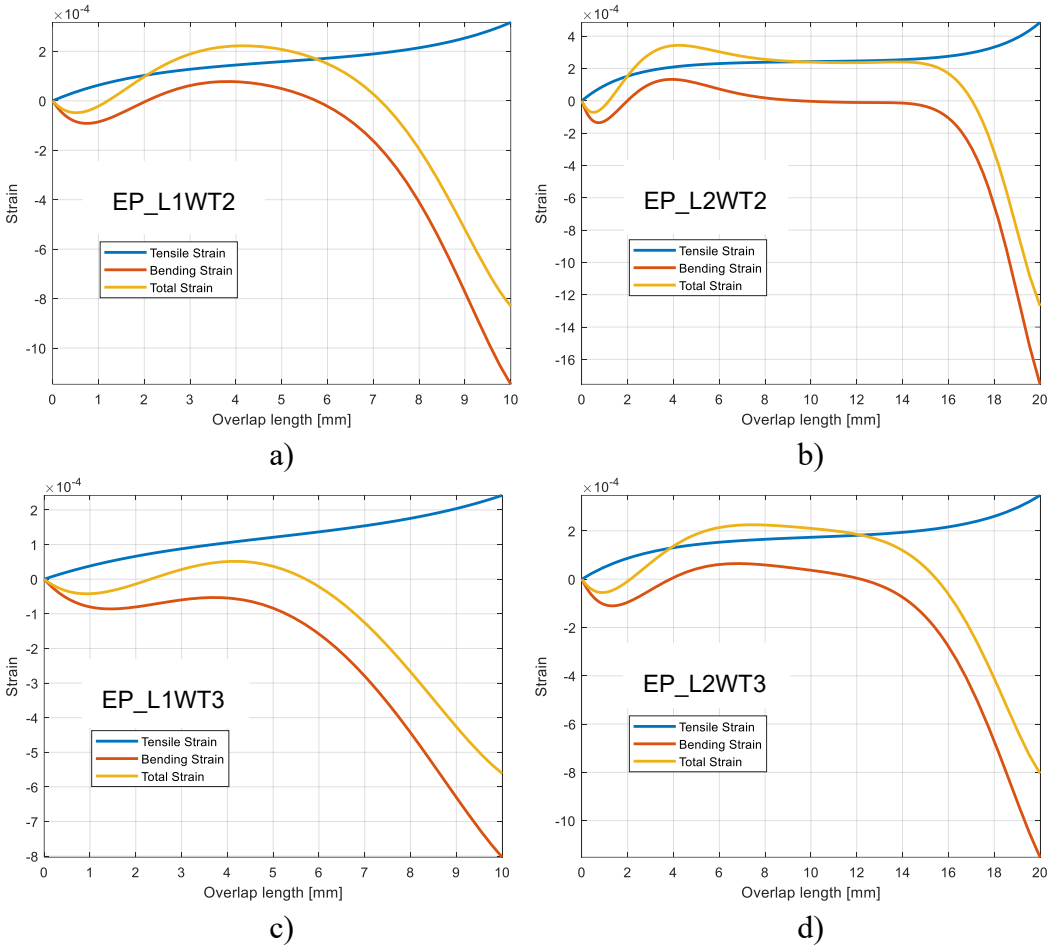

Figure 8.2. Tension and bending strain distribution on the backface of substrates using Bigwood and Crocombe model at 20% of ultimate load for epoxy adhesive SLJs for different configurations: a) EP_L1WT2; b) EP_L2WT2; c) EP_L1WT3; d) EP_L2WT3.

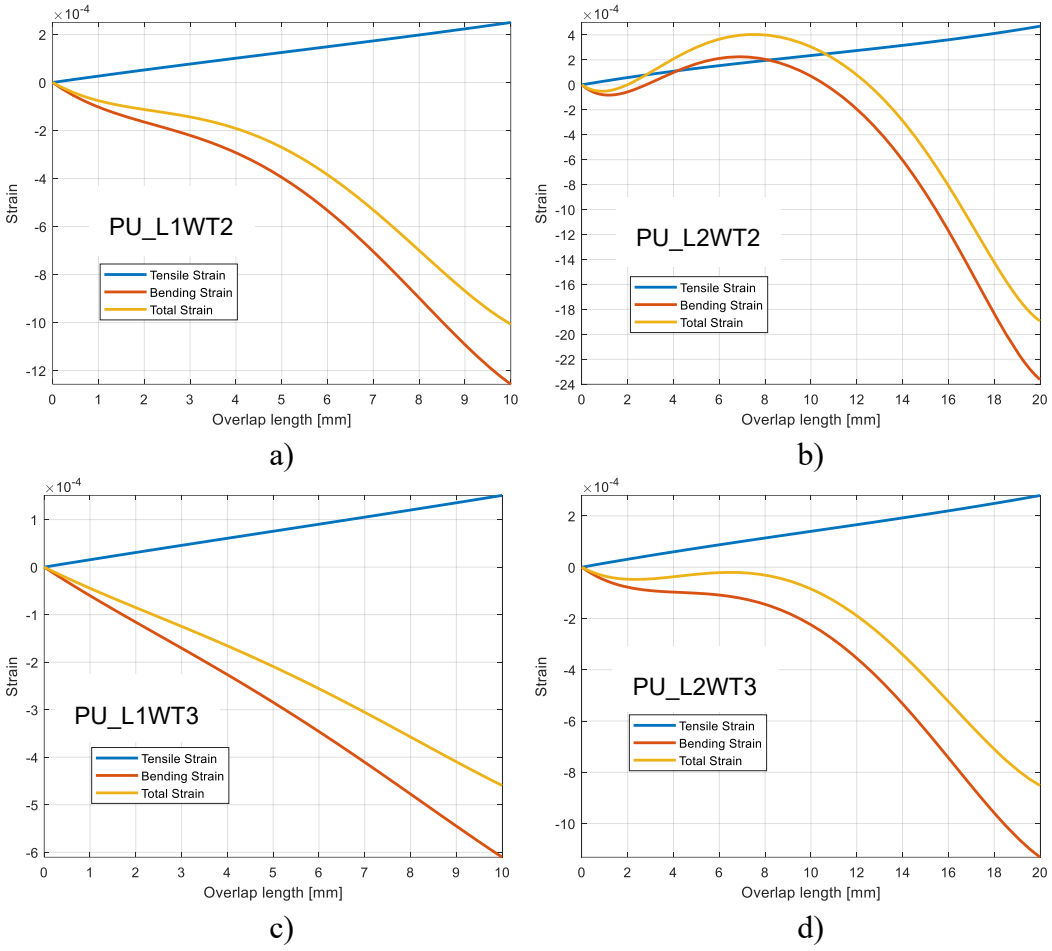

Figure 8.3. Tension and bending strain distribution on the backface of substrates using Bigwood Crocombe model at 20% of ultimate load for polyurethane adhesive SLJs for different configurations: a) PU_L1WT1; b) PU_L2WT1; c) PU_L1WT2; d) PU_L2WT2.

8.2. Definition of Zero-Strain Point (ZSP) using DIC

As explained and confirmed by the modified Bigwood and Crocombe model in section 8.1, SLJs experience a combined strain. The conflicting strains (mainly negative due to the bending moment and positive due to the tensile force) create the ZSP on the substrate's surface, as mentioned in the introduction. The ZSP maintains its strain value of zero until damage begins to propagate in the joint as it is shown in this section. In other words, in the point of initially zero strain (ZSP), when damage in the specimen begins the strain becomes negative.

To show the ZSP behavior, Figure 8.4a shows the strain along the overlap for a specimen (EP_L2W3T3) made with the epoxy adhesive that has an overlap of 20 mm, a width of 30 mm, and a thickness of 3.52 mm. Each curve is the distribution of the strain along the overlap length at a certain time or load. Numerous curves cross a common point where the strain is zero, as shown in Figure 8.4a by the red circle at 14.2 mm. It can be observed that the strain lines along the overlap cross the zero point at 14.2 mm before the damage propagates in the adhesive layer. This effect can be observed in the remaining lines that are not passing through the circle until the adhesive fails. To visualize how the strain in the ZSP point changes as the load increases, the specimen's ZSP strain and load-displacement curve are depicted in a single graph in Figure 8.4b. The strain in the ZSP is approximately zero in the elastic part of the load-displacement curve. Simultaneously, as the damage starts and grows (the nonlinear part of the curve before failure) the ZSP records negative strains up to joint failure. Obviously, the DIC was not able to record the displacement and strains very close to the edges of the joint, especially the unloaded edge of the bonding area. This is because when the specimen moves or rotates, and the damage grows in the joint the light and focus of lenses are no longer precise as before. Subsequently, a rise in the strain history might be observed at the joint edge. Figure 8.4c, on the other hand, shows the comparison between the Bigwood Crocombe analytical model and the experimental result at force 3 kN, with the sample still in the elastic region. It can be seen that the analytical model is in good agreement with the experimental strain obtained from the DIC except for the edges of the joint where the loss of resolution was observed, as reported. The zeroing of the total strain curve given by the analytical model indicates the predicted ZSP (again shown with a circle), which appears at 15.1 mm, and thus in reasonable agreement with the DIC result (14.2 mm).

The same analysis is also done and reported for polyurethane SLJs. Figure 8.5a shows the strain on overlap length for polyurethane SLJ specimen PU_L2W3T3 with an overlap of 20 mm, a width of 30 mm, and a thickness of 3.52 mm. In this sample, the ZSP is located at 10.5 mm. The ZSP exhibits the same behavior (Figure 8.5b) as explained for the epoxy SLJ sample (Figure 8.4). Finally, in Figure 8.5c it can be seen that, although the general trend of the backface strain predicted by the analytical model is in agreement with the experimental measurement, the precision of the analytical model decreases from approximately the middle to the loaded end of the bonding area. This is likely related to the fact that these polyurethane adhesive joints do not precisely exhibit a linear elastic behavior, as assumed by the model. In this case, the ZSP predicted by the analytical model is at 8.5 mm while the experimental results report the ZSP at 10.5 mm.

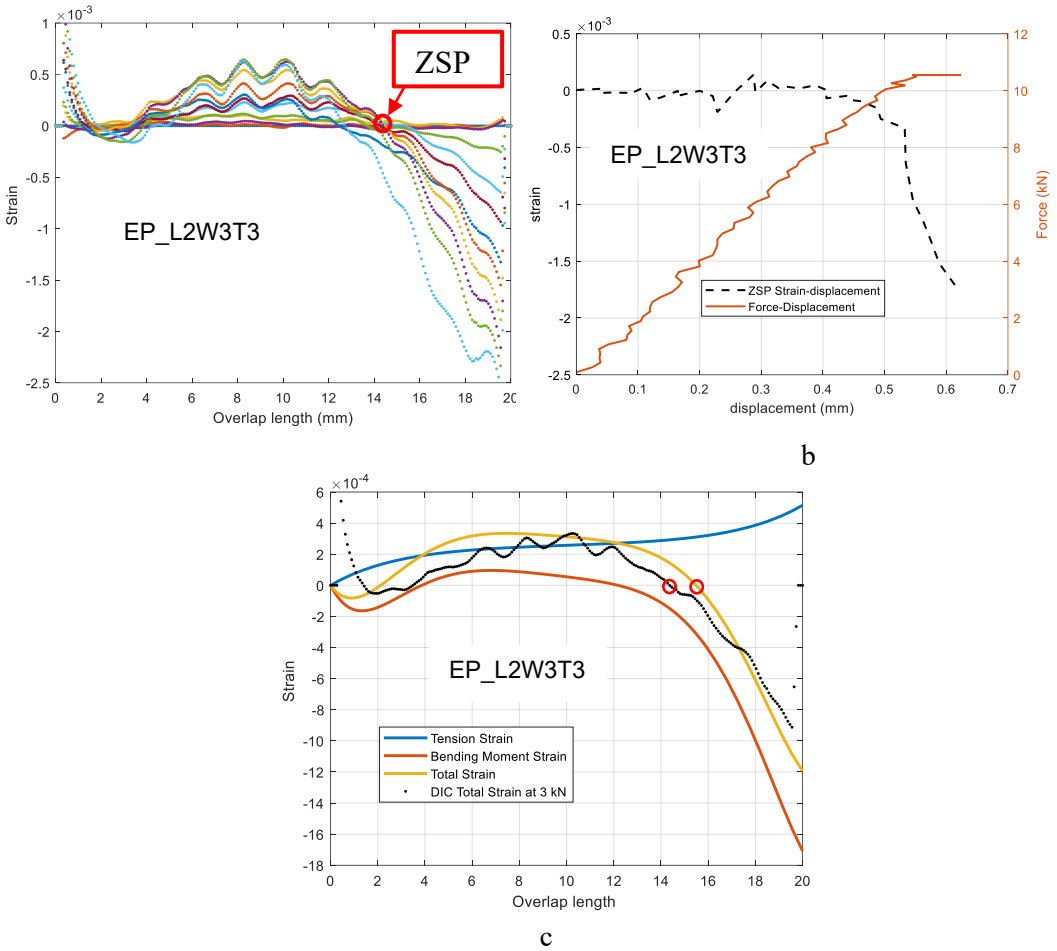

Figure 8.4. ZSP behavior and strain distribution of an epoxy SLJ with L= 20mm, W = 30mm and T= 3.52mm (EP_L2W3T3): a) strain distribution on the overlap length; b) relationship between ZSP strain evolution and force-displacement curve; c) comparison of the DIC experimental total strain with the strains obtained from the Bigwood Crocombe analytical model at 3kN.

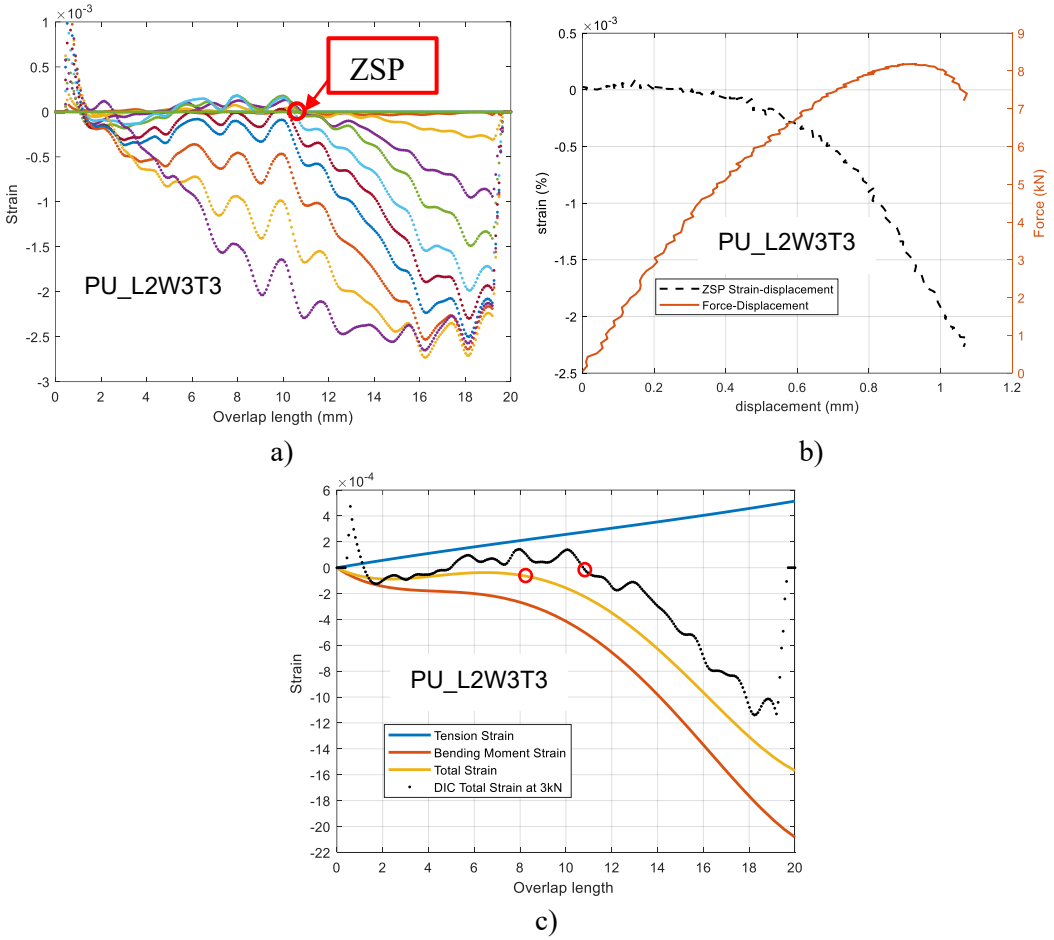

Figure 8.5. ZSP behavior and strain distribution of a polyurethane SLJ with L= 20mm, W = 30mm and T= 3.52mm (PU_L2W3T3): a) strain distribution on the overlap length; b) relationship between ZSP evolution and force-displacement curve; c) comparison of the DIC experimental strain with the strains obtained from the Bigwood Crocombe analytical model at 3kN.

8.3. Validation of the ZSP using Fiber Optic Sensors

In Section 8.2, analyzing the DIC and the Bigwood-Crocombe analytical results from different aspects showed that the so-called ZSP is trustworthy enough to predict the behavior of a joint. However, this methodology using DIC cannot be used as an in-situ methodology. For this reason, optical fibers have been studied to assess whether they can lead to reliable results. Samples L2W2T2 and L2W2T3 were equipped, on both sides of the overlap area, as reported in Section 3.2.3. Figure 8.6a,b show, respectively, the strain signals recorded by four fibers installed on sample L2W2T2 and L2W2T3. Since the results of each fiber were approximately the same (Figure 8.6a,b) as the others just one of them (Figure 8.6c,d) is chosen and explained. For example, for specimen L2W2T2 the third signal and for L2W2T3 the second signal were chosen. Figure 8.6a,b show that the specimen with thicker substrate experienced lower strain and this is due to the lower deformation that the thicker substrate underwent. Due to the relatively high acquisition frequency, in Figure 8.6c,d, one out of each 10 curves was selected for a better visualization and understanding of the data. The ZSP is clearly visible and shown with black circles. This analysis carried out with the optical fibers led to the same outcomes on the ZSP found with DIC analysis (reported in section 8.2). Finally, Figure 8.6e,f shows both the evolution of the strain in ZSP from LUNA and DIC Vs. crosshead displacement matching different stages of the specimen force-displacement curve. As can be seen, very similar results were obtained by comparing the strains measured by optical fibers and DIC methodology. Another point to be noticed is that the rise in the unloaded edge is not visible here in Luna curves. This is a result of the precision of Optic Fiber Sensors that measures the strain correctly also at the joint end proximity.

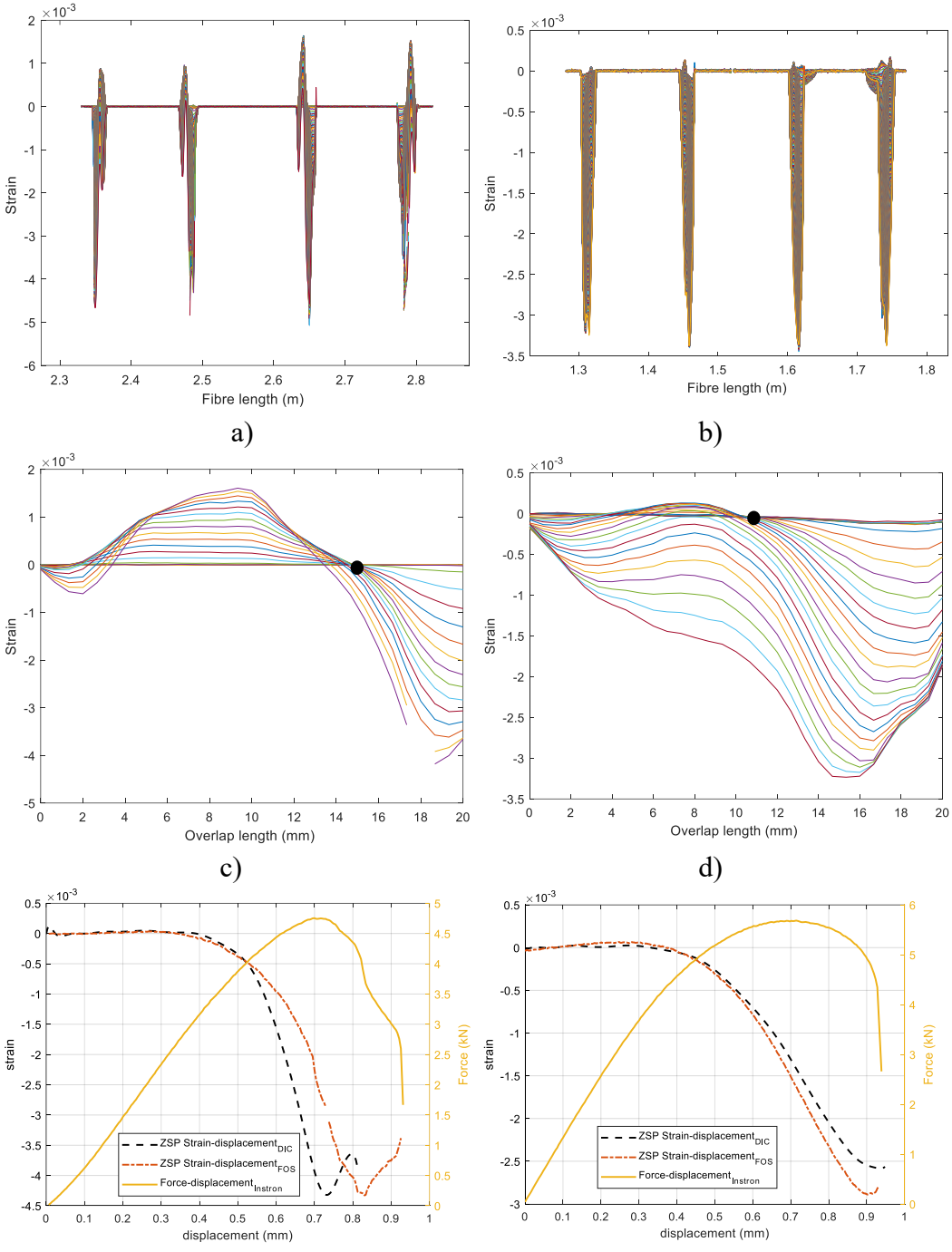

Figure 8.6 ZSP for specimen L2W2T2 and L2W2T3 using both LUNA and DIC a) LUNA signals for L2W2T2 b) LUNA signals for L2W2T3 c) 3rd signal is selected and filtered for L2W2T2 d) 2nd signal is selected and filtered for L2W2T3 e) ZSP strain and force-displacement of L2w2t2 f) ZSP strain and force-displacement of L2w2t3

8.4. Waviness of the strain history curves provided by the DIC

Another point that is worth mentioning is that the strain map for composite substrate looks wavy (for example, Figure 8.4a) due to the intrinsic texture of composite materials. A microscopic image of the composite substrate is shown in Figure 8.7. Each nominated point on the overlap length (Figure 8.7a) is the average of all the points (averaged strain) on the joint width with the same position on the overlap length. For example, the orange point (Figure 8.7a) is the average of the strain on the orange line and the blue point is the average of the points on the blue line. Each line includes both warp and weft but not with the same ratio. This concept is emphasized in Figure 8.7b. As can be seen, the blue line contains more resin, more warp with E_{fl} (longitudinal modulus) and less weft with E_{ft} (transverse modulus) Young modulus. Whilst, the orange line contains less warp with E_{fl} and more weft with E_{ft} Young modulus. Usually, modulus of the fiber in the longitudinal direction is higher compared to its modulus in the transversal direction ($E_{ft} < E_{fl}$) [13]. Therefore, the peaks can be related to the sections (the orange line which contains more of E_{ft}) with a smaller resultant Young modulus because based on the Hooke law those parts undergo larger strain. Based on the same approach, valleys can be due to the sections (the blue line which contains more of E_{fl}) with larger resultant Young modulus.

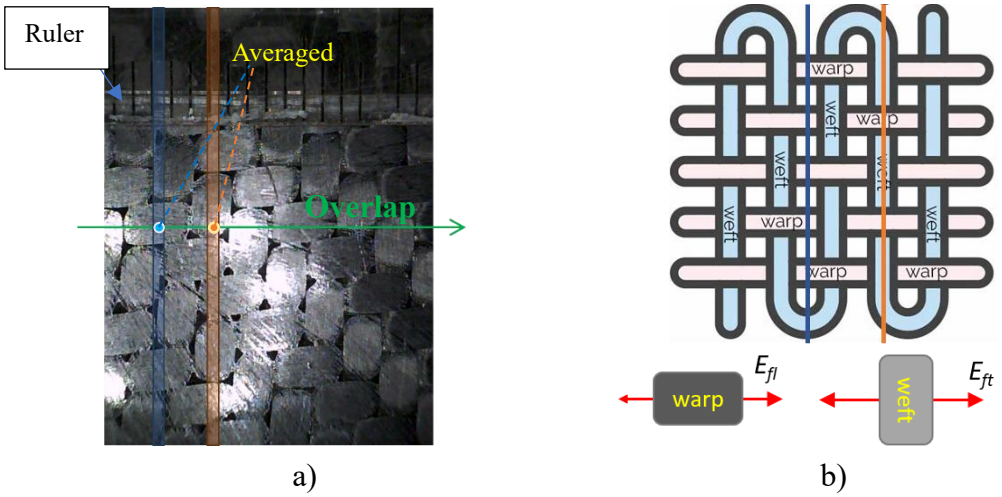

a) b)

Figure 8.7 Composite substrate texture a) microscopic image of the laminate b) Ideal schematic of the laminate texture

On the other hand, the strain history obtained from the optical fibers (Figure 8.6c,d) are smooth in comparison with the ones obtained by DIC. The reason is that the optical fibers measurement does not deal with warp, weft or resin of the material and it is more affected by the general continuous behavior of the measured line.

8.5. ZSP position in joints with epoxy adhesive

Which parameters affect the ZSP position? In this section, the results related to the joints with the epoxy adhesive are discussed. As already explained in 3.2.2, a design of experiment has been conducted which considers the overlap length (L), joint width (W) and substrate thickness (T). After the tests have been done and monitored with the DIC, the results are explained as follows. As explained in chapter 6, the repeated tests showed different results and a completely adhesive failure in case of SLJs with epoxy adhesive and substrate T1. Therefore, only results related to T2 and T3 are reported here.

Figure 8.8a,b,c,d,e,f show the strain distribution on the overlap length for the specimens with substrate thickness T2, three different widths (W1, W2 and W3) and two overlap lengths (L1 and L2). In particular, Figure 8.8a,c,e (left part of Figure 8.8) report the strains along the overlap at fixed L1 and T2 and for W1, W2 and W3 respectively. Figure 8.8b,d,f (right part of Figure 8.8) report the strains along the overlap area for SLJ prepared with L2, T2 and the three different widths W1, W2 and W3. Considering a fixed overlap length and substrate thickness the position of the ZSP remains approximately unchanged by increasing the joint width as shown in the images of Figure 8.8a,b,c,d,e,f. For the specimens of thickness T2, the ZSP is located at 6.3±0.1 mm and 16.5±0.2 mm from the free end of the joints respectively for the overlap lengths L1 and L2. This implies that the effect of the joint width is negligible on the position of the ZSP, and it is due to the lack of influence of the width on the stress and consecutively strain responses of the adhesive joints that do not vary with the increase of the considered widths as discussed in Task 2 (Chapter 6). Considering the joint width and the substrate thickness, it can be concluded that by increasing the overlap length the position of the ZSP moves toward the loaded end of the adherend. This could also be justified by the effects of tensile and bending contributions provided in section 8.1 by using the Bigwood and Crocombe model. In a larger overlap length, moving toward the loaded edge of the adherend, the tensile strain increases while the bending strain is still either in the plateau zone or the drop is not drastic, which helps the ZSP to appear closer to the edge.

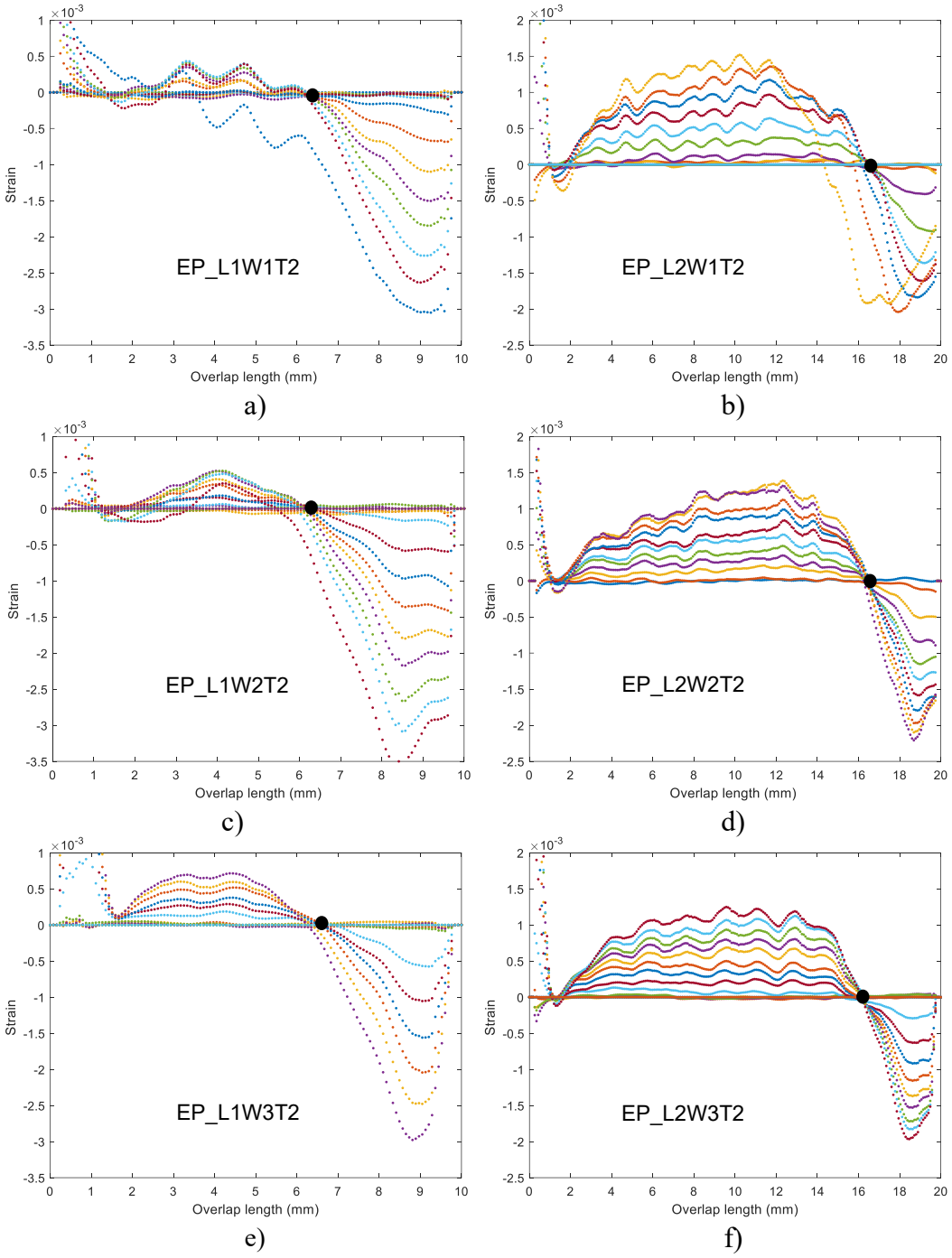

Figure 8.8. Strain history on the overlap length at different times for epoxy adhesive joints with substrate thickness of T2 a) EP_L1W1T2; b) EP_L2W1T2, c) EP_L1W2T2; d) EP_L2W2T2; e) EP_L1W3T2; f) EP_L2W3T2.

Figure 8.9a,b,c,d,e,f show the strain distribution for the epoxy SLJs with the

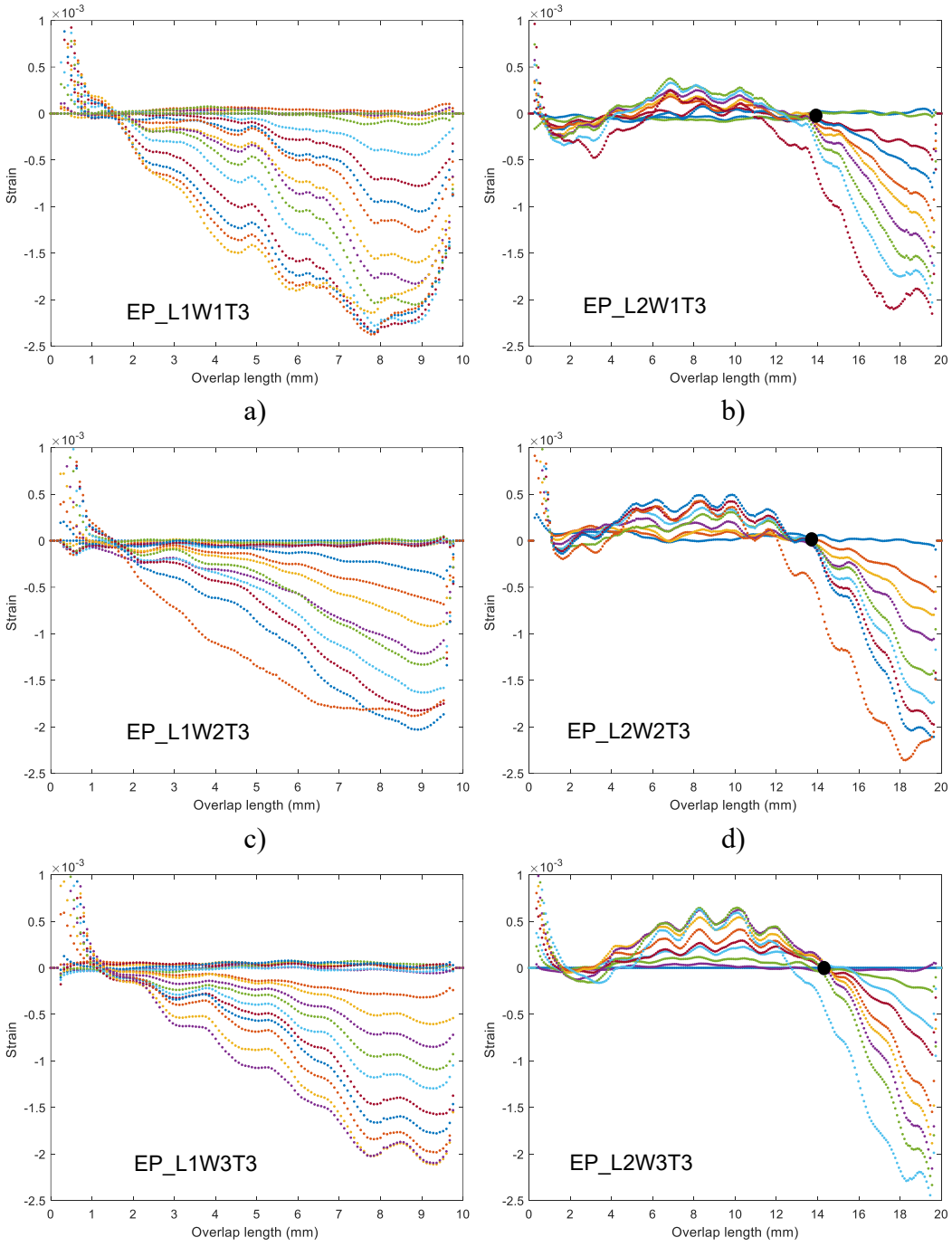

Figure 8.9. Strain history on the overlap length at different times for epoxy adhesive joints with substrate thickness of T3: a) EP_L1W1T3; b) EP_L2W1T3; c) EP_L1W2T3; d) EP_L2W2T3; e) EP_L1W3T3; f) EP_L2W3T3.

substrate thickness T3. Regarding the joint width, the same results explained for T2 are observed. For specimens with T3, the ZSP is located at 4.5±0.5 mm and 13.6±0.5 mm from the left end of the joints respectively for the overlap lengths L1 and L2. The comparison between Figure 8.8a,b,c,d,e,f and Figure 8.9a,b,c,d,e,f show that as the substrate thickness increases the positive strain on the overlap length becomes smaller. This is because when the substrates are thicker, they experience smaller deformation. Additionally, an increase of the substrate thickness causes the ZSP to move toward the middle of the joint or to the half of the joint which is close to unloaded end of the adherend. The reason is, as reported in section 8.1 providing the explanation for Figure 8.2 and Figure 8.3, when the substrate thickness increases, the bending strain positive part tends to disappear, and the plateau part of the distribution is reduced. In this case, the superposition of the positive and negative strain which forms the ZSP moves its position closer to the middle of the joint, as it is visually noticeable.

In table Table 8.1, the effects of different joint dimensions on the location of ZSP in SLJs with epoxy adhesive are summarized. Considering a joint width negligible effect on ZSP, they are shown as W1,2,3.

Table 8.1 Joint dimension effects dimension on ZSP position in SLJs with Epoxy adhesive

Parameters		T1 (0.88mm)	T2 (1.76mm)	T3 (3.52mm)
L1 (10mm)	W1,2,3	Not evaluated	6.3±0.1	4.5±0.5
L2 (20mm)	W1,2,3	Not evaluated	16.5±0.2	13.6±0.5

8.6. ZSP position in joints with polyurethane adhesive

In this section, the strain history on the overlap length for SLJs with a polyurethane adhesive is discussed. Similar to SLJs with epoxy adhesive, the same SLJ geometries are also considered for the polyurethane adhesive to opportunely compare the differences. The reason and explanation for the effect of each joint parameters are already given in section 8.5 and they are also valid in case of polyurethane adhesive. For this reason, the reasonings are not repeated here.

Figure 8.10a,b,c,d,e,f show the strain distribution on the overlap length for all the specimens with substrate thickness T1. In particular, Figure 8.10a,c,e (left part of Figure 8.10) report the strains along the overlap at fixed L1 and T1 and for W1,

W2 and W3 respectively. Figure 8.10b,d,f (right part of Figure 8.10) report the strains along the overlap area for SLJ prepared with L2, T1 and the three different widths W1, W2 and W3. Considering a fixed overlap length and substrate thickness the position of ZSP remains approximately unchanged by increasing the joint width. For specimens with T1, ZSP is located, in average, at 7.3±0.4 mm and 16.7±0.5 mm respectively for overlap length of L1 and L2. The narrowness of the ranges implies that the effect of the joint width is negligible on the position of the ZSP. This is again due to the lack of influence of the joint width on the response of SLJs [10,11]. Considering the joint width and substrate thickness it can be concluded that by increasing the overlap length the position of the ZSP moves toward the bonding area edge which is loaded.

Figure 8.11a,b,c,d,e,f show the results for the polyurethane SLJs with substrates T2 whereas Figure 8.12a,b,c,d,e,f display the same for the thickness T3. Looking at the results of Figure 8.11a,b,c,d,e,f and Figure 8.12a,b,c,d,e,f, it can be seen that, like for the epoxy SLJs, the effect of the joint width is negligible for the tested joint geometries. In the case of the substrate T2 (Figure 8.11), the position of the ZSP is 5.3±0.2 mm and 14.2±0.2 mm, respectively, for joints with overlap lengths of L1 and L2. Conversely, when the substrate thickness is T3 (Figure 8.12) the ZSP is located at 10.0±0.2 mm for the joints with overlap length of L2. However, the individuation of the ZSP for the SLJ prepared with L1 overlap length is more complex. This can be attributed to the lower peak loads measured during the tests due to higher compliance of the adhesive that led to a reduction of the strain in the substrate[10,11,133]. However, the most probable understanding is that the ZSP could be located on the part of the joint between the center of the overlap and the unloaded end of the adherend.

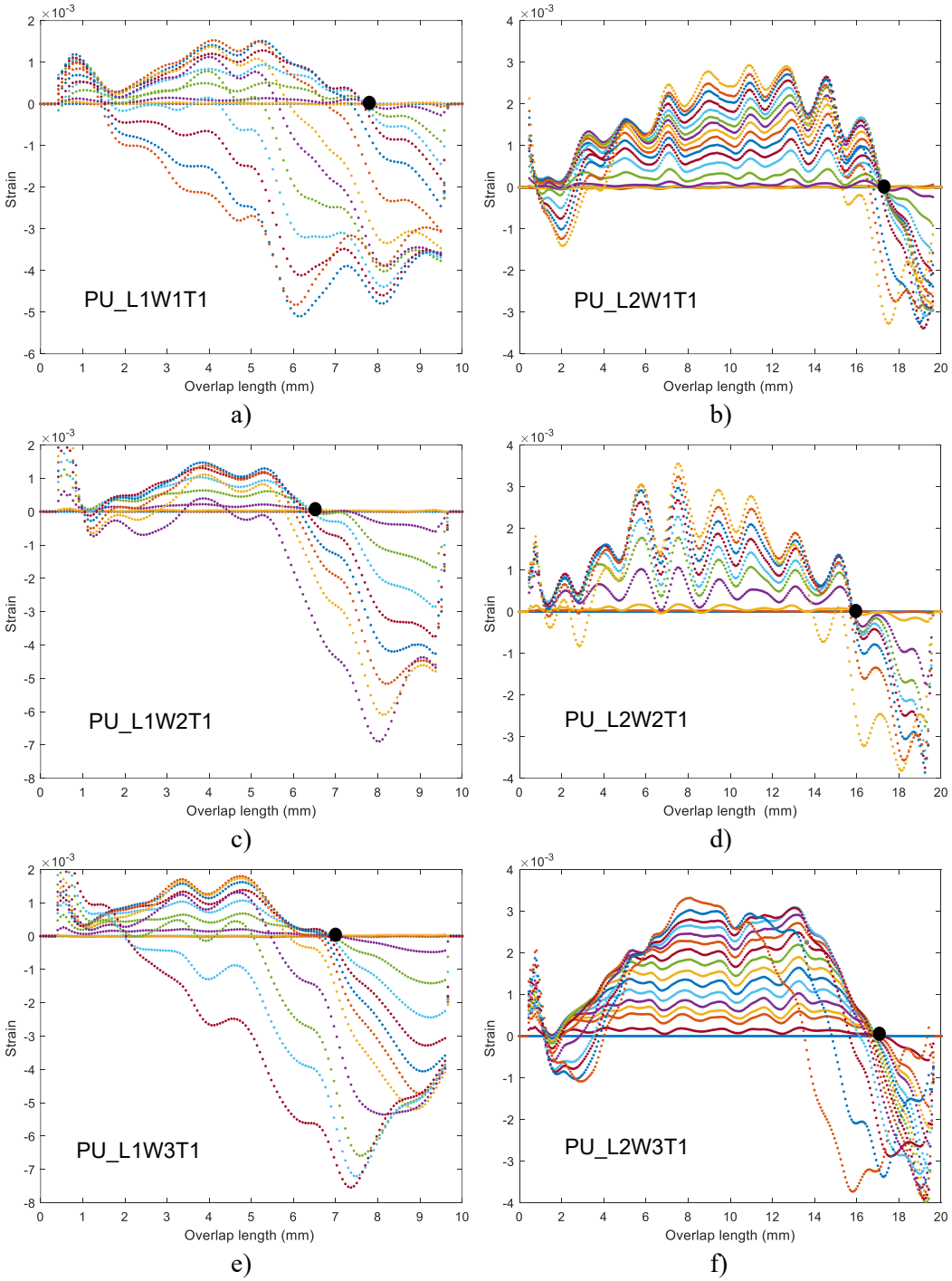

Figure 8.10 Strain history on the overlap length at different times for polyurethane adhesive joints with substrate thickness of T1: a) PU_L1W1T1; b) PU_L2W1T1; c) PU_L1W2T1; d) PU_L2W2T1; e) PU_L1W3T1; f) PU_L2W3T1.

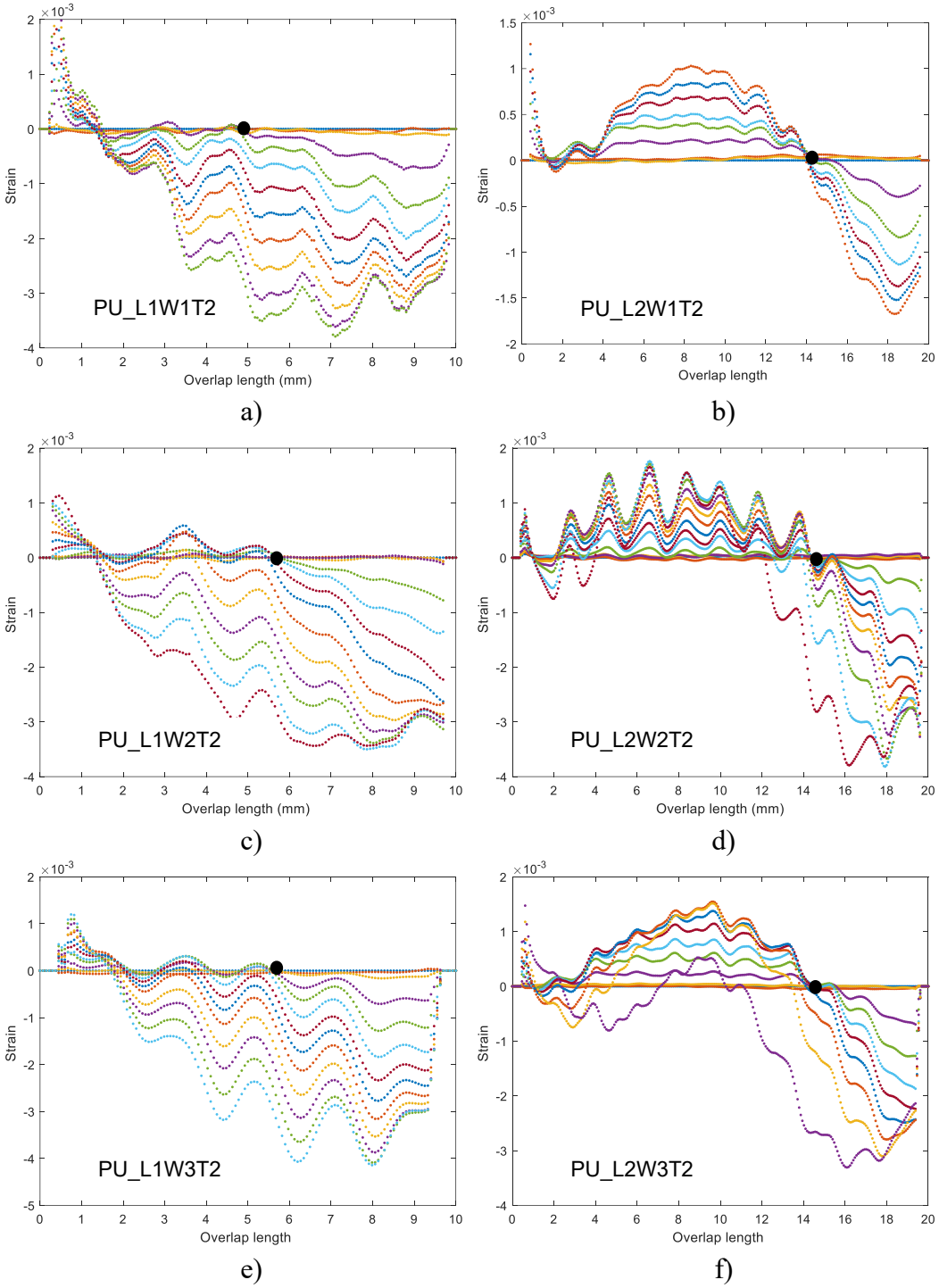

Figure 8.11. Strain history on the overlap length at different times for polyurethane adhesive joints with substrate thickness of T2: a) PU_L1W1T2; b) PU_L2W1T2; c) PU_L1W2T2; d) PU_L2W2T2; e) PU_L1W3T2; f) PU_L2W3T2.

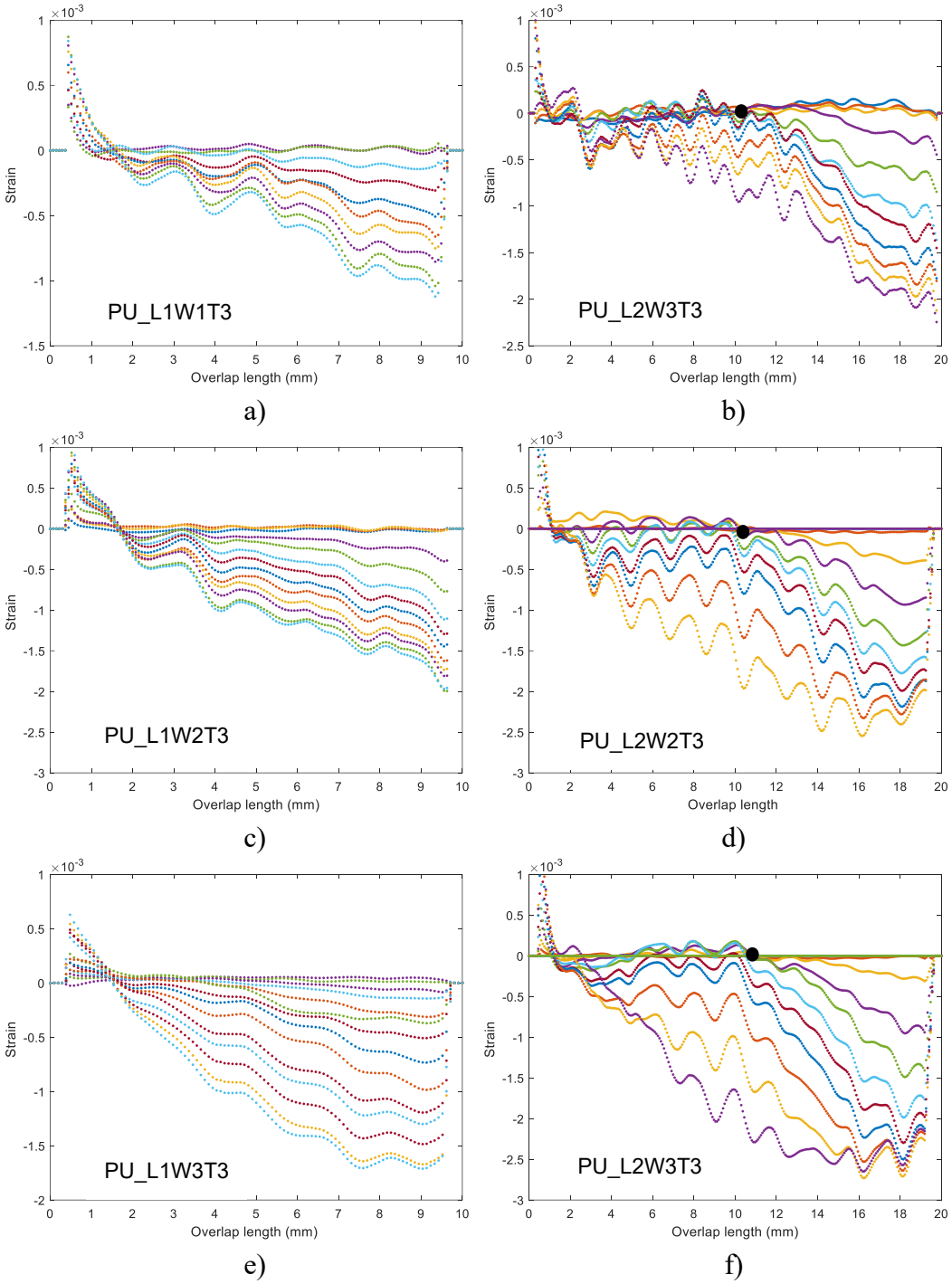

Figure 8.12 Strain history on the overlap length at different times for polyurethane adhesive joints with substrate thickness of T3: a) PU_L1W1T3; b) PU_L2W1T3; c) PU_L1W2T3; d) PU_L2W2T3; e) PU_L1W3T3; f) PU_L2W3T3.

In Table 8.2, the effects of different joint dimensions on the location of ZSP in SLJs with polyurethane adhesive are summarized. Considering a joint width negligible effect on ZSP, they are shown as W1,2,3.

Table 8.2 Joint dimension effects on ZSP position in SLJs with Polyurethane adhesive

Parameters		T1 (0.88mm)	T2 (1.76mm)	T3 (3.52mm)
L1 (10mm)	W1,2,3	7.3±0.4	5.3±0.2	------
L2 (20mm)	W1,2,3	16.7±0.5	14.2±0.2	10±0.2

8.7. General remarks on ZSP

The results shown in Figure 8.8a,b,c,d,e,f, Figure 8.9a,b,c,d,e,f, Figure 8.11a,b,c,d,e,f, and Figure 8.12a,b,c,d,e,f illustrate that the ZSP can be detected for all the considered configurations, both for a structural epoxy adhesive and for a semi structural polyurethane adhesive. Furthermore, the ZSP evolution can be seen as an index of crack initiation. For this reason, the ZSP could be investigated in structural health monitoring applications instead of monitoring the maximum strains. This monitoring, in principle, presents an advantage since is capable of detecting when damage starts and propagates. Conversely, monitoring the maximum strains is strictly dependent on the specific configuration and possible defect of the joints that cannot allow to design a unique strategy to monitor the joints. As mentioned in the introduction, although other researchers proved that the backface strain method [102,134,135] considering the peak strain profile could be effectively used as an index to detect the crack initiation and track its propagation there are also some drawbacks with this method. For example, these works [134,135] used strain gauges as strain measurement tool and the location of the strain gauge and the gauge length showed significant importance, i.e., changing the location and the gauge length will end up with different results. According to [134], if cracks occur simultaneously at both ends of the joint, the observed strain changes will be smaller, and the downturn following the peak, indicative of crack growth, may be negligible. This can complicate the assessment of damage severity and distribution. Another drawback mentioned by [134] is that the sensitivity of the technique decreases as substrate stiffness increases. For more rigid materials, the method may not provide as clear an indication of damage initiation or propagation. Moreover, Bernasconi et al [102] discussed the reliability of minimum peak strain as an index to detect the crack by measuring the backface strain using fiber optic sensors. Although they showed the method is reliable one drawback is that the joint rotation may affect the measurement accuracy and as a result the accuracy of the

method. This factor must be carefully considered when interpreting data, particularly for out-of-plane displacements. On the other hand, in ZSP method the proposed strain measurement tools are DIC or optic fiber sensors. These two tools already eliminate the challenges with the location of the measurement gauge as they can monitor a wider or longer joint area. The DIC in 3D mode also solves the problem of out-of-plane measurements, although it cannot be used in real applications for continuous health monitoring. On the other hand, optic fiber sensors are reliable and can be easily used in real applications, need less wirings than strain gauges since they can be very long and the same wire can be used in different zones and parts of the joint. The ZSP also showed that is not highly dependent on small joint rotations, as many specimens have been tested and the results were repeatable and reliable. So far, the only limitation found by the authors is related to stiff adherends (in this study T3) and short overlap length (L1) which is explained in this section. This limitation is also found in the Crocombe et al. study [134].

In general, with both adhesive types, when the substrate thickness increases, the positive strain in the mid area of the joints becomes smaller due to the higher stiffness of the thicker substrates. This can be observed by comparing Figure 8.8a,b,c,d,e,f to Figure 8.9a,b,c,d,e,f and comparing Figure 8.11a,b,c,d,e,f to Figure 8.12a,b,c,d,e,f. This is also confirmed in section 8.1, considering the changes of the tensile and bending strains when the substrate thickness increases. Essentially, joint configurations that experience larger bending (lower flexural rigidity) show a more pronounced ZSP, due to the larger bending strains. For example, in joints with overlap length L2, comparing Figure 8.8b,d,f to Figure 8.9b,d,f, the positive strain in the middle of the joint drops by 61.5%. This drop in the case of polyurethane SLJs with an overlap length L2 is even larger, 93.7% (comparing Figure 8.11b,d,f to Figure 8.12b,d,f). More importantly, the results illustrate that when the substrate is relatively thick the ZSP can be more easily detected for epoxy adhesive joints rather than polyurethane adhesive joints due to a clearer transition from positive to negative strains. This result could be observed by comparing Figure 8.8a,b,c,d,e,f with Figure 8.11a,b,c,d,e,f, and Figure 8.9a,b,c,d,e,f with Figure 8.12a,b,c,d,e,f for each specific joint dimension. In the tests conducted on adhesive joints prepared with substrate thickness T1 and overlap L2, both adhesive joints show a clear transition from positive to negative strain in the ZSP area, as visible in Figure 8.8b,d,f and Figure 8.11b,d,f. On the other hand, when the joints have an overlap length L1 the transition from positive to negative strain can be more clearly detected in epoxy adhesive SLJs (Figure 8.8a,c,e). Furthermore, the tests conducted on adhesive joints prepared with epoxy adhesive, substrate T2 and overlap L2, also

illustrate that the ZSP can be easily detected (Figure 8.9b,d,f). In contrast, the strain measured for the polyurethane adhesive joints prepared with L2 and T2 show that the ZSP cannot be easily and precisely detected, as shown in Figure 8.12b,d,f. Similarly, the tests conducted on adhesive joints with the short overlap length L1 and thicker substrate T2 (Figure 8.9a,c,e and Figure 8.12a,c,e) exhibit a similar strain curve. This could be considered as a limitation for the ZSP method to predict the joint damage.

Another point to be considered is that, as reported in Task 2 (section 6.3), epoxy adhesive single lap joints do not experience ductile failure and they present a limited plastic zone. Thus, these joints reach the rupture after a short time when the (previous) ZSP starts gaining negative strain. By contrast, considering the polyurethane SLJs, generally the damage propagation time is larger compared to epoxy adhesive SLJs. This can also be seen in the strain distribution at different levels (Figure 8.8a,b,c,d,e,f, Figure 8.9a,b,c,d,e,f, Figure 8.11a,b,c,d,e,f, and Figure 8.12a,b,c,d,e,f) for both types of joints. After the damage started growing and the ZSP started gaining negative strain the number of curves not passing through the ZSP are higher in polyurethane adhesive SLJs before failure. Moreover, the ZSP strain and load-displacement curves reported in Figure 8.13a,b illustrate that the ZSP strain has a sharper drop in the epoxy SLJ. The same comparison can be observed also by comparing Figure 8.4b and Figure 8.5b.

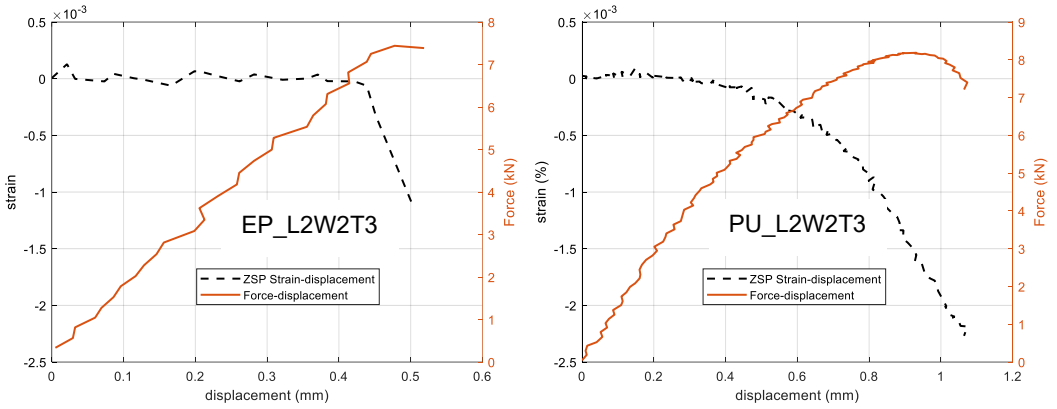

Figure 8.13. Relationship between ZSP strain evolution and force-displacement curve for epoxy and polyurethane SLJs: a) EP_L2W2T3; b) PU_L2W2T3.

8.8. Cyclic loading with polyurethane SLJs

The results presented in Sections 8.2 and 8.3 demonstrated that the ZSP method can be detected with both DIC and optical fibers. Further, these methods can monitor the damage initiation and propagation in SLJs with different bonding area dimensions under normal tensile loading. However, structures and adhesive bonding joints could practically be subjected to cyclic or fatigue loads. In this section, the effect of cyclic loading on damage initiation and propagation of an SLJ using both DIC and optical fiber is studied. The ZSP method is employed as the criteria for the prediction of joint behavior.

Sample L2W1T2 (L=20 mm, W=10 mm, and T=20 mm) was used to study how the strain in the ZSP varies under cyclic loading and whether the strain in ZSP changes from zero when plastic deformation is accumulated in the joint. A six-cycle loading was considered in a way that in each cycle the load increases at a constant velocity of 5 mm/min up to a certain amount, and then unloading starts with the same velocity up to 50 N. After that, the next cycle starts considering the same velocity for loading and unloading. The maximum load for the first, second, third, fourth, fifth and sixth cycles are, respectively, 1 kN, 1.5 kN, 2 kN, 2.2 kN, 2.4 kN, and up to the sample rupture (which for this sample happened at approximately 2 kN). Figure 8.14 shows the load-displacement curves for sample L2W1T2 subjected to the mentioned cyclic loading. As can be seen, after the first and second cycle the joint is still undamaged, and the unloading curve follows the loading curve. The quite small variation in the displacement is due to the initial clearances of the joint. In the third cycle, the peak load falls on a line which passes the first and second cycles' peaks. This could be interpreted as the healthiness of the joint up to the third cycle peak load. However, there is a difference (approximately 28%) between the third unloading curve and the first loading curve, which signals the damage initiation. After the third cycle, the cycles' peaks are not in a line anymore which again indicates that the damage has already been initiated. Moreover, the difference between the fourth unloading curve and the first loading curve becomes even larger (approximately 70%). In the fifth cycle, this difference is 150% and the crack grows noticeably in the joint. Finally, the sixth cycle is when the crack grows up to the joint rupture.

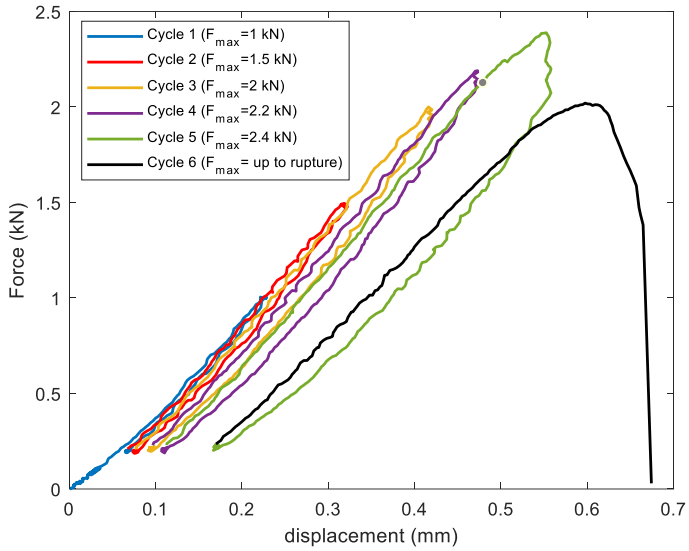

Figure 8.14 Load displacement curve for sample L2W1T2 under cyclic loading

Having the loading cycles explained, Figure 8.15a, b, c, d, e and f illustrate the strain on the backface of L2W1T2 overlap length at each complete cycle. The solid lines are representatives of the data from optical fibers, and the dashed lines represent the data from DIC. As can be seen in Figure 8.15, the maximum recorded strains by the optical fiber are larger than the maximum strain recorded by the DIC. This is because of the texture of the composite materials and the fact explained in detail in section 8.4 about the waviness of DIC strain histories on the overlap length. For the same reason, looking at the strain curves from the DIC data, a sort of plateau is visualized in the mid-area of the joint.

According to the results of Figure 8.14, after the first and second cycle the joint is still in a healthy condition, and this could be verified by results provided in Figure 8.15a,b. Figure 8.15a and b show that the ZSP has still a value of zero strain after the first and second cycle. In the third cycle (Figure 8.15c) the damage initiates as the ZSP starts recording a small negative value. However, before the crack starts propagating the unloading starts. The ZSP is located initially at 15 mm (shown with a black circle) and remains at the same position until the end of the 3rd cycle. In the fourth cycle, ZSP is shown with the purple circle. It can be seen that the ZSP is slightly shifted to the left close to 14 mm, i.e., the crack propagated but to a small extent and again unloading starts. After the crack stopped propagating in the unloading part, a new point (blue circle) appears on the graph (Figure 8.15d) with a negative constant value (close to zero) over time. The position of this point is where the ZSP will appear in the next cycle. This is because the effective overlap

length of the joint decreases after each cycle in such a way that after each cycle it can be assumed that the loading is being applied to a joint with a shorter overlap length. This new point appears in the unloading part of the cycle and exactly when the crack stops propagating. As the unloading part of each cycle is close to the loading part of the next cycle (Figure 8.14), this point represents the ZSP for the next cycle. In the fifth cycle (Figure 8.15e), the blue circle defines the ZSP which is at the same position predicted in the 4th cycle. Here, the crack propagates to a large extent, but the joint has not yet reached the rupture. Therefore, the position of the new ZSP will be estimated in the unloading part as the empty red circle. Finally, in the sixth cycle (Figure 8.15f), the crack propagates completely, and the substrates are detached.

Under cyclic loading there are two ways to analyze the joint. The first one is that at each cycle it can be assumed that the loading is being applied to a new SLJ with its own ZSP. It is enough to monitor the related ZSP strain at each cycle and understand the behavior of the joint as it is done for a normal SLJ subjected to tensile loading. As in real components, it might not be possible to install the DIC because of its dimensions, and as explained before the effective overlap length of the joint changes in each cycle it might not be precise to use strain gauges. Therefore, to use this approach optical fibers are the most useful tool to be employed to monitor continuously the ZSP since the beginning. Figure 8.16a shows the strain history versus time for points on the overlap length (ZSP candidate points) the same as already explained in section 8.2. each line is representative of the strain history at a point. Solid lines show DIC data while dashed lines present optical fibers data. In Figure 8.16a, different cycles can be easily distinguished. In general, when the strain increases in absolute value it means that the sample is in the loading phase of the cycle, otherwise the sample is in unloading phase. Therefore, after each absolute minimum value of strain the next cycle is going to start. As expected, there are not too many points with the approximately constant strain value of zero when the joint is still in healthy condition. Those points are representative for the ZSP which are correspondence to the black circles in Figure 8.15a,b,c. By plotting the strain history of the original ZSP Vs time as well as Force Vs. time in the same graph (Figure 8.16b) the performance of ZSP and behavior of the joint can be explained better. As explained previously in this section based on Figure 8.14 and Figure 8.15, and according to Figure 8.16b, the joint is in a safe condition up to the peak of the third cycle because the ZSP strain remains approximately around zero. In the unloading phase of third cycle, a small drop can be seen in the ZSP strain curve. This might signal the damage initiation, but it is not yet confirmed because ZSP might go back to zero value at the end of unloading phase. Since the curves

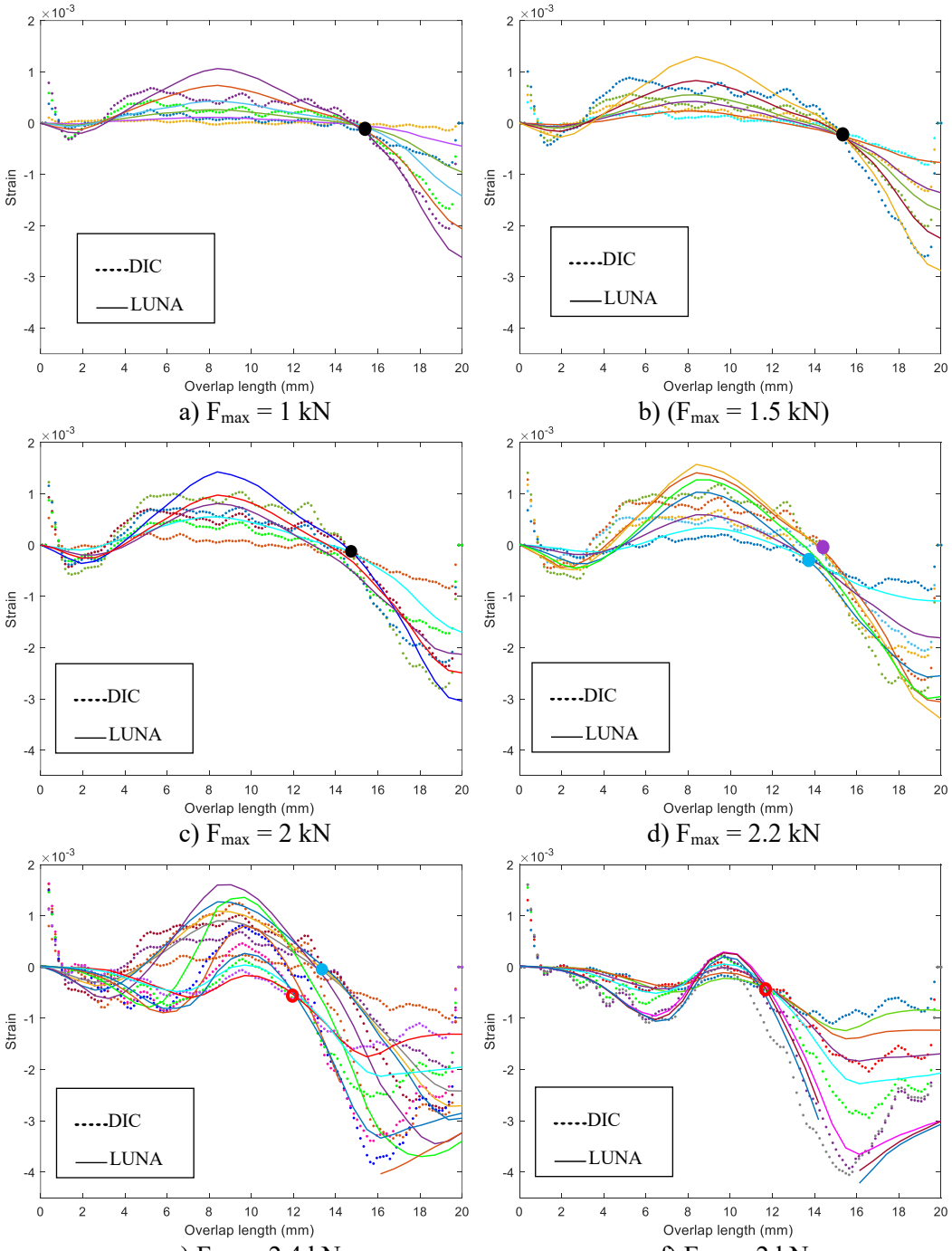

a) F_{max} = 1 kN

b) (F_{max} = 1.5 kN)

c) F_{max} = 2 kN

d) F_{max} = 2.2 kN

e) F_{max} = 2.4 kN

f) F_{max} = 2 kN

Figure 8.15 Backface strain distribution at each cycle for specimen L2W1T2 **a)** cycle 1: healthy condition **b)** cycle 2: healthy condition **c)** cycle 3: damage initiating **d)** cycle 4: small damage propagation **e)** cycle 5: noticeable damage propagation **f)** cycle 6: damage propagation up to rupture

are being filtered there is a possibility to find a point very close to the real ZSP instead of the real ZSP itself. This will result in an oscillation close to zero in the found ZSP value. In the fourth cycle, the ZSP starts gaining value before reaching zero value. This confirms that the damage was initiated in the previous cycle. Up to the fourth cycle the crack starts propagating by the force reaching its maximum value and in the unloading phase. In the fifth cycle the propagation starts shortly before the peak load, and in the loading phase with a drastic drop in the ZSP value at peak load. Finally, in the sixth cycle the crack starts propagating shortly after the loading started and the joint arrives at the rupture at peak force.

Finally, depending on the application and loading type the threshold for ZSP may change and it should be obtained for each case. Before the damage starts the ZSP strain value oscillates near to zero. Considering different specimens, the value of $\pm 1e^{-4}$ is considered as a threshold for the damage initiation. When the joint is healthy the ZSP strain oscillates in this threshold interval. One important point to be taken into account is that when the damage starts, the ZSP strain increases negatively and continuously up to the failure. It might happen that in one oscillation, the ZSP experiences a strain value greater than the threshold (Figure 8.4b) and again the strain value goes back within the safe threshold range. In this case, the oscillation could be a noise and should not be considered as the damage initiation point.

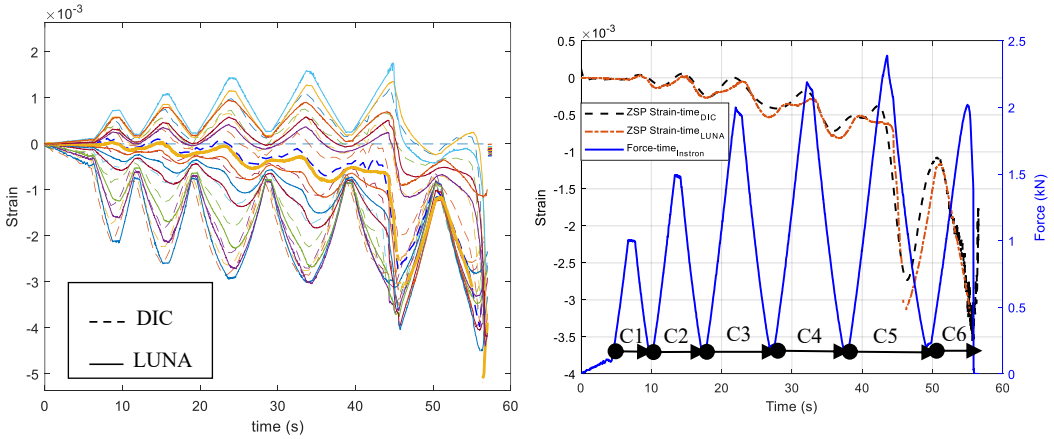

a) Strain history of ZSP candidates on the overlap length

b) ZSP point behavior with respect to the joint behavior

Figure 8.16 ZSP strain using DIC and Luna as well as L2W1T2 force diagram versus the time

When it comes to cyclic loading the same approach can be employed, and even the same threshold can be considered. Figure 8.16 shows that the ZSP strain violates the threshold in the first three cycles, but it returns to the safe threshold interval. However, the ZSP strain does not go back to the threshold interval after the third cycle, which means the crack has been nucleated during the third cycle. A larger interval can also be considered as threshold in case of cyclic loading, for example, $\pm 2.5e^{-4}$ for sample L2W1T2 shown in Figure 8.16.

8.9. Conclusion of Task 4

The present work aims to propose the so-called zero-strain point (ZSP) as a criterion to monitor the healthy condition of composite single lap joints. Furthermore, the effectiveness and reliability of this method were studied when the joint dimension (in particular, adherend thickness, joint width, overlap length), loading type (quasi static and cyclic), and adhesive type change. The method was validated analytically using Bigwood and Crocombe model, and experimentally with the results of the tests performed using DIC (digital image correlation) and LUNA (Optic Fiber Sensors) systems. The drawn conclusions are as follows:

- The ZSP point can be detected for both types of adhesives (epoxy and polyurethane) and the SLJs can be a criterion which provides information to predict the damage initiation and propagation in the joints up to the rupture.
- The joint width shows negligible effect on the position of the ZSP in joints with both adhesive types.
- In joints with larger overlap lengths, the transition from positive to negative strain allows to better identify the ZSP position. Therefore, the ZSP detection is more reliable in joints with larger overlap length.
- For both types of joints, epoxy and polyurethane based, increasing the substrate thickness causes the ZSP to move toward the middle of the joint or the unloaded end of the adherend.
- Considering the same joint dimensions, except for the adhesive thickness, the ZSP of epoxy adhesive SLJs are closer to the middle of the joint or the unloaded end of the adherend compared to polyurethane adhesive SLJs.
- In larger substrate thicknesses, the ZSP is more easily detectable in epoxy adhesive SLJs compared to polyurethane adhesive SLJs due to the presence of larger positive strain on the substrate surface of SLJs.
- When the substrate thickness is relatively large, and the overlap length is relatively short, only negative strains are observed in joints prepared with

both epoxy and polyurethane adhesives. Therefore, the ZSP might not be clearly visible, and this implies a limitation on the application of the ZSP as an indicator of damage initiation.

- Bigwood and Crocombe's analytical model predicts the backface strain distribution with a good approximation before damage initiation for both types of adhesives, more precisely in the case of epoxy adhesive SLJs whose response is closer to the linear elasticity as assumed by the model.
- Considering both cyclic and static tensile loading conditions, the ZSP point can be utilized as a criterion for adhesives SLJs to predict the damage initiation and propagation up to the rupture. This fact was verified precisely with both DIC and optical fiber results.
- According to the optical fiber results, both sides of SLJs (both loaded and fixed adherends) experience approximately the same strain. Therefore, in order to the ZSP method it is enough to observe the strain on backface of one adherend.
- Increasing the substrate thickness causes the ZSP to move toward the middle or free edge of the joint. The same result is obtained by decreasing the overlap length.
- The strain history on the SLJs' overlap length is wavy when analyzing the DIC data due to the texture of composite materials. Whilst it is smooth when the LUNA data is being considered because the strain will be recorded based on the optical fiber deformations.
- Under cyclic loading, although each cycle has its own ZSP which can be used as the criterion to observe the joint condition after the damage initiation, it would be easier and more effective to use the primary ZSP before the damage initiation to monitor the joint behavior.
- Although DIC might not be installed on a component to monitor the healthy condition of the joint, optical fibers could be mounted in order to perform an online and in-situ monitoring of the joints.

Chapter 9

9. Conclusion

In this thesis, the main purpose was to develop a strategy for detecting damage initiation and propagation in composite adhesively bonded single lap joints. To serve this purpose, two different types of adhesives, epoxy and polyurethane-based, were considered. Moreover, as the bonding geometry dimensions play a significant role in joint behavior, SLJs were designed with different overlap lengths, joint widths, and substrate thicknesses. Therefore, based on the predicted challenges in this research activity, a research methodology consisting of four tasks was adopted. The first task is the characterization of adhesive materials by performing tensile, DCB, and ENF tests. The second task is to manufacture SLJs with different adhesives and joint geometry, subject them to tensile load, and analyze the effects of various parameters. The third task is to find an alternative to fracture tests and estimate the fracture properties of polyurethane adhesive, mainly because it is not always possible to perform an ENF test for this type of adhesive as a consequence of its flexibility. Finally, after that the behavior of material and joints is known, the fourth task is developing an approach in order to detect when a cack starts propagating in a SLJ.

The investigation conducted as the first part of this study aimed to characterize and evaluate the mechanical properties of two distinct types of adhesives, namely a rigid epoxy adhesive and a relatively soft polyurethane adhesive. Through a series of rigorous tests, including tensile tests on adhesive bulk dogbone specimens, as well as Double Cantilever Beam (DCB) and End-Notched Flexure (ENF) tests, valuable insights were obtained. The results revealed significant differences in the

mechanical behavior of the two adhesives. Specifically, the epoxy adhesive exhibited higher Young's modulus, ultimate strength, and elongation compared to the polyurethane adhesive. Moreover, the DCB tests demonstrated smoother crack propagation in specimens bonded with polyurethane adhesive, in contrast to the stick-slip mechanism observed in epoxy specimens. Utilizing Corrected Beam Theory (CBT) and Compliance Based Beam Method (CBBM) as data reduction schemes, the critical energy release rates (G_{IC} and G_{IIC}) were determined for both adhesives. The obtained values indicated distinct performance characteristics, with the polyurethane adhesive exhibiting lower G_{IC} but higher G_{IIC} compared to epoxy adhesive. However, it is noteworthy that the G_{IIC} value for polyurethane adhesive was compromised due to substrate interlaminar crack propagation. Overall, these findings provide valuable insights into the mechanical behavior and performance of epoxy and polyurethane adhesives, contributing to a deeper understanding of their suitability and application in various engineering scenarios.

The second part of the thesis involved investigating various joint geometry parameters, such as adherend thicknesses, joint widths, and overlap lengths, and their impact on the mechanical properties of composite Single Lap Joints (SLJs) bonded with epoxy and polyurethane adhesives under tensile loading conditions. This investigation led to several significant findings. Notably, polyurethane SLJs exhibited a distinctive elastic-plastic behavior preceding failure, while epoxy SLJs demonstrated a more linear elastic response until rupture occurred. Comparing the two adhesive types, epoxy joints displayed higher peak load and joint stiffness, averaging 18% and 40% respectively, than their polyurethane counterparts. However, polyurethane SLJs exhibited approximately a 100% greater displacement at maximum load compared to epoxy joints. Furthermore, in polyurethane SLJs, increasing parameters such as thickness, width, and length resulted in enhanced joint stiffness and peak load, with width and length showing more pronounced effects. Conversely, in epoxy SLJs, the influence of length, width, and thickness on peak force and joint stiffness varied, while overlap length had minimal impact. Moreover, changes in joint dimensions affected shear stress differently in epoxy and polyurethane SLJs, with epoxy SLJs being more sensitive to alterations in joint dimensions. These findings underscore the intricate interplay between joint geometry and mechanical behavior, offering valuable insights for optimizing adhesive bonding practices across various engineering applications.

The third research activity of the thesis aims at using the SLJ experimental results and a finite element method to offer an alternative to DCB and ENF tests for polyurethane adhesives. Therefore, an optimization methodology has been

introduced to estimate the fracture mechanical properties of a polyurethane adhesive SLJ joint without performing DCB and ENF tests. The FEM model tries to mimic the SLJ load-displacement curve through optimizing the adhesive properties adopted for computation. Reaching to a good agreement between the FEM output and SLJ experimental result, the fracture properties of adhesive are obtained. Afterward, the adhesive internal stresses were investigated. Key conclusions derived from this research include the validation of SLJ numerical results against experimental findings. Additionally, the methodology used to estimate mechanical properties of polyurethane adhesive via FEM, optimization, and SLJ tests proved effective, yielding G_{IC} and G_{IIC} values consistent with experimentally obtained fracture testing results. Furthermore, adhesive peel and shear stresses demonstrated the importance of bonded joint geometry as crucial parameters on the behavior of SLJs.

Lastly, as the main goal of the thesis, this study introduced the concept of the zero-strain point (ZSP) as a robust indicator for monitoring the structural heath and integrity of composite single lap joints (SLJs). By exploring a range of joint parameters, loading scenarios, and adhesive materials, the ZSP emerges as a reliable predictor of damage onset and progression, crucial for ensuring joint durability. Notably, the ZSP's detectability remains consistent across different adhesive types, such as epoxy and polyurethane, offering valuable insights into damage behavior up to the point of failure. Further analysis reveals that while joint width has minimal impact on ZSP positioning, longer overlap lengths enhance detection accuracy, providing a clearer indication of structural health. Additionally, variations in substrate thickness influence the ZSP's location within the joint, with thicker substrates leading to a shift towards the joint's midpoint or unloaded adherend end, particularly pronounced in epoxy-based joints. The analytical validation using Bigwood and Crocombe's model, along with experimental confirmation through DIC and LUNA devices, underscores the ZSP's efficacy in predicting damage evolution under both cyclic and static loading conditions. Overall, this research highlights the ZSP's potential as a practical tool for real-time health monitoring of SLJs, suggesting optical fibers as a feasible solution for continuous condition assessment in diverse operational environments.

As a future research direction, the BFS technique should be tested on more complex geometries and components, and its effectiveness should also be evaluated under fatigue loading. This method is particularly valuable for applications where structural elements are pushed to their limits, and where component failure could have catastrophic consequences, such as in sailing boats, Formula 1 racing cars,

space launchers, and satellites. Beyond the automotive industry, adhesive joints, especially composite adhesive joints, are increasingly being used in industries, for example aerospace, where components face complex loadings, including fatigue. In these cases, lightweight design is often employed, making the monitoring of composite assemblies essential to determine how far they can be pushed before damage occurs.

References:

[1] da Silva LFM, Öchsner A, Adams RD. Introduction to Adhesive Bonding Technology. Handbook of Adhesion Technology, Berlin, Heidelberg: Springer Berlin Heidelberg; 2011, p. 1–7. https://doi.org/10.1007/978-3-642-01169-6_1.

[2] Petrie EM. Handbook of Adhesives and Sealants. 2nd Edition. New York: McGraw-Hill Education; 2007.

[3] W. Lees. Adhesives in Engineering Design. Springer 1984. https://doi.org/DOI:10.1017/S0001924000014809.

[4] Adamvalli M, Parameswaran V. Dynamic strength of adhesive single lap joints at high temperature. Int J Adhes Adhes 2008;28:321–7. https://doi.org/10.1016/j.ijadhadh.2007.10.005.

[5] Tserpes K, Barroso-Caro A, Carraro PA, Beber VC, Floros I, Gamon W, et al. A review on failure theories and simulation models for adhesive joints. J Adhes 2022;98:1855–915. https://doi.org/10.1080/00218464.2021.1941903.

[6] Weiland J, Sadeghi MZ, Thomalla J V., Schiebahn A, Schroeder KU, Reisgen U. Analysis of back-face strain measurement for adhesively bonded single lap joints using strain gauge, Digital Image Correlation and finite element method. Int J Adhes Adhes 2020;97:102491. https://doi.org/10.1016/J.IJADHADH.2019.102491.

[7] Crocombe AD, Ong CY, Chan CM, Abdel Wahab MM, Ashcroft IA. Investigating fatigue damage evolution in adhesively bonded structures using backface strain measurement. Journal of Adhesion 2002;78:745 – 776. https://doi.org/10.1080/00218460213835.

[8] Zhang Z, Shang JK, Lawrence F V. A Backface Strain Technique for Detecting Fatigue Crack Initiation in Adhesive Joints. J Adhes 1995;49:23–36. https://doi.org/10.1080/00218469508009975.

[9] Ciampaglia A, Fiumarella D, Boursier Niutta C, Ciardiello R, Belingardi G. Impact response of an origami-shaped composite crash box: Experimental analysis and numerical optimization. Compos Struct 2021;256:113093. https://doi.org/10.1016/J.COMPSTRUCT.2020.113093.

[10] Abbasi M, Ciardiello R, Goglio L. Effect of bonding area geometry on the behavior of composite single lap joints (SLJ) and estimation of adhesive properties using finite element method. Journal of Adhesion 2023. https://doi.org/10.1080/00218464.2023.2252338.

[11] Abbasi M, Ciardiello R, Goglio L. Experimental Study on the Effect of Bonding Area Dimensions on the Mechanical Behavior of Composite Single-Lap Joint with Epoxy and Polyurethane Adhesives. Applied Sciences 2023;13:7683. https://doi.org/10.3390/app13137683.

[12] Abbasi M, Ciardiello R, Goglio L. Backface strain as an index to detect damage initiation in composite single-lap bonded joints: Effects of adhesive type and joint dimensions. Int J Adhes Adhes 2024;134:103791. https://doi.org/10.1016/j.ijadhadh.2024.103791.

[13] Abbasi M, Ciardiello R, Goglio L. A novel approach for damage assessment in adhesively bonded composite joints using backface strain technique. Compos B Eng 2024;286:111766. https://doi.org/10.1016/j.compositesb.2024.111766.

[14] Ebnesajjad S, Landrock AH. Adhesives Technology Handbook. Elsevier; 2015. https://doi.org/10.1016/C2013-0-18392-4.

[15] Ramalho LDC, Campilho RDSG, Belinha J, da Silva LFM. Static strength prediction of adhesive joints: A review. Int J Adhes Adhes 2020;96:102451. https://doi.org/10.1016/J.IJADHADH.2019.102451.

[16] Giannis S, Adams RD. Failure of elastomeric sealants under tension and shear: Experiments and analysis. Int J Adhes Adhes 2019;91:77–91. https://doi.org/10.1016/j.ijadhadh.2019.03.007.

[17] Voloshin A, Arcan M. Pure shear moduli of unidirectional fiber-reinforced materials (FRM). Fiber Science and Technology 1980;13:125–34. https://doi.org/10.1016/0015-0568(80)90041-X.

[18] Spaggiari A, Castagnetti D, Dragoni E. Experimental Tests on Tubular Bonded Butt Specimens: Effect of Relief Grooves on Tensile Strength of the Adhesive. J Adhes 2012;88:499–512. https://doi.org/10.1080/00218464.2012.660831.

[19] Ji G, Ouyang Z, Li G. Effects of bondline thickness on Mode-I nonlinear interfacial fracture of laminated composites: An experimental study. Compos B Eng 2013;47:1–7. https://doi.org/10.1016/j.compositesb.2012.10.048.

[20] Marzi S, Biel A, Stigh U. On experimental methods to investigate the effect of layer thickness on the fracture behavior of adhesively bonded joints. Int J Adhes Adhes 2011;31:840–50. https://doi.org/10.1016/j.ijadhadh.2011.08.004.

[21] Teixeira J, Campilho R, da Silva F. Numerical assessment of the Double-Cantilever Beam and Tapered Double-Cantilever Beam tests for the G_{IC} determination of adhesive layers. J Adhes 2018;94:951–73. https://doi.org/10.1080/00218464.2017.1383905.

[22] Ji G, Ouyang Z, Li G. Local Interface Shear Fracture of Bonded Steel Joints with Various Bondline Thicknesses. Exp Mech 2012;52:481–91. https://doi.org/10.1007/s11340-011-9507-y.

[23] Wang W-X, Nakata M, Takao Y, Matsubara T. Experimental investigation on test methods for mode II interlaminar fracture testing of carbon fiber reinforced composites. Compos Part A Appl Sci Manuf 2009;40:1447–55. https://doi.org/10.1016/j.compositesa.2009.04.029.

[24] de Oliveira BMA, Campilho RDSG, Silva FJG, Rocha RJB. Comparison between the ENF and 4ENF fracture characterization tests to evaluate G_{IIC} of bonded aluminium joints. J Adhes 2018;94:910–31. https://doi.org/10.1080/00218464.2017.1387056.

[25] Costa M, Carbas R, Marques E, Viana G, da Silva LFM. An apparatus for mixed-mode fracture characterization of adhesive joints. THEOR APPL FRACT MEC 2017;91:94–102. https://doi.org/10.1016/j.tafmec.2017.04.014.

[26] Hasegawa K, Crocombe AD, Coppuck F, Jewel D, Maher S. Characterising bonded joints with a thick and flexible adhesive layer–Part 1: Fracture testing and behavior. Int J Adhes Adhes 2015;63:124–31. https://doi.org/10.1016/j.ijadhadh.2015.09.003.

[27] Goland M, Reissner E. The Stresses in Cemented Joints. J Appl Mech 1944;11:A17–27. https://doi.org/10.1115/1.4009336.

[28] Dragoni E, Goglio L, Kleiner F. Designing bonded joints by means of the JointCalc software. Int J Adhes Adhes 2010;30:267–80. https://doi.org/10.1016/j.ijadhadh.2009.11.002.

[29] Goglio L, Rossetto M, Dragoni E. Design of adhesive joints based on peak elastic stresses. Int J Adhes Adhes 2008;28:427–35. https://doi.org/10.1016/j.ijadhadh.2008.04.001.

[30] da Silva LFM, das Neves PJC, Adams RD, Wang A, Spelt JK. Analytical models of adhesively bonded joints—Part II: Comparative study. Int J Adhes Adhes 2009;29:331–41. https://doi.org/10.1016/j.ijadhadh.2008.06.007.

[31] da Silva LFM, das Neves PJC, Adams RD, Spelt JK. Analytical models of adhesively bonded joints—Part I: Literature survey. Int J Adhes Adhes 2009;29:319–30. https://doi.org/10.1016/j.ijadhadh.2008.06.005.

[32] Zhao B, Lu Z-H, Lu Y-N. Two-dimensional analytical solution of elastic stresses for balanced single-lap joints—Variational method. Int J Adhes Adhes 2014;49:115–26. https://doi.org/10.1016/j.ijadhadh.2013.12.026.

[33] Ozel A, Yazici B, Akpinar S, Aydin MD, Temiz Ş. A study on the strength of adhesively bonded joints with different adherends. Compos B Eng 2014;62:167–74. https://doi.org/10.1016/j.compositesb.2014.03.001.

[34] Gültekin K, Akpinar S, Özel A, Öner GA. Effects of unbalance on the adhesively bonded composites-aluminium joints. J Adhes 2017;93:674–87. https://doi.org/10.1080/00218464.2015.1136998.

[35] Ayatollahi MR, Akhavan-Safar A. Failure load prediction of single lap adhesive joints based on a new linear elastic criterion. THEOR APPL FRACT MEC 2015;80:210–7. https://doi.org/10.1016/j.tafmec.2015.07.013.

[36] da Silva LFM, Campilho RDSG. Advances in Numerical Modeling of Adhesive Joints. Berlin, Heidelberg: Springer Berlin Heidelberg; 2012. https://doi.org/10.1007/978-3-642-23608-2.

[37] Rice JR. A Path Independent Integral and the Approximate Analysis of Strain Concentration by Notches and Cracks. J Appl Mech 1968;35:379–86. https://doi.org/10.1115/1.3601206.

[38] Rybicki EF, Kanninen MF. A finite element calculation of stress intensity factors by a modified crack closure integral. Eng Fract Mech 1977;9:931–8. https://doi.org/10.1016/0013-7944(77)90013-3.

[39] García JA, Chiminelli A, García B, Lizaranzu M, Jiménez MA. Characterization and material model definition of toughened adhesives for finite element analysis. Int J Adhes Adhes 2011;31:182–92. https://doi.org/10.1016/j.ijadhadh.2010.12.006.

[40] Chousal JAG, de Moura MFSF. Mixed-mode I+II continuum damage model applied to fracture characterization of bonded joints. Int J Adhes Adhes 2013;41:92–7. https://doi.org/10.1016/j.ijadhadh.2012.10.014.

[41] Barenblatt GI. The formation of equilibrium cracks during brittle fracture. General ideas and hypotheses. Axially-symmetric cracks. J Appl Math Mech 1959;23:622–36. https://doi.org/10.1016/0021-8928(59)90157-1.

[42] Dugdale DS. Yielding of steel sheets containing slits. J Mech Phys Solids 1960;8:100–4. https://doi.org/10.1016/0022-5096(60)90013-2.

[43] Álvarez D, Blackman BRK, Guild FJ, Kinloch AJ. Mode I fracture in adhesively-bonded joints: A mesh-size independent modelling approach using cohesive elements. Eng Fract Mech 2014;115:73–95. https://doi.org/10.1016/j.engfracmech.2013.10.005.

[44] Li G, Li C. Assessment of debond simulation and cohesive zone length in a bonded composite joint. Compos B Eng 2015;69:359–68. https://doi.org/10.1016/j.compositesb.2014.10.024.

[45] Rocha RJ. B, Campilho RDSG. Evaluation of different modelling conditions in the cohesive zone analysis of single-lap bonded joints. J Adhes 2018;94:562–82. https://doi.org/10.1080/00218464.2017.1307107.

[46] Karac A, Blackman BRK, Cooper V, Kinloch AJ, Rodriguez Sanchez S, Teo WS, et al. Modelling the fracture behavior of adhesively-bonded joints as a function of test rate. Eng Fract Mech 2011;78:973–89. https://doi.org/10.1016/j.engfracmech.2010.11.014.

[47] Anyfantis KN. On the failure analysis of bondlines: Stress or energy based fracture criteria? Eng Fract Mech 2014;126:108–25. https://doi.org/10.1016/j.engfracmech.2014.04.024.

[48] Carvalho UTF, Campilho RDSG. Validation of pure tensile and shear cohesive laws obtained by the direct method with single-lap joints. Int J Adhes Adhes 2017;77:41–50. https://doi.org/10.1016/j.ijadhadh.2017.04.002.

[49] Campilho RDSG, Banea MD, Neto JABP, da Silva LFM. Modelling adhesive joints with cohesive zone models: effect of the cohesive law shape of the adhesive layer. Int J Adhes Adhes 2013;44:48–56. https://doi.org/10.1016/j.ijadhadh.2013.02.006.

[50] Neto JABP, Campilho RDSG, da Silva LFM. Parametric study of adhesive joints with composites. Int J Adhes Adhes 2012;37:96–101. https://doi.org/10.1016/j.ijadhadh.2012.01.019.

[51] Özel A, Aydin M, Temiż Ş. The effects of overlap length and adherend thickness on the strength of adhesively bonded joints subjected to bending moment. J Adhes Sci Technol 2004;18:313–25. https://doi.org/10.1163/156856104773635454.

[52] Aydin MD, Özel A, Temiz Ş. The effect of adherend thickness on the failure of adhesively-bonded single-lap joints. J Adhes Sci Technol 2005;19:705–18. https://doi.org/10.1163/1568561054890499.

[53] Gültekin K, Akpinar S, Özel A. The effect of the adherend width on the strength of adhesively bonded single-lap joint: Experimental and numerical analysis. Compos B Eng 2014;60:736–45. https://doi.org/10.1016/J.COMPOSITESB.2014.01.022.

[54] Kadioglu F. Effects of compressive applied load on the adhesive single lap joint with different parameters. J Adhes 2022;98:390–411. https://doi.org/10.1080/00218464.2020.1834390.

[55] Kanani AY, Hou X, Ye J. A novel dissimilar single-lap joint with interfacial stiffness improvement. Compos Struct 2020;252:112741. https://doi.org/10.1016/J.COMPSTRUCT.2020.112741.

[56] Kanani AY, Hou X, Ye J. The influence of notching and mixed-adhesives at the bonding area on the strength and stress distribution of dissimilar single-lap joints. Compos Struct 2020;241:112136. https://doi.org/10.1016/J.COMPSTRUCT.2020.112136.

[57] Budhe S, Banea MD, de Barros S, da Silva LFM. An updated review of adhesively bonded joints in composite materials. Int J Adhes Adhes 2017;72:30–42. https://doi.org/10.1016/J.IJADHADH.2016.10.010.

[58] Reis PNB, Antunes FJV, Ferreira JAM. Influence of superposition length on mechanical resistance of single-lap adhesive joints. Compos Struct 2005;67:125–33. https://doi.org/10.1016/J.COMPSTRUCT.2004.01.018.

[59] Fernández-Cañadas LM, Ivañez I, Sanchez-Saez S, Barbero EJ. Effect of adhesive thickness and overlap on the behavior of composite single-lap joints. MAMS 2021;28:1111–20. https://doi.org/10.1080/15376494.2019.1639086.

[60] Moya-Sanz EM, Ivañez I, Garcia-Castillo SK. Effect of the geometry in the strength of single-lap adhesive joints of composite laminates under uniaxial tensile load. Int J Adhes Adhes 2017;72:23–9. https://doi.org/10.1016/J.IJADHADH.2016.10.009.

[61] Cui J, Wang S, Wang S, Chen S, Li G. Strength and failure analysis of adhesive single-lap joints under shear loading: Effects of surface morphologies and overlap zone parameters. J Manuf Process 2020;56:238–47. https://doi.org/10.1016/J.JMAPRO.2020.04.042.

[62] Ciardiello R, D'Angelo D, Cagna L, Croce A, Paolino DS. Effects of plasma treatments of polypropylene adhesive joints used in the automotive industry. Proc Inst Mech Eng C J Mech Eng Sci 2022;236:6204–18. https://doi.org/10.1177/09544062211065361.

[63] Kim JG, Choi I, Lee DG, Seo IS. Flame and silane treatments for improving the adhesive bonding characteristics of aramid/epoxy

composites. Compos Struct 2011;93:2696–705. https://doi.org/10.1016/J.COMPSTRUCT.2011.06.002.

[64] Avendaño R, Carbas RJC, Marques EAS, da Silva LFM, Fernandes AA. Effect of temperature and strain rate on single lap joints with dissimilar lightweight adherends bonded with an acrylic adhesive. Compos Struct 2016;152:34–44. https://doi.org/10.1016/J.COMPSTRUCT.2016.05.034.

[65] da Silva LucasFM, Carbas RJC, Critchlow GW, Figueiredo MA V, Brown K. Effect of material, geometry, surface treatment and environment on the shear strength of single lap joints. Int J Adhes Adhes 2009;29:621–32. https://doi.org/https://doi.org/10.1016/j.ijadhadh.2009.02.012.

[66] Xu W, Wei Y. Strength and interface failure mechanism of adhesive joints. Int J Adhes Adhes 2012;34:80–92. https://doi.org/10.1016/j.ijadhadh.2011.12.004.

[67] Kadioglu F, Avil E, Ercan ME, Aydogan T. Effects of different overlap lengths and composite adherend thicknesses on the performance of adhesively-bonded joints under tensile and bending loadings. IOP Conf Ser Mater Sci Eng 2018;369:012034. https://doi.org/10.1088/1757-899X/369/1/012034.

[68] Adams RD, Peppiatt NA. Stress analysis of adhesive-bonded lap joints. J STRAIN ANAL 1974;9:185–96. https://doi.org/10.1243/03093247V093185.

[69] Grant LDR, Adams RD, da Silva LFM. Experimental and numerical analysis of single-lap joints for the automotive industry. Int J Adhes Adhes 2009;29:405–13. https://doi.org/10.1016/J.IJADHADH.2008.09.001.

[70] Reis PNB, Ferreira JAM, Antunes F. Effect of adherend's rigidity on the shear strength of single lap adhesive joints. Int J Adhes Adhes 2011;31:193–201. https://doi.org/10.1016/J.IJADHADH.2010.12.003.

[71] Martínez MA, de Armentia SL, Abenojar J. Influence of sample dimensions on single lap joints: effect of interactions between parameters. J Adhes 2020;97:1358–69. https://doi.org/10.1080/00218464.2020.1771313.

[72] Li W, Palardy G. Damage monitoring methods for fiber-reinforced polymer joints: A review. Compos Struct 2022;299:116043. https://doi.org/10.1016/J.COMPSTRUCT.2022.116043.

[73] Sánchez-Romate XF, Sbarufatti C, Sánchez M, Bernasconi A, Scaccabarozzi D, Libonati F, et al. Fatigue crack growth identification in bonded joints by using carbon nanotube doped adhesive films. Smart Mater Struct 2020;29:035032. https://doi.org/10.1088/1361-665X/ab7109.

[74] Augustin T, Karsten J, Kötter B, Fiedler B. Health monitoring of scarfed CFRP joints under cyclic loading via electrical resistance measurements using carbon nanotube modified adhesive films. Compos Part A Appl Sci Manuf 2018;105:150–5. https://doi.org/10.1016/j.compositesa.2017.11.015.

[75] Bekas DG, Sharif-Khodaei Z, Baltzis D, Aliabadi MHF, Paipetis AS. Quality assessment and damage detection in nanomodified adhesively-bonded composite joints using inkjet-printed interdigital sensors. Compos Struct 2019;211:557–63. https://doi.org/10.1016/J.COMPSTRUCT.2019.01.008.

[76] Kang MH, Choi JH, Kweon JH. Fatigue life evaluation and crack detection of the adhesive joint with carbon nanotubes. Compos Struct 2014;108:417–22. https://doi.org/10.1016/J.COMPSTRUCT.2013.09.046.

[77] Dasilva S, Jimenez-Suarez A, Rodríguez E, Prolongo SG. Quality assessment and structural health monitoring of CNT reinforced CFRP and Ti6Al4V multi-material joints. Mater Des 2021;210:110118. https://doi.org/10.1016/J.MATDES.2021.110118.

[78] Roth W, Giurgiutiu V. Structural health monitoring of an adhesive disbond through electromechanical impedance spectroscopy. Int J Adhes Adhes 2017;73:109–17. https://doi.org/10.1016/J.IJADHADH.2016.11.008.

[79] Dugnani R, Zhuang Y, Kopsaftopoulos F, Chang F-K. Adhesive bond-line degradation detection via a cross-correlation electromechanical impedance–based approach. Struct Health Monit 2016;15:650–67. https://doi.org/10.1177/1475921716655498.

[80] Deligianni A, Hale JM, Kotsikos G. Development of piezoelectric thick-film sensors to be embedded into adhesively bonded joints. PLAST

RUBBER COMPOS 2016;45:173–80. https://doi.org/10.1080/14658011.2016.1165903.

[81] Zhuang Y, Kopsaftopoulos F, Dugnani R, Chang F-K. Integrity monitoring of adhesively bonded joints via an electromechanical impedance-based approach. Struct Health Monit 2018;17:1031–45. https://doi.org/10.1177/1475921717732331.

[82] Bak KM, KalaiChelvan K, Vijayaraghavan G, Sridhar B. Acoustic emission wavelet transform on adhesively bonded single-lap joints of composite laminate during tensile test. J Reinf Plast Compos 2013;32:87–95. https://doi.org/10.1177/0731684412459249.

[83] Saeedifar M, Saleh MN, De Freitas ST, Zarouchas D. Damage characterization of adhesively-bonded Bi-material joints using acoustic emission. Compos B Eng 2019;176:107356. https://doi.org/10.1016/J.COMPOSITESB.2019.107356.

[84] Saeedifar M, Saleh MN, Nijhuis P, de Freitas ST, Zarouchas D. Damage assessment of a titanium skin adhesively bonded to carbon fiber–reinforced plastic omega stringers using acoustic emission. Struct Health Monit 2022;21:407–23. https://doi.org/10.1177/14759217211001752.

[85] Vijaya Kumar RL, Bhat MR, Murthy CRL. Evaluation of kissing bond in composite adhesive lap joints using digital image correlation: Preliminary studies. Int J Adhes Adhes 2013;42:60–8. https://doi.org/10.1016/J.IJADHADH.2013.01.004.

[86] Comer AJ, Katnam KB, Stanley WF, Young TM. Characterising the behavior of composite single lap bonded joints using digital image correlation. Int J Adhes Adhes 2013;40:215–23. https://doi.org/10.1016/J.IJADHADH.2012.08.010.

[87] Li HCH, Herszberg I, Davis CE, Mouritz AP, Galea SC. Health monitoring of marine composite structural joints using fiber optic sensors. Compos Struct 2006;75:321–7. https://doi.org/10.1016/J.COMPSTRUCT.2006.04.054.

[88] Silva-Muñoz RA, Lopez-Anido RA. Structural health monitoring of marine composite structural joints using embedded fiber Bragg grating strain

sensors. Compos Struct 2009;89:224–34. https://doi.org/10.1016/J.COMPSTRUCT.2008.07.027.

[89] Zeng H, Yan R, Xu L, Gui S. Application study on fiber Bragg grating sensors in damage monitoring of sandwich composite joints. J Sandw Struct Mater 2020;22:1542–63. https://doi.org/10.1177/1099636218789621.

[90] Grundmann N, Brüning H, Tserpes K, Strohbach T, Mayer B. Influence of Embedding Fiber Optical Sensors in CFRP Film Adhesive Joints on Bond Strength. Sensors 2020;20:1665. https://doi.org/10.3390/s20061665.

[91] Zetina-Hernández O, Duarte-Aranda S, May-Pat A, Canché-Escamilla G, Uribe-Calderon J, Gonzalez-Chi PI, et al. Coupled electro-mechanical properties of multiwall carbon nanotube/polypropylene composites for strain sensing applications. J Mater Sci 2013;48:7587–93. https://doi.org/10.1007/s10853-013-7575-3.

[92] Doshi SM, Lyness TB, Thostenson ET. Damage monitoring of adhesively bonded composite-metal hybrid joints using carbon nanotube-based sensing layer. Nanocomposites 2020;6:12–21. https://doi.org/10.1080/20550324.2019.1699229.

[93] Zhu J, Qing X, Liu Q, Liu X, Wang Y. Monitoring of Fiber-Reinforced Composite Single-Lap Joint with Electromechanical Impedance of Piezoelectric Transducer. Materials 2019;12:3241. https://doi.org/10.3390/ma12193241.

[94] Dugnani R, Chang F-K. Analytical model of lap-joint adhesive with embedded piezoelectric transducer for weak bond detection. J Intell Mater Syst Struct 2017;28:124–40. https://doi.org/10.1177/1045389X16645864.

[95] da Silva LFM, Moreira PMGP, Loureiro ALD. Determination of the strain distribution in adhesive joints using Fiber Bragg Grating (FBG). J Adhes Sci Technol 2014;28:1480–99. https://doi.org/10.1080/01694243.2012.698120.

[96] Hild F, Roux S. Digital Image Correlation: from Displacement Measurement to Identification of Elastic Properties – a Review. Strain 2006;42:69–80. https://doi.org/10.1111/j.1475-1305.2006.00258.x.

[97] Satoh T, Abe H. Non-Destructive Detection Method of Fatigue Crack in Spot-Welded Joint Specimens. SAE International Congress and Exposition, SAE International; 1986. https://doi.org/https://doi.org/10.4271/860601.

[98] Janetzko-Preisler A, Sadeghi Z, Adomeit A, Schröder K-U. Damage Assessment in Adhesively Bonded Structures by Using SmartSHM. vol. 2. 2015. https://doi.org/10.12783/SHM2015/27.

[99] Solana A. G., Crocombe A. D., Wahab M. M. A., Ashcroft IA. Fatigue initiation in adhesively-bonded single-lap joints. J Adhes Sci Technol 2007;21:1343–57. https://doi.org/10.1163/156856107782313629.

[100] Curley AJ, Hadavinia H, Kinloch AJ, Taylor AC. Predicting the service-life of adhesively-bonded joints. Int J Fract 2000;103:41–69. https://doi.org/10.1023/A:1007669219149.

[101] Shenoy V, Ashcroft IA, Critchlow GW, Crocombe AD. Unified methodology for the prediction of the fatigue behavior of adhesively bonded joints. Int J Fatigue 2010;32:1278–88. https://doi.org/10.1016/J.IJFATIGUE.2010.01.013.

[102] Bernasconi A., Comolli L. Strain Profile Measurement for Structural Health Monitoring of Woven Carbon-fiber Reinforced Polymer Composite Bonded joints by Fiber Optic Sensing Using an Optical Backscatter Reflectometer. J Adhes 2016;92:440–58. https://doi.org/10.1080/00218464.2015.1043005.

[103] Sans D, Stutz S, Renart J, Mayugo JA, Botsis J. Crack tip identification with long FBG sensors in mixed-mode delamination. Compos Struct 2012;94:2879–87. https://doi.org/10.1016/J.COMPSTRUCT.2012.03.032.

[104] Bernasconi A, Carboni M, Comolli L. Monitoring of fatigue crack growth in composite adhesively bonded joints using Fiber Bragg Gratings. Procedia Eng 2011;10:207–12. https://doi.org/10.1016/j.proeng.2011.04.037.

[105] Pereira FAM, de Moura MFSF, Dourado N, Morais JJL, Xavier J, Dias MIR. Direct and inverse methods applied to the determination of mode I cohesive law of bovine cortical bone using the DCB test. Int J Solids Struct 2017;128:210–20. https://doi.org/10.1016/J.IJSOLSTR.2017.08.028.

[106] Gorman JM, Thouless MD. The use of digital-image correlation to investigate the cohesive zone in a double-cantilever beam, with comparisons to numerical and analytical models. J Mech Phys Solids 2019;123:315–31. https://doi.org/10.1016/J.JMPS.2018.08.013.

[107] Standard ISO 527-3:2018. BSI Standards Publication Plastics-Determination of tensile properties. 2018.

[108] Standard B, ISO 25217:2009. Adhesives-Determination of the mode 1 adhesive fracture energy of structural adhesive joints using double cantilever beam and tapered double cantilever beam specimens. 2009.

[109] Standard. ASTM D-3433 Standard Test Method for Fracture Strength in Cleavage of Adhesives in Bonded Metal Joints.

[110] Benelli A, Ciardiello R, Boursier Niutta C, Goglio L. Experimental and numerical characterization of adhesive joints with composite substrates by means of the Arcan test. Int J Adhes Adhes 2023;122:103321. https://doi.org/10.1016/J.IJADHADH.2022.103321.

[111] https://www.thorlabs.com/newgrouppage9.cfm?objectgroup_id=12731.

[112] https://www.optokon.com/optical-cables-and-fibres.

[113] Livermore Software Technology Corporation (LSTC). (2023). LS-DYNA: Explicit finite element analysis software. https://www.lstc.com/products/ls-dyna.

[114] LSTC. LS-DYNA® KEYWORD USER'S MANUAL VOLUME II Material Models. 2019.

[115] Hartlen DC, Montesano J, Cronin DS. Cohesive Zone Modeling of Adhesively Bonded Interfaces: The Effect of Adherend Geometry, Element Selection, and Loading Condition. 6th International LS-DYNA® Users Conference, 2020.

[116] Niutta CB, Belingardi G, Di P, Turin T, Scattina A. Experimental and Numerical Analysis of a Pristine and a Nano-Modified Thermoplastic Adhesive. Proceedings of the ASME 2018 Pressure Vessels and Piping Conference. Volume 2: Computer Technology and Bolted Joints. Prague, Czech Republic, vol. 2, Prague, Czech: 2018.

[117] Ciardiello R, Boursier Niutta C, Di Sciullo F, Goglio L. Single-lap joints of similar and dissimilar adherends bonded with a polyurethane adhesive used in the automotive industry. IOP Conf Ser Mater Sci Eng 2021;1038:012031. https://doi.org/10.1088/1757-899x/1038/1/012031.

[118] Banea MD, da Silva LFM, Campilho RDSG. The Effect of Adhesive Thickness on the Mechanical Behavior of a Structural Polyurethane Adhesive. J Adhes 2015;91:331–46. https://doi.org/10.1080/00218464.2014.903802.

[119] Leal AJS, Campilho RDSG, Silva FJG, Silva DFO, Moreira FJP. Comparison of different test configurations for the shear fracture toughness evaluation of a ductile adhesive. Procedia Manuf 2019;38:940–7. https://doi.org/10.1016/J.PROMFG.2020.01.177.

[120] Raponi E, Fiumarella D, Boria S, Scattina A, Belingardi G. Methodology for parameter identification on a thermoplastic composite crash absorber by the Sequential Response Surface Method and Efficient Global Optimization. Compos Struct 2021;278:114646. https://doi.org/10.1016/J.COMPSTRUCT.2021.114646.

[121] Stander N, Craig KJ. On the robustness of a simple domain reduction scheme for simulation-based optimization. Eng Comput (Swansea) 2002;19:431–50. https://doi.org/10.1108/02644400210430190.

[122] Bigwood DA, Crocombe AD. Elastic analysis and engineering design formulae for bonded joints. Int J Adhes Adhes 1989;9:229–42. https://doi.org/10.1016/0143-7496(89)90066-3.

[123] Melvin F. Kanninen, Carl H. Popelar. Advanced Fracture Mechanics. Oxford: Oxford University Press; 1985.

[124] MOSTOVOY S, CROSLEY PB, RIPLING EJ. Use of crack-line-loaded specimens for measuring plane-strain fracture toughness. J Mater 1967;2:661–81.

[125] KINLOCH AJ. Adhesion and Adhesives: Science and Technology. London: Chapman and Hall; 1987.

[126] Hashemi S, Kinloch AJ, Williams JG. The Analysis of Interlaminar Fracture in Uniaxial Fibre-Polymer Composites. Proc R Soc Lond A Math Phys Sci 1990;427:173–99.

[127] Blackman B, Dear JP, Kinloch AJ, Osiyemi S. The calculation of adhesive fracture energies from double-cantilever beam test specimens. J Mater Sci Lett 1991;10:253–6. https://doi.org/10.1007/BF00735649.

[128] De Moura MFSF, Gonçalves JPM, Chousal JAG, Campilho RDSG. Cohesive and continuum mixed-mode damage models applied to the simulation of the mechanical behavior of bonded joints. Int J Adhes Adhes 2008;28:419–26. https://doi.org/10.1016/J.IJADHADH.2008.04.004.

[129] Wang Y, Williams JG. Corrections for mode II fracture toughness specimens of composites materials. Compos Sci Technol 1992;43:251–6. https://doi.org/10.1016/0266-3538(92)90096-L.

[130] Fernlund G, Spelt JK. Mixed-mode fracture characterization of adhesive joints. Compos Sci Technol 1994;50:441–9. https://doi.org/10.1016/0266-3538(94)90052-3.

[131] de Moura MFSF, Morais JJL, Dourado N. A new data reduction scheme for mode I wood fracture characterization using the double cantilever beam test. Eng Fract Mech 2008;75:3852–65. https://doi.org/10.1016/j.engfracmech.2008.02.006.

[132] de Moura MFSF, Campilho RDSG, Gonçalves JPM. Pure mode II fracture characterization of composite bonded joints. Int J Solids Struct 2009;46:1589–95. https://doi.org/10.1016/j.ijsolstr.2008.12.001.

[133] Neto JABP, Campilho RDSG, da Silva LFM. Parametric study of adhesive joints with composites. Int J Adhes Adhes 2012;37:96–101. https://doi.org/10.1016/j.ijadhadh.2012.01.019.

[134] Crocombe AD, Ong CY, Chan CM, Abdel Wahab MM, Ashcroft IA. Investigating fatigue damage evolution in adhesively bonded structures using backface strain measurement. J Adhes 2002;78:745 – 776. https://doi.org/10.1080/00218460213835.

[135] Zhang Z, Shang JK, Lawrence F V. A Backface Strain Technique for Detecting Fatigue Crack Initiation in Adhesive Joints. J Adhes 1995;49:23–36. https://doi.org/10.1080/00218469508009975.

Appendix

- MATLAB code for analyzing the DIC data

```
  clear all
%%

%This line uses the dir function in MATLAB to list the contents of the
current folder that have
%the file extension .mat (MATLAB data file) and stores the results in a
structure array nn.
imgfiles=dir('*.mat');

%This loop iterates over the files listed in nn and loads the data
matrices from each file using the load function.
%It then calculates the mean along the second dimension of the eyy
matrix (which represents strain values) using the mean function and
stores it in a temporary variable temp.
%The calculated mean values are stored in a matrix M_eyy with each
column representing the mean values from a different file.
%Similarly, it stores the values from the 100th column of the Yp matrix
(which represents Y-position values) in the corresponding columns of a
matrix M_Yp.
for i=1:length(imgfiles)
    load(imgfiles(i).name);
    temp=mean(eyy,2);
    M_eyy(:,i)=temp;
    %     M_Yp(:,i)=mean(Yp(:,7:281),2);
    M_Yp(:,i)=Yp(:,100);
end
%%

%This line calculates the mean along the first dimension of the M_eyy
matrix, which represents the mean strain values from different files at
each time point.
%The calculated mean values are stored in a variable M_eyy_t.
%It then creates a new figure and plots the calculated mean values on
the y-axis against the time points on the x-axis using the plot
function.
%total average over the aoi
M_eyy_t=mean(M_eyy);
figure, plot(M_eyy_t)
%%

figure
%ploting the  strain Vs. overlap length
plot(M_Yp(:,1:5:end),M_eyy(:,1:5:end),'.')
```

```
xlabel('Overlap length ')
ylabel('Strain ')
hold on

%ploting the average of above plots
%averaging each  line of the matrice M_eyy and M_Yp
M_eyy_tot=mean(M_eyy,2);
M_Yp_tot=mean(M_Yp,2);
plot(M_Yp_tot,M_eyy_tot,'k.','linewidth',5)
xlim([-10 10])

%%%%%%%%% setting the overlap length to [0,20]
figure
clmn = linspace(20,0,size (Yp,1))';
plot(clmn(:,1:15:end),M_eyy(:,1:15:end),'.')
xlabel('Overlap length ')
ylabel('Strain ')
ylim([-4e-3  2e-3])

%The resulting plot shows the strain values for each point over time.
figure
plot(M_eyy(1:3:150,1:5:end)','-')
xlabel('Time ')
ylabel('strain ')


%plotting strain and force V.S. Displacement for one point (ZSP) over
the time

figure
sl_di_fo = readtable ('L2W2T2.xlsx');
plot (sl_di_fo.Displacement (20:1:135,:), M_eyy(64,20:1:135).*100,  '-')
ylabel('strain (%)')
Yp(54:57,100)
yyaxis right
grid on
plot (sl_di_fo.Displacement (20:1:135,:), sl_di_fo.Force (20:1:135,:),
'-')
xlabel('disp (mm)')
ylabel('Force (kN)')
```

- MATLAB code for analyzing the FOS data

```
clear all
%% Reading the data
Straintable = readtable ("L2W2T2_1.csv"); %reading the file provided by
LUNA as a table
num = table2array(Straintable(32:end,4:end)); %converting the table to
array to be used in MATLAB

Fiberl= num(1, 1:end); %the first line of the sum is the position on the
optic fiber length
Strain= num(2:end , 1:end); %the rest is the recorded strain at
different time and one position (each %column) or %different position at
the same time on the fiber (each row)

LDtable = readtable ("LD_Instron.csv"); % load displacement curve from
Instron

%% plotting the base figures to see the fiber signals

figure %plotting the strain Vs. overlap length (all)
plot(Fiberl(1, 1:1:end), Strain(1:1:end , 1:1:end))
xlabel('Fiber length ')
ylabel('Strain ')

figure %plotting the strain Vs. overlap length (reduced frame to include
4 fibers)
plot(Fiberl(1, 3420:1:4170), Strain(1:1:224 , 3420:1:4170)./1000000)
xlabel('Fiber length (m) ')
ylabel('Strain ')

figure %plotting the strain Vs. overlap length (reduced frame to include
2 fibers)
plot(Fiberl(1, 3420:1:3700), Strain(1:3:224 , 3420:1:3700)./1000000)
xlabel('Fiber length (m) ')
ylabel('Strain ')

figure %plotting the strain Vs. overlap length (reduced frame to include
second 2 fibers)
plot(Fiberl(1, 3850:1:4170), Strain(1:2:224 , 3850:1:4170)./1000000)
xlabel('Fiber length (m) ')
ylabel('Strain ')

figure %plotting the strain Vs. overlap length (reduced to 1) 1st fiber
(from left to right)
plot(Fiberl(1, 3440:1:3480), Strain(1:1:end , 3440:1:3480))
xlabel('Fiber length ')
ylabel('Strain 1st')

figure %plotting the strain Vs. overlap length (reduced to 1) 2nd (from
left to right)
plot(Fiberl(1, 3620:1:3680), Strain(1:1:end , 3620:1:3680))
```

```
xlabel('Fiber length ')
ylabel('Strain 2nd ')

figure %plotting the strain Vs. overlap length (reduced to 1) 3rd (from
left to right)
plot(Fiberl(1, 3876:1:3924), Strain(1:1:220 , 3876:1:3924))
xlabel('Fiber length (m)')
ylabel('Strain')

figure %plotting the strain Vs. overlap length (reduced to 1) 3rd
reduced (from left to right)
plot(Fiberl(1, 3870:1:3930), Strain(40:10:180 , 3870:1:3930))
xlabel('Fiber length ')
ylabel('Strain 3rd reuced')

figure %ploting the strain Vs. overlap length (reduced to 1) 4th (from
left to right)
plot(Fiberl(1, 4090:1:4140), Strain(1:1:end , 4090:1:4140))
xlabel('Fiber length ')
ylabel('Strain 4th')

%% extending or shrinking the overlap length to the nominal size of
specimen

figure %plotting the strain Vs. overlap length (reduced to 1) 3rd
reduced according to [-10 10] overlap
Ov_l = linspace(-10,10,size (Strain(1:10:180 , 3880:1:3910),2));
%providing an x axis with the size of overlap length
plot(Ov_l(1, 1:1:end), Strain(1:10:180 , 3880:1:3910))
xlabel('Overlap length (mm) ')
ylabel('Strain')

Ov_l = linspace(0,20,size (Strain(1:10:180 , 3880:1:3910),2));
%providing an x axis with the size of overlap length
plot(Ov_l(1, 1:1:end), Strain(1:10:180 , 3880:1:3910)./1000000)
xlabel('Overlap length (mm) ')
ylabel('Strain')

%% finding the ZSP and plotting its starin vs time

figure %plotting the strain for every point on the overlap length at
different times (reduced to 1) 3rd reduced
   %by plotting this it can be understood when the test is started and
then it can be correlated with the load displacement from Instron
    %n=size(Strain(1:1:180 , 3870:1:3930),1); %shorter range
    n=size(Strain,1); %larger range to see the full curve
    t=-0.05;
    test_t = zeros(1, n);
    for i = 1:n
        t= t+ 0.05;
        test_t(i) = t;
    end
```

```
%plot(test_t(1, 1:1:180), Strain(1:1:180 , 3870:1:3930)) %related to
shorter length with more strain columns
plot(test_t(1, 39:1:260), Strain(39:1:260 , 3901:1:3903)) %related to
the larger range and choosing the start of the test, choosing the ZSP
xlabel('time ')
ylabel('Strain 3rd reuced')

%% plotting the load displacement and strain for the ZSP
%%grapgh without DIC data
figure
plot (LDtable.displacement (:,:), Strain(39:1:260 , 3901:1:3903)./10000,
'-')
ylabel('strain (%)')
yyaxis right
grid on
plot (LDtable.displacement (:,:), LDtable.force(: , :)./1000,  '-')
xlabel('disp (mm)')
ylabel('Force (kN)')

%% adding the ZSP strain and disp data from DIC and plotting in the
final diagram
DIC_st_d = readtable ('DIC_st_d.csv');

%as the data acquisition is not the same an interpolation should be done

degree = 18; % Choose the degree of the polynomial (e.g., degree 2 for a
quadratic polynomial)
coefficients = polyfit(DIC_st_d.disp(:,:), DIC_st_d.str(:,:),
degree);%Use polyfit to fit a polynomial curve to the data
% Create a finer grid of x values
x_finer = linspace(min(DIC_st_d.disp(:,:)), max(DIC_st_d.disp(:,:)),
size(Strain(39:1:260 , 3901:1:3903),1)); % Adjust the number of points
as needed size(Strain(178:1:550 , 2116:1:2118),1) this should be the
same as the plot input

b_fitted = polyval(coefficients, x_finer);% Evaluate the polynomial at
the specified x-values

% Now, 'b_fitted' contains the interpolated y-values at the specified x-
values

figure;% Plot the original data and the fitted curve
plot(DIC_st_d.disp(:,:), DIC_st_d.str(:,:), '-', 'MarkerSize', 6); %
Plot original data points
hold on;
plot(x_finer, b_fitted, '-r', 'LineWidth', 2); % Plot fitted curve
xlabel('d');
ylabel('f');
legend('Original Data', 'Fitted Curve');


figure %plotting the load displacement and strain for the ZSP
```

```
plot (x_finer (:,:), b_fitted (: , :)./100, '--k', 'LineWidth',1.5)%DIC
% pay atttention the Strain () input here should be inserted in x_finer
line
hold on
plot (LDtable.displacement (:,:), Strain(39:1:260 , 3902)./1000000, '-
.', 'LineWidth',1.5) % LUNA
ylabel('strain')
yyaxis right
grid on
plot (LDtable.displacement (:,:), LDtable.force(: , :)./1000,  '-
','LineWidth',1.5) %Instron
xlabel('displacement (mm)')
ylabel('Force (kN)')
legend ('ZSP Strain-displacement_D_I_C','ZSP Strain-
displacement_F_O_S','Force-Displacement_I_n_s_t_r_o_n')
```